COMPACT BINARY MILLISECOND PULSARS: X-RAY OBSERVATIONS AND NUMERICAL SIMULATIONS

By

Eda Vurgun

Departament de Física
Universitat Politècnica de Catalunya

Supervisors:
Manuel Linares
Domingo García-Senz

A thesis submitted for the degree of

Doctor of Philosophy

Barcelona, July 2024

This thesis is submitted to the Physics Department, Universitat Politècnica de Catalunya in fulfillment of the requirements for the PhD degree in Computational and Applied Physics.

Eda Vurgun, July 2024

Acknowledgements

"To my father who never saw this adventure."

ENGLISH

Millisecond pulsars (MSPs) represent a fascinating and crucial subset of rotation-powered pulsars (RPPs). Distinguished by their exceptionally rapid rotation periods ($P_s < 30$ milliseconds) and powerful magnetic fields (ranging from 10^8 to 10^9 Gauss), MSPs are cosmic marvels. These rapidly spinning neutron stars are believed to form through a process in which mass transfer from a companion star in a binary system causes the neutron star to accelerate, or "spin up" to millisecond periods. This "recycling" process not only rejuvenates the pulsar but also sheds light on the complex mechanisms of stellar evolution. The discovery and study of MSPs have significantly advanced our understanding of the life cycles of stars, binary interactions, and the extreme physical conditions in these extraordinary celestial objects. This thesis comprises two parts, both focusing on phenomena associated with MSPs. The first part explores a population of neutron stars using X-ray observational data. Globular clusters (GCs) are known to be extremely efficient at forming MSPs and low-mass X-ray binaries (LMXBs), due to their high stellar densities. Since many of those MSPs and LMXBs are closely packed within the GC core, their X-ray counterparts can only be fully resolved using Chandra's subarcsecond angular resolution. In this thesis, a deep study of the GC M28 (NGC 6626) is presented covering the full 330 ks 2002-2015 ACIS dataset from the Chandra X-ray Observatory. We investigate the X-ray luminosity (L_X), spectrum, and orbital modulation of the 7 known compact binary MSPs in the cluster. We discover a double-peaked X-ray orbital flux modulation in M28I (IGR $J18245$–2452) during its pulsar state, centered around pulsar inferior conjunction. We analyze the spectrum of the quiescent neutron star LMXB to constrain its mass and radius. Using both hydrogen and helium neutron star atmosphere models, we infer a neutron star radius of R = 9.2 - 11.5 km and R = 13.0 - 17.5 km, respectively, for a neutron star mass of 1.4 $M_\odot$ (68% confidence range). We also search for long-term variability in the 46 brightest X-ray sources and report the discovery of six new variable low luminosity X-ray sources in M28.

In the second part of the thesis, we study the interaction of the magnetic field of the neutron star with the nearby accretion disk, carrying out detailed magneto-hydrodynamics (MHD) simulations that incorporate realistic disk structures into the numerical simulations. The primary objective of this section is to elucidate the mechanism driving state transitions in transitional MSPs, whose physical origin remains largely unknown. To perform the simulations, we use an axisymmetric

MHD smoothed particle hydrodynamics (SPH) code recently developed. By implementing the SPH method to our code, we discuss four different interaction scenarios taking the distance from the neutron star to the disk inner radius as 0.5, 1, 5, and 25 times the light cylinder radius. We carry out the simulations using a typical surface magnetic field value for MSPs, $B_0 = 9.6 \times 10^7$ G, associated with the well-known MSP $J1023+0038$ and investigating the magnetic field-disk interaction as a function of the distance to the disk inner radius and the inclination of the magnetic axis. The thesis focuses on numerical simulations of disk structures, both with and without magnetic fields. Initial simulations without magnetic fields established a stable disk configuration, which served as a further study baseline. Subsequent simulations introduced a magnetic field with varying inclination angles to observe its impact on disk stability and the short-term evolution of the simulated portion of the disk. Our findings showed that aligned rotators maintained stability for completing multiple orbits, while higher inclination angles led to instability at the disk.

CASTELLANO

Los púlsares de milisegundos (MSPs) representan un subconjunto fascinante y crucial de púlsares impulsados por rotación (RPPs). Se distinguen por sus períodos de rotación excepcionalmente rápidos ($P_s < 30$ milisegundos) y sus potentes campos magnéticos (que van desde 10^8 hasta 10^9 Gauss), los MSP son maravillas cósmicas. Se cree que estas estrellas de neutrones que giran rápidamente se forman a través de un proceso en el que la transferencia de masa desde una estrella compañera en un sistema binario hace que la estrella de neutrones se acelere o "gire" en períodos de milisegundos. Este proceso de "reciclaje" no sólo rejuvenece el púlsar sino que también arroja luz sobre los complejos mecanismos de la evolución estelar. El descubrimiento y estudio de las MSP ha avanzado significativamente nuestra comprensión de los ciclos de vida de las estrellas, las interacciones binarias y las condiciones físicas extremas en estos extraordinarios objetos celestes. Esta tesis consta de dos partes, ambas centradas en fenómenos asociados con las MSP. La primera parte explora una población de estrellas de neutrones utilizando datos de observación de rayos X. Se sabe que los cúmulos globulares (GCs) son extremadamente eficientes en la formación de MSP y binarias de rayos X de baja masa (LMXBs), debido a sus altas densidades estelares. Dado que muchos de esos MSP y LMXB están estrechamente empaquetados dentro del núcleo del GC, sus contrapartidas de rayos X solo pueden resolverse completamente utilizando la resolución angular de subarcosegundo de Chandra. En esta tesis, se presenta un estudio profundo del GC M28 (NGC 6626) que cubre el conjunto completo de datos ACIS de 330 ks 2002-2015 del Observatorio de rayos X Chandra. Investigamos la luminosidad de los rayos X (L_X), el espectro y la modulación orbital de los 7 MSP binarios compactos conocidos en el grupo. Descubrimos una modulación del flujo orbital de rayos X de doble pico en M28I (IGR J18245–2452) durante su estado de púlsar, centrada alrededor de la conjunción inferior del púlsar. Analizamos el espectro de la estrella de neutrones en la LMXB inactiva para limitar su masa y radio. Utilizando modelos de atmósfera de estrellas de neutrones de hidrógeno y helio, encontramos radios de la estrella de neutrrones de R = 9,2 - 11,5 km y R = 13,0 - 17,5 km, respectivamente, para una masa de estrella de neutrones de 1,4 $M_\odot$ (68% rango de confianza). También buscamos variabilidad a largo plazo en las 46 fuentes de rayos X más brillantes e informamos del descubrimiento de seis nuevas fuentes variables de rayos X de baja luminosidad en M28.

En la segunda parte de la tesis, estudiamos la interacción del campo magnético de la estrella de neutrones con el disco de acreción cercano, realizando simula-

ciones detalladas de magnetohidrodinámica (MHD) que incorporan estructuras de disco realistas en las simulaciones numéricas. El objetivo principal de esta sección es dilucidar el mecanismo que impulsa las transiciones de estado en los MSP de transición, cuyo origen físico sigue siendo en gran medida desconocido. Para realizar las simulaciones, utilizamos un código de hidrodinámica de partículas suavizadas (SPH) MHD axisimétrico desarrollado recientemente. Al implementar el método SPH en nuestro código, analizamos cuatro escenarios de interacción diferentes que toman la distancia desde la estrella de neutrones hasta el radio interno del disco como 0,5, 1, 5 y 25 veces el cilindro de luz. Seguimos las simulaciones utilizando un valor de campo magnético de superficie típico para MSP, $B_0 = 9.6 \times 10^7$ G, asociado con el valor conocido para el MSP PSR $J1023 + 0038$ e investigando la interacción campo magnético-disco en función del ángulo de inclinación entre el eje de rotación y magnético de la estrella de neutrones. La tesis se centra en simulaciones numéricas de estructuras de discos, tanto con como sin campos magnéticos. Las simulaciones iniciales sin campos magnéticos establecieron una configuración de disco estable, que sirvió como base para estudios posteriores. Simulaciones posteriores introdujeron un campo magnético con diferentes ángulos de inclinación para observar su impacto en la estabilidad y evolución del disco. Nuestros hallazgos revelan que los rotadores alineados mantuvieron la estabilidad durante múltiples órbitas, mientras que los ángulos de inclinación más altos provocaron inestabilidad en el disc.

CATALAN

Els púlsars de mil·lisegons (MSPs) representen un subconjunt fascinant i crucial de púlsars de rotació (RPPs). Distinguts pels seus períodes de rotació excepcionalment ràpids (P_s < 30 mil·lisegons) i els potents camps magnètics (que van des de 10^8 a 10^9 Gauss), els MSP són meravelles còsmiques. Es creu que aquestes estrelles de neutrons que giren ràpidament es formen a través d'un procés en què la transferència de massa d'una estrella companya en un sistema binari fa que l'estrella de neutrons s'acceleri, o "giri" fins a períodes de mil·lisegons. Aquest procés de "reciclatge" no només rejoveneix el púlsar, sinó que també aporta llum sobre els complexos mecanismes de l'evolució estel·lar. El descobriment i l'estudi dels MSP han avançat significativament la nostra comprensió dels cicles de vida de les estrelles, les interaccions binàries i les condicions físiques extremes en aquests objectes celestes extraordinaris. Aquesta tesi consta de dues parts, ambdues centrades en els fenòmens associats als MSP. La primera part explora una població d'estrelles de neutrons utilitzant dades d'observació de raigs X. Se sap que els cúmuls globulars (GCs) són extremadament eficients per formar MSP i binaris de raigs X de baixa massa (LMXBs), a causa de les seves altes densitats estel·lars. Com que molts d'aquests MSP i LMXB estan estretament empaquetats dins del nucli del GC, les seves contrapartides en raigs X només es poden resoldre completament mitjançant la resolució angular subarcsegon de Chandra. En aquesta tesi, es presenta un estudi profund del GC M28 (NGC 6626) que cobreix el conjunt de dades ACIS complet de 330 ks 2002-2015 de l'Observatori de raigs X de Chandra. Investiguem la lluminositat de raigs X (L_X), l'espectre i la modulació orbital dels 7 MSP binaris compactes coneguts al clúster. Descobrim una modulació de flux orbital de raigs X de doble pic a M28I (IGR J18245–2452) durant el seu estat de púlsar, centrat al voltant de la conjunció inferior del púlsar. Analitzem l'espectre de l'estrella de neutrons a la LMXB inactiva per limitar la seva massa i radi. Utilitzant models d'atmosfera d'estrelles de neutrons d'hidrogen i heli, trobem els radis de l'estrella de neutrons de R = 9,2 - 11,5 km i R = 13,0 - 17,5 km, respectivament, per a una massa d'estrella de neutrons d'1,4 $M_\odot$ (68% interval de confiança). També cerquem la variabilitat a llarg termini a les 46 fonts de raigs X més brillants i informem del descobriment de sis noves fonts de raigs X variables de baixa lluminositat a M28.

En la segona part de la tesi, s'estudia la interacció del camp magnètic de l'estrella de neutrons amb el disc d'acreció proper, realitzant simulacions detallades de magnetohidrodinàmica (MHD) que incorporen estructures de disc realistes a les simulacions numèriques. L'objectiu principal d'aquesta secció és dilucidar el mecan-

isme que impulsa les transicions d'estat en els MSP de transició, l'origen físic dels quals segueix sent en gran part desconegut. Per realitzar les simulacions, utilitzem un codi d'hidrodinàmica de partícules suavitzades (SPH) MHD axisimètric desenvolupat recentment. Mitjançant la implementació del mètode SPH al nostre codi, discutim quatre escenaris d'interacció diferents que prenen la distància de l'estrella de neutrons al radi interior del disc com 0.5, 1, 5, 25 vegades el radi del cilindre de llum. Realitzem les simulacions utilitzant un valor de camp magnètic de superfície típic per als MSP, $B_0 = 9,6 \times 10^7$ G, associat amb el valor conegut per el MSP PSR $J1023 + 0038$ i investigant la interacció camp magnètic-disc en funció de l'angle d'inclinació entre l'eix de rotació i l'eix magnètic de l'estrella de neutrons. La tesi se centra en simulacions numèriques d'estructures de disc, tant amb camps magnètics com sense. Les simulacions inicials sense camps magnètics van establir una configuració de disc estable, que va servir de base per a estudis posteriors. Les simulacions posteriors van introduir un camp magnètic amb angles d'inclinació variables per observar el seu impacte en l'estabilitat i l'evolució del disc. Les nostres troballes revelen que els rotadors alineats van mantenir l'estabilitat durant múltiples òrbites, mentre que els angles d'inclinació més alts van provocar inestabilitat al disc.

Contents

List of Figures

List of Tables

LIST OF ACRONYMS

AB Active Binary

ACIS Advanced CCD Imaging Spectrometer

AV Artificial Viscosity

BH Black Hole

BW Black Widow

BD Brown Dwarf

CCD Charged Coupled Device

CV Cataclysmic Variable

CBMSP Compact Binary Millisecond Pulsar

CFD Computational Fluid Dynamics

DEC Declination

DP Double-Peaked

EMW Electromagnetic Wave

UV Ultraviolet

GR General Relativistic

GC Globular Cluster

GBT Green Bank Telescope

IC Inferior Conjunction

IBS Intrabinary Shock

JWST James Webb Space Telecsope

LC Light Cylinder

LMXB Low-mass X-ray Binary

MHD Magnetohydrodynamics

M-R Mass and Radius

MSP Millisecond Pulsar

NS Neutron Stars

PIC Particle In Cell

RB Redback

RG Red Giant

RA Right Ascension

RPP Rotation-powered Pulsar

SPH Smoothed Particle Hydrodynamics

SPMHD Smoothed Particle Magnetohydrodynamics

SC Superior Conjunction

TMSP Transitional MSP

WD White Dwarf

qLMXB Quiescent LMXB

Chapter 1

Introduction

1.1 Low-mass X-ray Binaries

Globular clusters (GCs) stand as remarkable astronomical laboratories, offering a unique environment for the formation of low-mass X-ray binaries (LMXBs) and millisecond pulsars (MSPs). The high stellar densities within these clusters, as extensively discussed in Camilo and Rasio (2005a) and Verbunt and Lewin (2006), foster complex dynamical interactions that lead to the creation of compact objects and binary systems.

Neutron stars (NSs), the remnants of massive stars after supernova explosions, are incredibly dense objects, creating gravitational fields that are second only to black holes (BH). They are the collapsed core of a massive supergiant star with a radius of 10 km and a mass of about 1.4 $M_\odot$. In the core of a NS, the density can be extraordinarily high. It is believed to reach up to 10^{14-15} g/cm^3 [Shapiro and Teukolsky 1983]. They slow down rapidly after birth, reaching spin periods of 0.1–10 seconds, and can reach extremely strong magnetic fields (10^{15} G). LMXBs, which consist of a NS (or a BH) orbiting a low-mass companion star such as a white dwarf (WD), or brown dwarf (BD) with masses ranging from 0.01 $M_\odot$ up to a few solar masses, offer a unique laboratory to study extreme physical processes occurring under conditions of extreme gravity and temperature [Duncan and Thompson 1992, Bombaci 1996]. They also consist of main sequence, sub-giant, or red giant branch stars with masses ranging between $0.1 - 60$ $M_\odot$. These systems often emit X-rays powered by accretion, making them observable by X-ray telescopes and revealing information about the accretion flow and stellar components (See Figure 1.1). Henceforth, we will exclude BH accretors and focus solely on LMXBs comprising NSs.

One of the defining features of LMXBs is the mass transfer process between the companion star and the compact object. This mass transfer occurs via Roche lobe overflow leading to the formation of an accretion disk around the compact object. The study of mass transfer and accretion in LMXBs provides a critical avenue for investigating the dynamics of compact astrophysical systems. They are renowned for their strong X-ray emission, which stems from the accretion of material onto the compact object. This X-ray emission is often highly variable, with characteristic patterns such as Type I X-ray bursts produced by thermonuclear shell flashes in the accreted NS envelope.
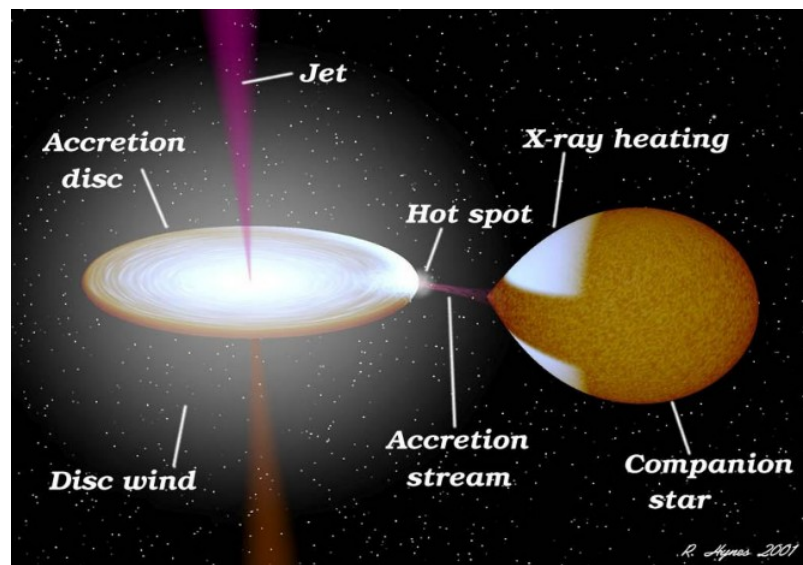
Figure 1.1: Representation of an X-ray binary. Credit: NASA/R.Hynes

Most systems, known as X-ray transients, intermittently reveal themselves during short X-ray outbursts, showing luminosities ranging from approximately 10^{34} erg s^{-1} to 10^{38} erg s^{-1}. However, they predominantly remain in a quiescent state, characterized by X-ray luminosities typically between 10^{32} and 10^{34} erg s^{-1}. During this phase, the X-ray spectrum is often dominated by a soft thermal component, characterized by a blackbody temperature around 0.1–0.3 keV. Additionally, a non-thermal component, described by a power law with a photon index of approximately 1–2, is frequently observed alongside the thermal emission [Campana et al. 1998]. In certain instances, this non-thermal component becomes predominant in the 0.5–10 keV X-ray spectrum, overshadowing any detectable thermal emission [Campana et al. 2005, Wijnands et al. 2005a;b]. Although the origin of the non-thermal component is not understood perfectly, it has been suggested that the magnetic field of the NS could be behind this non-thermal process [Campana et al.

1998]. Conversely, the thermal component likely originates from the NS's surface, potentially representing the cooling emission of its crust, heated during outbursts. Alternatively, the thermal component could also originate from low-level accretion down to the NS's surface [Wijnands and Degenaar 2013].

1.1.1 Quiescent LMXBs

Quiescent LMXBs (qLMXBs) have been identified following intense transient outbursts, frequently exhibiting type I X-ray bursts. Their quiescent spectra are generally modeled with a thermal component roughly consistent with a 10 km NS and an additional power-law component [Campana et al. 1998]. One of the central challenges in high-energy astrophysics is determining the mass (M) and radius (R) of NSs, as these fundamental parameters are linked to the equation of state (EOS) that governs the behavior of matter under extreme densities within NS interiors. Accurate measurements of M and R offer critical insights into the nature of ultra-dense matter. Techniques such as pulsar timing, X-ray, and optical observations, provide substantial constraints on NS and companion masses. Pulsar timing involves systematically monitoring the rotation of a NS by precisely tracking the arrival times of its radio pulses. It allows for the determination of the orbital dynamics and the NS's influence on its companion, enabling precise mass measurements [Lorimer and Kramer 2004].

QLMXBs within GCs present promising candidates due to their precisely determined distances (5.5±0.3 kpc for M28; Harris 2010) and comparatively modest magnetic fields (B $\lesssim 10^{10}$ G; Di Salvo and Burderi 2003). Utilizing X-ray observations, which offer spectral insights alongside theoretical models, enables the estimation of their radii [Heinke et al. 2006]. These systems typically feature a relatively faint emission (L$_X$ $\sim$ $10^{32} - 10^{33}$ erg s^{-1}) interpreted with a thermal blackbody, allowing the observed thermal emissions to serve as constraints for the NS's radius when coupled with its distance and mass [Guillot et al. 2011].

1.2 Millisecond Pulsars

Millisecond pulsars (MSPs) are recycled NSs and are thought to be born in LMXBs when the NS has gained enough angular momentum from the accreted material from the companion star. It is generally accepted that a radio MSP is born when the NS stops accreting and enters a rotation-powered state. MSPs are old NSs

with short spin periods (P_s) less than 30 milliseconds and weak surface magnetic fields ($B = 10^8$–10^9 G). Pulsars initially slow down swiftly after formation, typically reaching spin periods of 0.1 to 10 seconds [Manchester et al. 2005, Lorimer 2008; 2019]. The general theory [Alpar et al. 1982] assumes that these rapidly spinning NSs, with spin periods of milliseconds, are "recycled" through the accretion of matter and angular momentum in LMXB systems, which are therefore regarded as the progenitors of MSPs. As matter accretion diminishes, the NS transitions into a rotation-powered MSP, detectable as a radio pulsar.

1.2.1 Compact Binary Millisecond Pulsars: Stellar Predators

Compact binary MSPs (so-called spiders) represent a growing category of pulsars in tight orbits with orbital periods (P_{orb}) typically less than 1 day [Roberts 2013]. Spiders have two distinct subclasses, known as "black widows" (BWs) and "redbacks" (RBs). They have been nicknamed after cannibalistic spiders due to strong irradiation by the relativistic pulsar wind. RBs have revealed two distinct quiescent states: the "disk" and "pulsar" states [Archibald et al. 2009a]. The disk state is characterized by intermediate X-ray luminosity ($L_X \sim 10^{33}$ erg s^{-1}), notable variability including rapid X-ray mode transitions occurring on timescales shorter than P_{orb}, and the presence of broad, double-peaked optical emission lines typical of accretion disks [Linares 2014b, Linares et al. 2014a]. Conversely, the pulsar state shows radio pulsations and exhibits the lowest X-ray luminosity ($L_X \lesssim 10^{32}$ erg s^{-1}). The X-ray emission observed in the pulsar state of compact binary MSPs is believed to arise from an intrabinary shock, where the relativistic pulsar wind interacts with the wind or outflowing material originating from the companion star [Wadiasingh et al. 2017].

BWs have companions that are a very low mass semi-degenerate stars (< 0.1 $M_\odot$) and they have low X-ray luminosity $L_X \sim 10^{30} - 10^{31}$ erg s^{-1} (0.5-10 keV). The study of BW pulsars provides insights into the interplay between mass transfer, magnetic fields, and the emission of high-energy radiation [Fruchter et al. 1989]. The intense radiation processes in BWs can have a profound impact on the companion star. They may lead to the erosion and eventual evaporation of the companion's outer layers, leaving behind a highly evolved, degenerate core. The study of BWs is instrumental in understanding the influence of compact objects on the evolutionary pathways of their companions.

RBs are also known for their transformative effects on their companion stars. In these systems, the NS orbits a low-mass companion star, often a bloated main-sequence star. RBs have more massive non-degenerate companion stars ($0.1 - 0.4\ M_\odot$) and on average higher $L_X \sim 10^{31} - 10^{32}$ erg s^{-1}. RB systems can exhibit variability in their mass transfer rates, occasionally transitioning between the disk and pulsar states (Section 1.2.2). These transitions provide valuable insights into the mechanisms driving mass transfer in LMXBs and the effects on the companion star's evolution.

Recently, Zhao and Heinke (2023) showed that X-ray luminosities of spider pulsars are correlated with the minimum masses of their companion stars. In the pulsar state, the X-ray emission from the majority of RBs and BWs is predominantly non-thermal, with its luminosity exhibiting variations across orbital phases [Bogdanov et al. 2005]. This non-thermal emission is commonly attributed to the presence of an intrabinary shock (IBS) formed between the pulsar and companion winds. However, the exact shape and location of this shock remain uncertain, as they are viewed from varying perspectives along the orbit. Notably, orbital-phased light curves in most cases reveal double-peaked maxima concentrated around the pulsar's inferior conjunction (IC), suggesting that the IBS is curved around the pulsar (Romani and Sanchez 2016, Wadiasingh et al. 2017; 2018, Kandel et al. 2019, van der Merwe et al. 2020, see Section 2.1.1).

1.2.2 Transitional Millisecond Pulsars

It was found that a subclass of MSPs experience transitions from a rotation-powered to an accretion-powered or "outburst" state, as well as an intermediate subluminous disk state with high/active and low/passive modes on timescales shorter than the orbital period (P_{orb}) [Papitto et al. 2013, Linares et al. 2014a, Papitto and de Martino 2020]. A "transitional MSP" (tMSP) which was found in M28 (IGR $J18245-2452$, or M28-I hereafter; Papitto et al. 2013) is an example of this subclass. The system was known as a binary rotation-powered MSP [Bégin 2006] with an orbital period of 11 hr, and then in April 2013 showed an outburst (the *outburst state* with $L_X \sim 10^{34} - 10^{37}$ erg s^{-1}). This provided the strongest evidence of the recycling scenario for MSP formation. So far, three of the recognized RBs have undergone confirmation as transitional MSPs, switching between disk ($L_X \sim 10^{33}$ erg s^{-1}) and pulsar states ($L_X \sim 10^{32}$ erg s^{-1}) (Stappers et al. 2014, Bassa et al. 2014, Linares 2014a, Papitto and de Martino 2020, see Section 2.1.1).

1.3 Numerical Simulations of the Transitional MSPs

The magnetic field surrounding NS ranks among the strongest observed in the Universe. Any theoretical investigation or numerical simulation of a NS, as exemplified by MSPs in this study, requires the incorporation of Magnetohydrodynamics (MHD) principles and methodologies. A very important regime derived from the collisional one-fluid model is the classical MHD regime. MHD couples Maxwell's equations of electromagnetism with hydrodynamics to describe the macroscopic behavior of conducting fluids and plasmas, of special relevance in astrophysics.

The basic astrophysical foundations of MHD were developed from the 1950s through the 1980s. Nowadays, MHD simulations of plasmas are in a mature stage only limited by resolution issues and available computing resources. This thesis aims to show how MHD can be used to gain insight into the difficult topic of pulsar dynamics and, in particular, the evolution of the accretion disks that surround the NS in tMSPs. MHD simulation studies, combined with observations, will ideally give clues regarding the physical mechanism driving the transitional phenomena in MSPs.

1.3.1 The MHD approximation

The equations of MHD are a reduction of the equations of fluid mechanics coupled with Maxwell's equations (Stone 2011, see also Appendix B). Compared to general plasma physics, MHD is a significantly simplified theory. In MHD, the system is described using the standard fluid dynamics variables, such as density, velocity, and pressure, with the addition of only one extra vector: the magnetic field. This allows MHD to effectively model the macroscopic behavior of plasmas, incorporating the essential effects of electromagnetic fields on fluid dynamics without the complexity of a full plasma kinetic theory [Priest and Forbes 2000]. The "MHD approximation" involves three assumptions:

1. The fluid approximation: Assumes that the plasma can be treated as a continuous fluid, rather than a collection of individual particles. This is valid when the mean free path of particles is much smaller than the characteristic length scales of interest, and the plasma can be described by macroscopic quantities like density, pressure, and bulk velocity. The fluid approximation holds well in plasmas with high density and relatively low temperatures, where collisions between particles are frequent enough to establish local thermodynamic equilibrium.

2. Ohm's law: In MHD, Ohm's law is often simplified to include the effects of the electric field, magnetic field, and bulk motion of the plasma. This form of Ohm's law assumes that the electric field in the frame moving with the plasma is proportional to the current density. It is valid when the magnetic Reynolds number is large, implying that the magnetic field is "frozen" into the plasma and moves with it.

3. The plasma is electrically neutral: The assumption of quasineutrality implies that the net charge density in the plasma is zero or negligibly small, i.e., the number of positive charges (ions) is approximately equal to the number of negative charges (electrons). This assumption is valid in plasmas where the Debye length (the characteristic length scale over which charge imbalances are screened out) is much smaller than the system size. This is often true in many astrophysical and laboratory plasmas where the density is high and the thermal velocity of the particles is relatively low (Parker 1979, Priest and Forbes 2000, Mestel and Landstreet 2005, Spruit 2016).

1.3.2 The Smoothed Particle Hydrodynamics Method

The smoothed particle hydrodynamics (SPH) technique [Gingold and Monaghan 1977, Lucy 1977] has been widely used in astrophysics to study highly dynamical, geometrically distorted, and often catastrophic events, such as star formation [Springel and Hernquist 2003]. SPH is a computational method for solid or fluid mechanics. The basic concept is reconstructing a continuous field from a group of particles by interpolating the properties carried by these particles in any point of space at a given time. Defining a Gaussian-like interpolating kernel function with a scale factor h (called smoothing length), the continuous functions defining the main properties of the fluid can be reconstructed. The SPH method was developed in 1977 by Gingold and Monaghan (1977) and Lucy (1977). It is a mesh-free Lagrangian method initially designed for astrophysical simulations. Its applicability has since expanded to fluid dynamics considerably.

SPH is a Lagrangian particle method for solving the equations of hydrodynamics. A central point in the SPH technique is how to estimate the fluid density from an arbitrary distribution of point mass particles. Broadly speaking, there are three common approaches to computing the density (see Figure 1.2). The first one (the left panel of the figure) is the mesh-based method which creates a mesh and calculates density by dividing the mass in each cell by its volume. However,
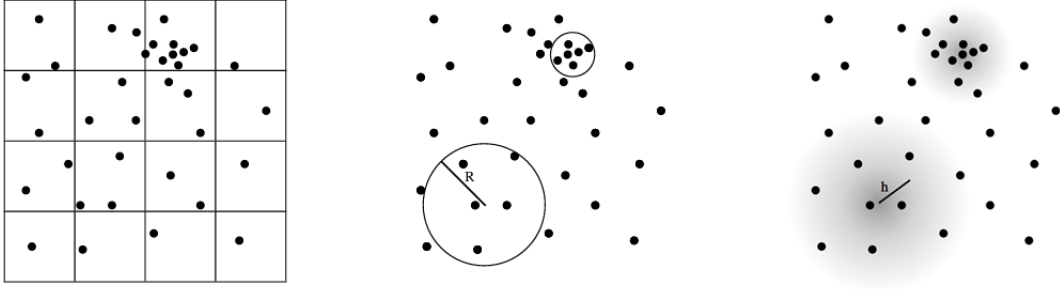
Figure 1.2: Computing a continuous density field from a collection of point mass particles. *Left panel:* In particle-mesh methods the density is computed by interpolating the mass to a grid (or simply dividing the mass by the volume). However, this tends to over/under-resolve clustered/sparse regions. *Middle panel:* An alternative not requiring a mesh is to construct a local volume around the sampling point, solving the clustering problem by scaling the sample volume according to the local number density of particles. *Right panel:* This panel shows the approach adopted in SPH, where the density is computed via a weighted sum over neighboring particles, with the weight decreasing with distance from the sample point according to a scale factor, h (smoothing length) [Price 2012a].

inefficiencies can arise in highly clustered mass distributions due to over/under-sampling in dense regions. Additionally, interpolation to and from particles can lead to a loss of accuracy, speed, and consistency. The second method (the middle panel of the figure) is local sampling without mesh. It calculates density by sampling the mass distribution locally, often within a sphere centered at the sampling point adapting to clustered or sparse regions by adjusting the sampling volume size based on local density. However, this method can produce very noisy estimates. Lastly, the third approach (the right panel of the figure) is the SPH method with a weighted summation approach which computes density using a weighted summation over nearby particles with a Gaussian-like kernel that is truncated at a finite radius. It provides a smooth, accurate density estimate and handles variations in local particle density effectively. Therefore the density is computed using a weighted summation over nearby particles, given by

$$\rho(r) = \sum_{b=1}^{N_{neigh}} m_b W(|r - r_b|, h) \tag{1.1}$$

where W is a weight function with dimensions of inverse volume and $|\mathbf{r} - \mathbf{r}'|$ is the distance between the neighboring particle ($\mathbf{r}'$) and the current particle ($\mathbf{r}$). The weight function (smoothing kernel) should have symmetry and a flat central por-

tion so the density estimate is not strongly affected by a small change in the position of the nearest neighbor. The Gaussian function fulfills all of the above properties and reads:

$$W(|r - r'|, h) = \frac{\sigma}{h^d} \exp\left[-\frac{(r - r')^2}{h^2}\right] \quad (1.2)$$

where d refers to the number of spatial dimensions and σ is a normalization factor. The kernel function serves the dual purpose of averaging values from nearby particles and determining their interactions. It is radially symmetric, peaking at the origin particle and decreasing to zero as distance exceeds a few times h. In the scope of this work, we make use of a flexible family of interpolators called "sinc kernels", which have compact support (i.e. they vanish at a distance of $2h$) and suppress the so-called pairing instability [Cabezón et al. 2017a].

A relevant physical magnitude in fluids is viscosity. SPH-based codes typically consider only bulk viscosity, which is integrated into the equations by introducing a new term known as artificial viscosity, AV, [Monaghan 1997]. Besides a standard AV routine, our code incorporates symmetrized Balsara limiters (Balsara 1995). The Balsara limiter is a technique used in numerical simulations to reduce the dissipation in regions where the flow is dominated by shear. It improves the accuracy of accretion disk simulations by reducing artificial viscosity in regions of strong shear and differential rotation, leading to a more realistic representation of angular momentum transport and disk dynamics.

Cartesian SPH variants incorporating MHD effects represent an advanced approach to simulating fluid dynamics in astrophysical contexts. These variants adapt the traditional SPH method by integrating the equations governing magnetic fields and fluid interactions. The incorporation of MHD effects involves solving the combined magnetohydrodynamic equations, which account for the interplay between magnetic fields, pressure, viscosity, and other relevant forces. This enables the simulation of the behavior of plasma in various astrophysical settings, including accretion disks around compact objects and stellar winds. By leveraging the strengths of both SPH and MHD methodologies, Cartesian SPMHD variants provide a powerful tool for investigating the dynamic interactions between magnetic fields and fluids.

In spite of the large success achieved by Cartesian SPH codes, there is a scarcity of SPH calculations taking advantage of the axisymmetric approach, which is the one used to carry out the numerical simulations in this thesis. Axisymmetric

SPH is a specialized adaptation of the traditional SPH method designed to efficiently simulate fluid dynamics in systems with rotational symmetry around an axis. In axisymmetric SPH, the three-dimensional problem is reduced to a two-dimensional one by assuming symmetry around an axis, typically the z-axis. This reduction significantly decreases computational load while maintaining accuracy in capturing the essential physics of the system. The particles are positioned and interact within this cylindrical coordinate framework, allowing for the effective modeling of phenomena such as accretion disks, jets, and rotating stars. The axisymmetric SPH method incorporates the necessary equations of motion, continuity, and energy conservation, adjusted to reflect the cylindrical geometry. By leveraging the inherent symmetry of such systems, axisymmetric SPH offers a computationally efficient and accurate means of exploring the complex dynamics of rotationally symmetric astrophysical phenomena.

Cartesian SPH:

1. Full Dimensionality: Cartesian SPH treats the problem fully three dimensions without assuming any particular symmetry from the onset. Particles are positioned in a Cartesian (x, y, z) coordinates, allowing for a more general and versatile application to various types of fluid dynamics problems.

2. Computational Complexity: Cartesian SPH requires more computational power and resources to achieve a good spatial resolution.

3. Applications: Better suited for complex, asymmetric systems where no simplifying assumptions about symmetry can be made, such as turbulent flows, general astrophysical processes, and engineering applications where precision in three dimensions is crucial.

Axisymmetric SPH:

1. Dimensional Reduction: Axisymmetric SPH reduces a three-dimensional problem to a two-dimensional one by assuming rotational symmetry around an axis (typically the z-axis). This assumption simplifies the computational problem while still capturing the essential physical behaviors of systems with this symmetry.

2. Coordinate System: It uses a cylindrical coordinate system (r, z, θ) where variations in the azimuthal angle (θ) are neglected due to symmetry. This allows for efficient simulation of systems like accretion disks, jets, and rotating stars, which can be approached in axial symmetry.

3. Computational Efficiency: By leveraging rotational symmetry, axisymmetric SPH reduces the number of particles and computational resources needed at a

given level of resolution. This makes the method very suitable to handle specific astrophysical problems where resolution issues are relevant.

4. Applications: Ideal for scenarios where the physical system has inherent rotational symmetry, such as certain astrophysical phenomena (e.g., the structure of accretion disks or the behavior of rotating fluids). In summary, the choice between axisymmetric SPH and Cartesian SPH depends on the specific characteristics and symmetry of the physical system being modeled. Axisymmetric SPH is computationally more efficient for the system possessing axial symmetry.

Implementing a consistent, well-verified axisymmetric SPMHD code may broaden the range of applications of such a technique. In astrophysics, the magnetic field around stellar objects can often be described with a dipole or toroidal geometries, both consistent with axial geometry. Good examples are the study of magnetized accretion discs around NSs (particularly relevant for this thesis) and the gravitational collapse of an initially spherical cloud of a magnetized gas, which is closely related to the formation of protoplanetary discs. Resolution issues add an extra degree of difficulty when these studies are conducted in three dimensions. In some cases, the axisymmetric approach is the only plausible option to study these scenarios (see, for example, Zanni and Ferreira 2009a, concerning simulations of accretion onto a dipolar magnetosphere with an Eulerian axisymmetric hydrodynamic code). Researchers can take advantage of hydrodynamic codes with axial geometry to carry out convergence studies of the resolution of their three-dimensional hydrodynamic codes or perform computationally affordable parameter explorations. In this thesis, we study the interaction between pulsars and disks, utilizing the MHD approach to fluid plasmas (see Chapter 3). Given the considerable computational demands stemming from resolution constraints, opting for the axisymmetric approach is a reasonable choice. Consequently, our first task was to develop and verify a novel axisymmetric SPMHD code [García-Senz et al. 2023a] (see Section 1.3.3 below).

1.3.3 Exploring Pulsar-Disk Interactions through SPMHD Simulation

Many astrophysical scenarios involving magnetic fields can be approached in axial geometry. Although the SPH technique has been successfully extended to MHD, a well-verified, axisymmetric SPMHD scheme based on such a technique did not exist when this thesis project began. Such axisymmetric SPMHD code was built and verified during the second part of the development of this thesis where we adapted
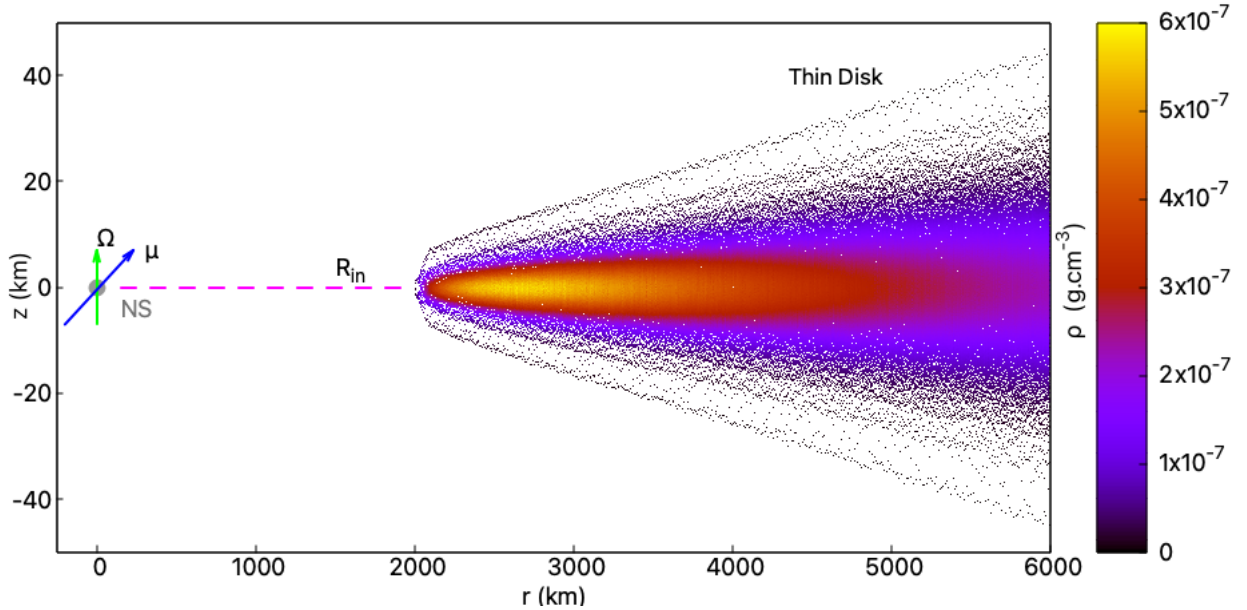
Figure 1.3: Density distribution of the accretion disk where the inner radius of the disk is at a distance of 25 R_{LC} from the NS. μ represents the magnetic moment and Ω represents the spin period of the pulsar. R_{in} is the inner disk radius. The inclination angle (ξ) is defined as the angle between μ and Ω.

it to perform SPH simulations of the pulsar-accretion disk interaction in compact binary systems with the final aim of understanding the state transitions and disk-field interactions. The code, called Axis-SPMHD, takes advantage of the existing cartesian hydrodynamic code SPHYNX described in Cabezón et al. (2017b) but written in cylindric geometry and extended to MHD [García-Senz et al. 2023a]. Interestingly, Axis-SPMHD is the first SPH code of this kind and fills a gap in the scientific literature regarding the SPH technique. As shown in García-Senz et al. (2023a) the axial code can be used to simulate many physical and astrophysical problems that display adequate geometry.

To simulate the disk's initial state, we used the thin disk approximation by Shakura and Sunyaev (1973) to build 2D-axisymmetric disks in hydrostatic equilibrium and with the inner radius of the disk located at varying distances from the NS. Most analytic accretion disk models assume a stationary and axially symmetric state of the matter being accreted into the compact object. In such models, all physical quantities depend only on the two spatial coordinates: the "radial" distance from the center r, and the "vertical" distance from the equatorial symmetry plane z. In addition, the most often studied models assume that the disk is not vertically thick. The thin disk approach considers an axisymmetric thin (= cool,

nearly Keplerian) disk. The main feature of the thin disk approximation is that all the physics that determines the time-dependent behavior of the disk depends on a single variable: the amount of shear viscosity (see Section 1.3.2 for details). Using such thin disk approximation, we study the reaction of the disk upon its interaction with the pulsar magnetic field (see Figure 1.3). The primary objective is to clarify the mechanisms that could be connected to the state transitions in transitional MSPs. This involves investigating the main physical agents that drive these transitions. In this respect, our main assumption is that the stability of the disk depends on the interplay between the pulsar's magnetic field and the disk through purely geometrical parameters such as the inner disk-pulsar distance and angle between the magnetic moment and the rotation axis of the pulsar. As shown in Section 3.3 some basic understanding and insight into the stability of the disk can be gained from that simple scenario which neglects the magnetospheric plasma around and considers Joule dissipation as the principal destabilizing agent.

A detailed analysis of the X-ray transient IGR J18245–2452 in the globular cluster M28, carried out by Linares et al. (2014a), reveals the unique behavior of this NS, which is the first known to switch between rotation-powered and accretion-powered pulsations and discusses potential mechanisms for the observed mode switching, suggesting it could be due to fast transitions between magnetospheric accretion and pulsar wind shock emission regimes. Ekşi and Alpar (2005) explored the interaction between NSs and surrounding disks under the influence of radiation pressure from radio pulsars. The study evaluates the balance of electromagnetic and kinetic energy densities to determine the inner radius of a thin disk around a NS and finds that disks can survive the radiation pressure even if their inner radius extends beyond the light cylinder, depending on the inclination angle. This survival is crucial for understanding the evolution of accretion-driven MSPs and certain transients. We aim to add new ideas to bridge theoretical simulations and observational data, enhancing the overall understanding of the transitions in NS systems.

Other notable approaches include the work of Parfrey et al. (2017), who focus on the dynamics of magnetospheres and the impact of disk-magnetosphere interactions on pulsar spin-down rates. Their simulations provide insights into the processes governing the angular momentum transfer between the star and the disk. Additionally, Papitto and Torres (2015) review the observational signatures of transitions between accretion and rotational-powered states in NS systems, emphasizing the role of multi-wavelength observations in identifying and understanding

these transitions. By integrating these various approaches, one might be possible to achieve a more comprehensive understanding of the complex behaviors exhibited by NS systems.

This thesis is organized as follows. In Chapter 2, we analyze the most recent observational data obtained by the Chandra X-ray Observatory. We explore the NS population in the GC M28 (NGC 6626). We investigate the X-ray luminosity (L_X), spectrum, and orbital modulation of the MSPs in the cluster. We analyze the spectrum of the qLMXB to constrain its M-R relation. We search for long-term variability in the 46 brightest X-ray sources and find six new variable low luminosity X-ray sources in the GC. This chapter of the thesis has been published in The Astrophysical Journal [Vurgun et al. 2022]. In Chapter 3, we discuss SPMHD simulations and bring information concerning the main features of the electromagnetic power radiated by a rotating NS and the survival chances of the disk. We perform the simulations with the novel axial SPHMD method developed by our team and published in the MNRAS journal [García-Senz et al. 2023a] using initial disk configurations in equilibrium to study the interaction between the accretion disk and the effective time-averaged magnetic field of the NS. We discuss the main results of the simulations taking the disk at different distances (R= $0.5R_{\mathrm{LC}}$, $1R_{\mathrm{LC}}$, $5R_{\mathrm{LC}}$, $25R_{\mathrm{LC}}$) and changing the angle between the spin and magnetic axes.

Chapter 2

Neutron Star Population in M28 and its Comprehensive Data Analysis

GCs are extremely efficient at forming MSPs and LMXBs, due to their high stellar densities [Camilo and Rasio 2005b, Verbunt and Lewin 2005]. Indeed, more than 200 MSPs are known in GCs [Ransom 2008, Freire 2021]. Since many of those MSPs and LMXBs are closely packed within the GC core, and their X-ray counterparts can only be fully resolved using *Chandra*'s sub-arcsecond angular resolution. $Messier$ 28 (M28, or NGC 6626), at a distance of 5.5 kpc [Harris 2010] is of particular interest among them, as it hosts one quiescent LMXB (qLMXB hereafter; source 26 from Becker et al. 2003, see also Servillat et al. 2012) and 14 known radio pulsars 7 of which are compact binary MSPs [Freire 2021].

One of the goals of high-energy astrophysics is to determine the mass (M) and radius (R) of NSs, since M and R constrain the equation of state in their interiors. One way of doing so is by fitting the surface thermal X-ray spectra from quiescent LMXBs with NS atmosphere models [Rutledge et al. 2002, Heinke et al. 2006, Steiner et al. 2018]. M and R measurements of NSs in qLMXBs rely on atmosphere modeling. In early studies, it was assumed that the NS atmosphere is composed exclusively of hydrogen, since heavier elements are expected to settle quickly below the atmosphere [Heinke et al. 2006, Rutledge et al. 2002]. Later work showed that a helium atmosphere gives significant departures in the emergent spectrum and thus systematically affects the inferred M and R [Ho and Heinke 2009, Servillat et al. 2012]. In this study, we perform a spectral analysis to constrain M and R for the known qLMXB in M28, using hydrogen and helium atmosphere models and the full available *Chandra* dataset.

In previous Chandra studies of M28, Becker et al. (2003) detected and analyzed 46 relatively bright X-ray sources in detail and found 13 variable sources. Bog-

Table 2.1: Chandra ACIS X-ray observations of M28 analyzed in this work

Obs. ID	Start Time MJD	Date	Exp. Time ks	Frame Time s	Phase$_{M28I}$[†]	Phase$_{M28H}$[†]
2684	52459.75161	2002 July 4	12.91	3.1	$0.64 - 0.96$	$0.29 - 0.45$
2685	52490.99057	2002 Aug 4	13.69	3.1	$0.65 - 0.98$	$0.93 - 1.28$
2683	52526.70489	2002 Sep 9	14.3	3.1	$0.44 - 0.73$	$0.05 - 0.12$
9132	54685.86508	2008 Aug 7	144.14	3.1	-	$0.41 - 1.10$
9133	54688.99333	2008 Aug 10	55.18	3.1	-	$0.49 - 1.93$
16748	57172.10733	2015 May 30	30.05	3.2	$0.13 - 0.86$	$0.21 - 1.18$
16749	57241.84265	2015 Aug 7	29.93	3.2	$0.92 - 1.64$	$0.81 - 1.46$
16750	57333.67060	2015 Nov 7	29.95	3.2	$0.78 - 1.52$	$0.49 - 1.53$

[†] Orbital phase range covered by each observation for M28I (with 10 bins) and M28H (6 bins).

danov et al. (2011) detected and studied 7 of the 12 MSPs known at the time [Bégin 2006], and found indications of orbital variability in the RB MSP PSR $J1824 - 2452H$. More recently, Cheng et al. (2020) detected 502 X-ray sources using the full Chandra dataset, and used them to study the dynamical properties and evolution of M28.

In 2015, we obtained 3 coordinated Chandra and Green Bank Telescope (GBT) observations of M28 in order to study M28I and the rest of the neutron star population. Here we report the results of our analysis of the full Chandra-ACIS dataset of the cluster (taken between 2002 and 2015), focusing on the neutron star population as well as the 46 brightest X-ray sources. We also report several detections of radio pulsed emission from M28I in our 2015 GBT observations; two of these observations (MJDs 57172.16 and 57333.71) are strictly simultaneous with a Chandra X-ray detection. We report the discovery of X-ray orbital modulation in the transitional MSP M28I. We present improved mass and radius constraints from spectral fits of the quiescent LMXB in M28, using both hydrogen and helium neutron star atmosphere models. We also discover six new variable X-ray sources in the cluster.

We analyzed eight observations of M28 collected with the *Chandra* X-ray Observatory taken between 2002 and 2015 with a total exposure time of 330 ks (see Table 2.1). We employed the observations performed with the Advanced CCD Imaging Spectrometer (ACIS) providing good spectral resolution[1]. We used the `CIAO`[2] version 4.13 to extract the spectra and light curves [Fruscione et al. 2006].

First, we computed the relative astrometric correction (with the tools *wcs-match* and *wcs-update*) using the longest observation as reference. We created exposure maps in the $0.2 - 8.0$ keV band using *fluximage* and produced point spread function

---

[1]ACIS Instrument Information: `https://cxc.harvard.edu/proposer/POG/html/chap6.html`.

[2]Chandra Interactive Analysis of Observations, available at `https://cxc.harvard.edu/ciao/`.

(PSF) maps using *mkpsfmap* to compute the PSF size at 2.3 keV for a 90% enclosed counts fraction for each pixel in the image. Then, we created a merged image in the $0.2 - 8.0$ keV band using the *merge-obs* tool (see Figure 2.1). We also refined the absolute astrometry of the merged X-ray image, to compare it with the radio pulsar positions. For M28A (for which the radio–X-ray association is well established), we found an offset between its radio position and its X-ray counterpart of $\Delta_{\rm RA} =$ 0.1 arcsec and $\Delta_{\rm DEC} =$ -0.3 arcsec in right ascension and declination, respectively. We then applied this correction to the astrometric frame of the X-ray dataset. We took the centroid coordinates of the X-ray counterparts of I, L and their positional uncertainties from Becker et al. (2003). Shifted X-ray positions of C, D, E, G, M and their positional uncertainties are taken from Cheng et al. (2020). The rest of the X-ray positions and their positional uncertainties are obtained in this work. We estimated positional uncertainties (95% confidence) using an empirical relation from Hong et al. (2005). Then, we calculated the angular separation between the radio and the X-ray coordinates (all reported in Table A.1).

Table 2.2: Counts, rates, and orbital parameters for the known NS systems in M28

Source	Net Count[a]	Count Rate	$\log P_{\rm B}[S/N]$[b]	Type[c]	T_0[d]	P_s	$P_{\rm orb}$	M_c[e]	Refs
		Count/s			MJD	ms	hrs	$M_\odot$	
q	13418	4e-02	-[36]	quiescent LMXB	-	-	-	-	1,2
A	9031	3e-02	-[30]	MSP	i	3.05	i	i	3,8
B	20	6e-05	-	MSP	i	6.55	i	i	3,5
C	27	9e-05	< -5	MSP, eccentric	-	4.16	193.8674	0.30	3,5
D	18	5e-05	< -5	young, eccentric	-	79.83	729.8762	0.45	3,5
E	20	7e-05	< -5	MSP	i	5.42	i	i	3,5
F	28	9e-05	< -5	MSP	i	2.45	i	i	3,5
G	23	7e-05	< -5	BW	53629.071809(10)	5.91	2.51000803(17)	0.01	3,5
H	117	4e-04	-[3]	RB	53755.2263988(13)	4.63	10.4406611(7)	0.20	3,5
I	10301	3e-02	-[7]	RB	56395.216893(1)	3.93	11.025781(2)	0.20	3,4,5
J	55	2e-04	< -5	BW	53832.2815822(36)	4.04	2.33835171(9)	0.01	3,5
K	52	2e-04	< -5	MSP	-	4.46	93.8482	0.16	3,6
L	1347	4e-03	-[5]	BW	-	4.10	5.4170	0.02	3,6
M	27	8e-05	< -5	BW	56451.272704(15)	4.78	5.82046126(3)	0.011[†]	3,7
N	-	-	-	BW	56451.2896713(15)	3.35	4.76383956(3)	0.019[†]	7

a Background-subtracted net counts extracted in the $0.2 - 8.0$ keV band. b Logarithm of the binomial no-source probability, taken from Cheng et al. (2020). Sources q,A,H,I,L are indicated by S/N ratio from Becker et al. (2003). c Types are indicated as follows: RB = Redback; BW = Black widow; MSP = Millisecond pulsar. d Epoch of zero mean anomaly. e Companion mass calculated assuming a pulsar mass of 1.35 $M_\odot$ and an inclination of 60°. † The minimum companion mass calculated assuming a pulsar mass of 1.4 $M_\odot$. i: Isolated pulsar. References: (1): Becker et al. (2003), (2): Servillat et al. (2012), (3): Paulo Freire's catalog, (4): Papitto et al. (2013), (5): Bégin (2006), (6): Bogdanov et al. (2011), (7): Douglas et al. (2022), (8): Lyne et al. (1987)

Following the standard `CIAO` data analysis threads[3], we extracted each spectrum using the *specextract* tool. Response matrices and ancillary response files

---

[3]Chandra Interactive Analysis of Observations, available at `https://cxc.cfa.harvard.edu/ciao/threads/pointlike/`.

were generated using the *mkacisrmf* and *mkarf* tools, respectively. We created circular regions for the source extraction with radii between 0.7 - 1.7 arcsec depending on the nearby surroundings. We used a region of 4 arcsec radius for the background extraction from a source-free part of the same chip. We fitted our spectra in the 0.2−8.0 keV energy range using *XSPEC 12.11.0* [Arnaud 1996], generally employing a phenomenological absorbed power-law model. For the brightest pulsar M28A, we included the Chandra pile-up model in the spectral fitting [Ho and Heinke 2009, Heinke et al. 2006, Suleimanov et al. 2014, Davis 2001]. For M28-I in the disk state, we verified that our reported spectral parameters are not affected by pile-up. We fit the spectra of the bright sources grouping them to a minimum of 15 counts per channel and using chi-squared statistics. We fit the spectra of the faint sources (less than 150 net counts) grouping so that each channel contains a minimum of 1 count and using Cash's C-statistic. We used the *tbabs* model to account for interstellar absorption [Wilms et al. 2000]. Individual observations were fitted simultaneously, leaving the spectral parameters free to vary when possible. For the power-law fits, we kept constant the equivalent hydrogen column density (N_H) at 0.25×10^{22} cm^{-2}, thus assuming that it did not vary between 2002 and 2015. All spectral fits and luminosities reported herein use a distance of 5.5 kpc [Harris 1996]. For the faint sources, we employed average fit results for each source and set upper limits on the L_X for the observation where these are not detected or with very low counts. We calculated the net counts taking the region size of 1.5 arcsec for each source (and 3.1 arcsec for M28F since it is outside the center regarding PSF sizes) and placing 90% c.l. in the range of 0.5 - 10.0 keV. Then, we divided the upper limits of the net counts by the exposure time of every single Chandra observation. Then, we calculated fluxes using WebPIMMS[4] giving N_H and Γ parameters from the average fit results.

In order to constrain the neutron star mass (M) and radius (R), we fitted the spectrum of the qLMXB using hydrogen (NSATMOS) and helium (NSX) NS atmosphere models, including the Chandra pile-up model [Ho and Heinke 2009, Heinke et al. 2006, Suleimanov et al. 2014, Davis 2001]. After verifying that they are consistent within the errors, we tied all parameters between different data sets and fixed the normalization to 1, thereby assuming that all the NS surface is emitting. We also kept the frame time frozen at 3.14 s for the observations between 2002 and 2008 and 3.24 s for the 2015 observations.

---

[4]Portable, Interactive Multi-Mission Simulator `https://heasarc.gsfc.nasa.gov/cgi-bin/Tools/w3pimms/w3pimms.pl`.
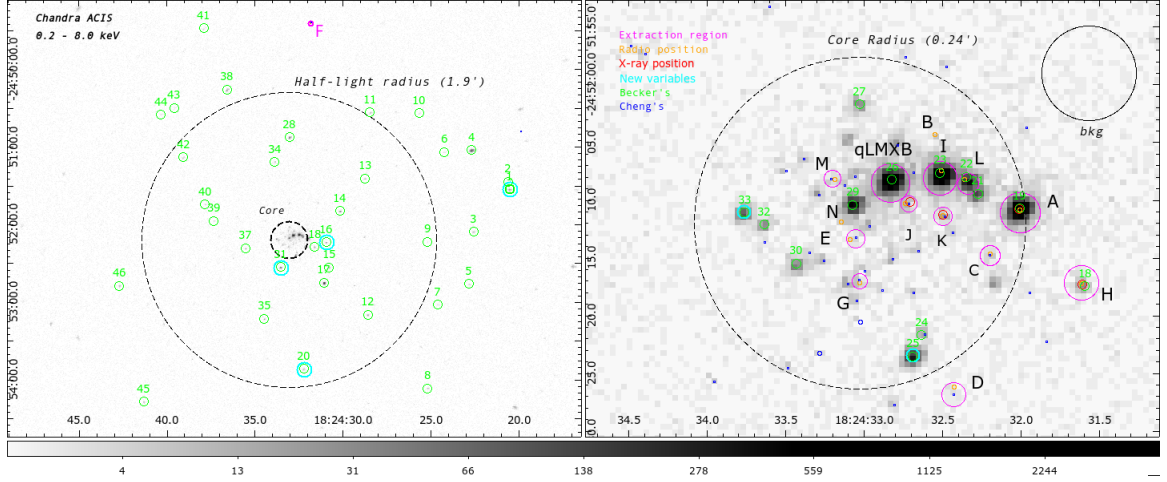
Figure 2.1: Full-band (0.2 - 8.0 keV) Chandra merged image of the globular cluster M28. *Left panel:* Black dashed circle shows the half-light radius of 1.9 arcmin of the cluster (J1824-2452F is the only known pulsar outside this circle). The green circles show the 46 X-ray sources detected by Becker et al. (2003). *Right panel:* The black dashed circle shows the core of M28 with a 0.24 arcmin radius [Harris 1996]. The small blue circles show the X-ray sources detected by Cheng et al. (2020). Magenta circles show the extraction regions and cyan circles show the new variable sources detected in this work. Red circles show the X-ray positions obtained in this work. Orange circles show the exact radio positions of the known radio pulsars. M and N's radio positions are taken from Douglas et al. (2022).

For the orbital phase-folded light curves, we studied the five brightest compact binary MSPs, namely: M28G, M28H, M28I, M28J and M28L (2 RBs and 3 BWs; see Table 2.2). We applied barycentric corrections to the photon arrival times in each event and aspect file using the *axbary* tool and we computed the orbital phase using *dmtcalc*. We computed the phases using the P_{orb} and the epoch of zero mean anomaly (T_0) of each MSP, as measured from radio timing observations (see Table 2.2). Thus, we define T_0 and orbital phase zero as the epoch of the ascending node of the pulsar. Finally, we extracted the phase-binned lightcurves using *dmextract*. To obtain the correct count rates, we calculated effective exposure times from the good time intervals for each phase bin.

We detected 12 (A, C, D, E, F, G, H, I, J, K, L, and M) of the 14 known pulsars in the cluster, by cross-correlating the significant source detections reported by Cheng et al. (2020) with the radio-timing positions of these pulsars (see Figure 2.1). Indeed, for all pulsars except B, their excess counts have a probability $< 10^{-5}$ of being produced by background fluctuations [Cheng et al. 2020]. We did not detect the newly discovered pulsar N, but we were able to measure L_X for the

new MSP M28-M [Douglas et al. 2022]. In Table 2.2, we give the wide range of net counts (18-13418) and count rates ($6 \times 10^{-5} - 4 \times 10^{-2}$ c/s) for the NSs studied in this work.

We give the radio and X-ray source positions with their uncertainties in Table A.1 of the appendix. In all 12 detected X-ray counterparts to the known pulsars in M28, the X-ray positions agree (within 2-sigma) with the much more precise radio locations. We quantified the uncertainty in the radio-X-ray cross-correlation following Bogdanov et al. (2011); we applied multiple random offsets to the radio pulsar positions (of 2.5-5 arcsec in R.A. and DEC) and compared these with the X-ray image (Figure 2.1). We find only one source match per offset due to chance, out of the 11 known pulsars in the core of M28 (where match is defined as coordinate agreement within 2-sigma).

2.1 X-ray Orbital Variability of Spiders

2.1.1 The Transitional MSP M28I

We extracted source counts from the transitional MSP M28I in the $0.2 - 8.0$ keV range (without background subtraction), including the 2002 and 2015 observations when the source was in the pulsar state (for a total exposure of 131 ksec, i.e., 3.3 times $P_{\rm orb}$). We note that this accumulated exposure time in the pulsar state has increased by 220% with respect to 2002, thanks to our 2015 observations. Furthermore, the three observations taken in 2015 cover altogether the full orbital phase range, as can be seen in Table 2.1.

We discover and report X-ray orbital modulation of M28I during the pulsar state, shown in Figure 2.2. We find evidence for a double-peaked light curve, with two maxima at orbital phases 0 and 0.6 and a broad minimum around phase 0.25. We extracted a light curve with 8 bins per orbit and found that this double peak is still apparent. This is consistent with the orbital modulation of most RBs: a double-peaked maximum centered around the inferior conjunction (IC, where the PSR is between the companion and the Earth) of the pulsar and a minimum at the pulsar's superior conjunction (SC; [Wadiasingh et al. 2017]). The peak-to-peak semi-amplitude of the modulation is 0.0015 c/s, i.e., about 71% of the average count rate (0.0022 c/s) after subtracting the background rate (9.1×10^{-5} c/s). The fractional semi-amplitude for some other RBs is typically around 50% in previous studies [Bogdanov et al. 2011, Hui et al. 2015].
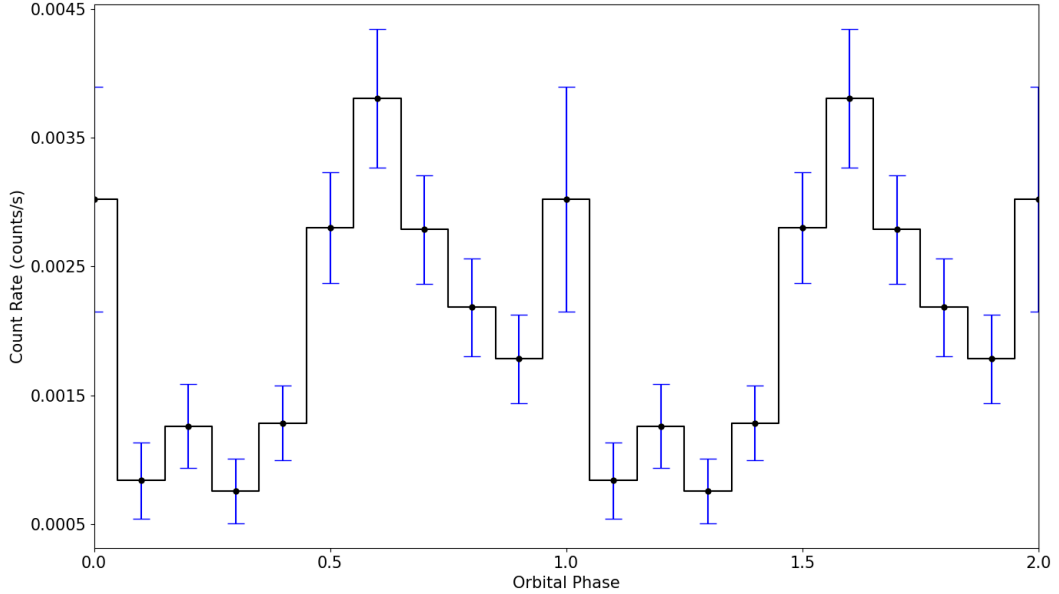
Figure 2.2: Orbital X-ray light curve of M28I in the 0.2–8.0 keV band including the observations taken in 2002 and 2015, when this transitional (and RB) MSP was in the pulsar state. Two cycles are shown for clarity.

In Figure 2.2, the orbital X-ray light curve of M28I shows a double-peaked (DP) orbital modulation centered around the pulsar's IC ($\phi = 0.75$). The maxima of the X-ray modulation are found at orbital phases $\phi = 0.6$ and $\phi = 1.0$. Between the two maxima, there is a dip around $\phi = 0.9$. Thus, based on the models of Wadiasingh et al. (2017), we infer that the intrabinary shock in M28I is curved or "wrapped" around the pulsar. We find a peak separation of 0.4 in the orbital X-ray light curve of M28I, similar to what Archibald et al. (2010) found for the RB PSR J1023+0038. In a Doppler-boosted shock with a small opening angle [Wadiasingh et al. 2017], the amplitude of the modulation is positively correlated with the inclination of the orbital plane, with the maximum possible modulation corresponding to an inclination angle of 90° [Cho et al. 2018]. We find that the orbital modulation of M28I shows a remarkably high fractional semi-amplitude (71%), which may be due to a high (nearly edge-on) inclination.

As a tMSP, M28I also experiences transitions from a rotation-powered to an accretion-powered or "outburst" state, as well as an intermediate sub-luminous disk state with high/active and low/passive modes [Papitto et al. 2013, Linares et al. 2014a, Papitto and de Martino 2020]. Figure 2.3 shows an overview of its L_X in the different states, as revealed by *Chandra* observations in 2002, 2008, 2013,
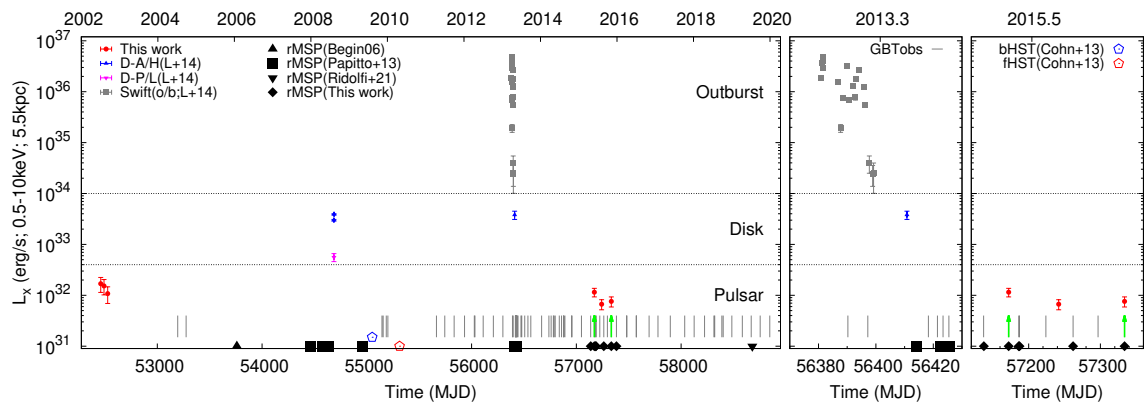
Figure 2.3: *Left panel:* X-ray luminosity (L$_X$) of the transitional MSP M28I as measured by *Chandra* and *Swift* between 2002 and 2015, together with the dates when the radio MSP was detected (shown with black filled symbols labeled "rMSP", with different origins as indicated; vertical grey lines show GBT observation dates). Red circles, blue/magenta triangles, and gray squares show the L$_X$ measurements taken in the pulsar, disk, and outburst states, respectively. The horizontal dashed lines show the approximate Lx boundaries between these states [Linares 2014b]. Blue/red pentagons show the bright/faint HST detections indicating that M28I was in the disk/pulsar state in 2009/2010 [Cohn et al. 2013]. *Middle panel:* Zoom into the outburst light curve (*Swift* observations shown with gray squares) showing the detection of a disk-active/high state 10 d after the end of the outburst (blue triangle, from a *Chandra* - HRC observation; Linares et al. 2014a) and the detection of the rMSP 4 d thereafter [Papitto et al. 2013]. *Right panel:* Zoom into the 2015 coordinated (*Chandra*+GBT) campaign. The green arrows show the strictly simultaneous radio/X-ray observations reported in this work.

and 2015. We found that M28I was in the pulsar state in 2015, and we detected for the first time radio pulsations simultaneously with an X-ray observation. Since also two of the GBT observations (57172.16 and 57333.71) were simultaneous with those from *Chandra*, the pulsar was definitively in the active radio pulsar state at the time of the X-ray observations, and likely throughout most of 2015. The radio timing observations of M28, and detections of M28I, from our GBT campaign are shown in Figures 2.3 and A.1 (see Vurgun et al. (2022) for the radio analysis details). So far, M28I was detected in the disk state in 2 of the 4 epochs when it has been observed with *Chandra*: in 2008 and 2013. Cohn et al. (2013) and Pallanca et al. (2013) found another possible occurrence of the disk state in 2009, using HST optical observations of M28. At present, *Chandra* observations are the most reliable and efficient way of constraining the duty cycle of these two states. The detection of radio pulsations with GBT reveals the pulsar state (by definition), but a non-detection does not allow a state identification since the pulsar is occulted/eclipsed for a large fraction of the orbit. This can be seen in the right panel of Figure 2.3, where we show an L_X measurement indicative of the pulsar state (*Chandra*), strictly simultaneous with a radio pulsar non-detection (GBT). As seen in Figure 2.7, the X-ray photon index Γ is approximately constant throughout the pulsar-disk-pulsar state transitions (the fitted spectra are shown in Figure A.2, panels *c* and *d*).

2.1.2 The Redback MSP M28H

We extracted the counts from the RB MSP M28H in the $0.2 - 10.0$ keV range, including all observations with a total exposure of 330 ksec. The X-ray orbital variability of the RB MSP M28H was studied by Bogdanov et al. (2011) using the 2002 and 2008 observations. They found a minimum around orbital phase 0.25 and a maximum at phase 1.0. We performed the same analysis as explained in §2 in order to compare with their results, using 6 orbital phase bins.

Our results are shown in Figure 2.4: we find a broad minimum in the orbital X-ray light curve at phase $0 - 0.4$ and a maximum around phase 0.75 (pulsar at IC). The peak-to-peak semi-amplitude of the modulation is 0.0004 c/s corresponding to a fractional amplitude of 80% of the average count rate (0.0006 c/s) after correcting the background rate (0.0001 c/s). The light curve shape is consistent with the results of Bogdanov et al. (2011), with a difference in the peak phase of about 0.25. In this case, we do not find a double-peaked light curve, within the lower phase resolution imposed by the lower X-ray luminosity of M28H compared to M28I in the pulsar state.
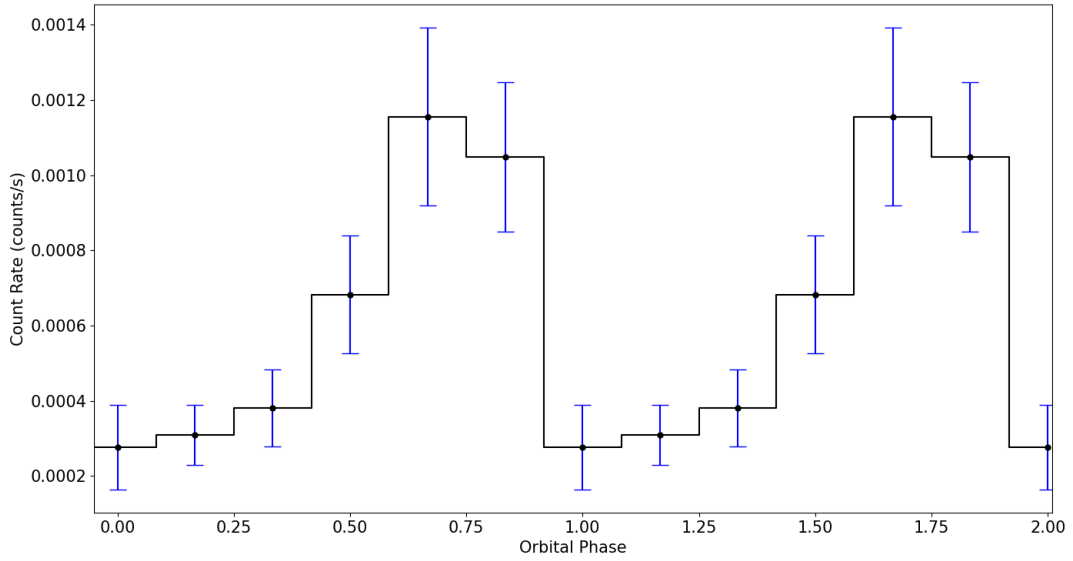
Figure 2.4: Orbital X-ray light curve of M28H in the 0.2–10.0 keV band including all observations. Two cycles are shown for clarity.
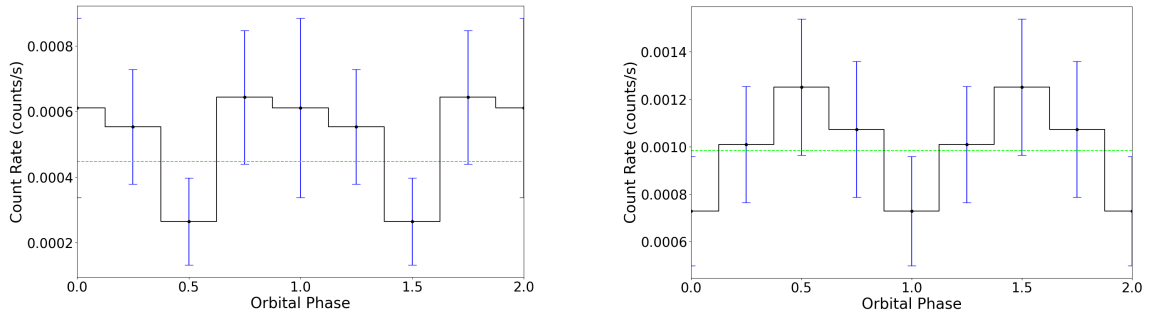
Figure 2.5: *Left panel:* Chandra ACIS-S merged two orbital cycle light curves of M28G with a bin number 4 including all observations. *Right panel:* Chandra ACIS-S merged two orbital cycle light curve of M28J with a bin number 4 including all observations.

The eclipsing binary pulsar M28H is in a 10.4-hour circular orbit around a non-degenerate star with a minimum inferred mass of $0.17 M_\odot$. The orbital separation of the system is $2.9 R_\odot$ for an assumed inclination of 60° [Bégin 2006]. We find an L_X for this RB of $[2.3 \pm 0.4] \times 10^{31} \text{ erg s}^{-1}$ for a 5.5 kpc distance, consistent with those measured in other RBs and BWs.

In contrast with M28I, we find an orbital modulation with one single peak in the orbital X-ray light curve of M28H. As seen from Figure 2.4, the maximum occurs when the pulsar is at IC ($\phi = 0.75$), and we find a broad minimum of the X-ray

emission around SC ($\phi = 0 - 0.3$) where the radio eclipses are seen [Bogdanov et al. 2011].

2.1.3 The Black Widow MSPs M28G, M28J and M28L

We performed the same orbital-phased light curve analysis for the BW MSPs M28G and M28J, including all observations (Figure 2.5). These are fainter and less luminous than the RBs (with typical $L_X < 10^{31}$ erg s^{-1} so we used in this case 4 orbital phase bins.

The count rates of these two BWs in the 4 phase bins are approximately constant, as can be seen in Figure 2.5. We fit both X-ray orbital light curves with a constant and find a χ^2/dof of 3.5/3 and 2.2/3 for M28G and M28J, respectively. We conclude that these two BWs show no evidence of X-ray orbital variability within the currently available data.

We did not investigate X-ray orbital modulation for the BW MSP M28L since it is suffering from the contamination of the very nearby RB M28I. This effect is even more clear in the 2008 epoch when M28I was in the disk state, as seen in Figure 2.6. The radio position of M28L (see Table A.1) suggests that its count rates are strongly exposed to source confusion. Indeed, the distance between the radio positions of these two sources is 1.8 arcsec, while the PSF size (FWHM) is 1.5 arcsec assuming a circular Gaussian representing the PSF[6].
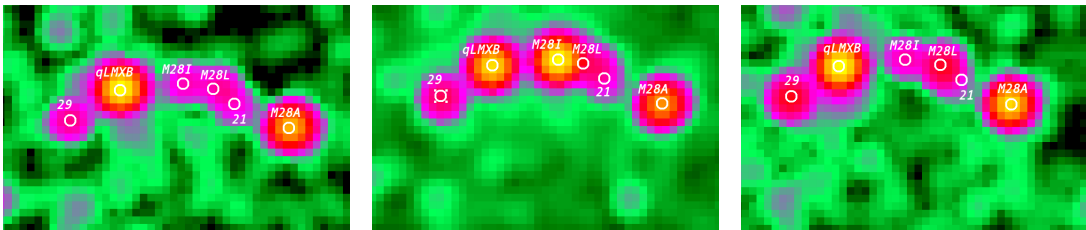
Figure 2.6: Chandra-ACIS archival observations of the core of M28 in three epochs taken in 2002 (OBS ID:2684), 2008 (OBS ID:9132), and 2015 (OBS ID:16750) from left to right. Blue circles here in the core show the sources from Becker et al. (2003) from the right to the left: M28A, S21, M28L, M28I, qLMXB, and S29. We see a blend of three sources: M28I, M28L, and S21.

---

[6]https://cxc.cfa.harvard.edu/ciao/ahelp/psfsize_srcs.html.

2.2 Spectra and Luminosities

We analyzed the spectra of the spider MSPs and the other known pulsars in M28, respectively, for each observation where they were detected. We fit all the spectra from each source jointly within *Xspec*, keeping the power law index and normalization linked between different observations and the N_H frozen to the cluster value. We thereby find the 2002-2015 average flux, L_X, and photon index for each system, which we present in Table 3. We find photon indices in the range 1-4 and L_X between 9×10^{29} erg s^{-1} and 2×10^{33} erg s^{-1}, for the full variety of pulsar types and states (see Appendix A for the spectra). Next, we present our results for the transitional MSP and the other known compact binary MSPs in more detail.
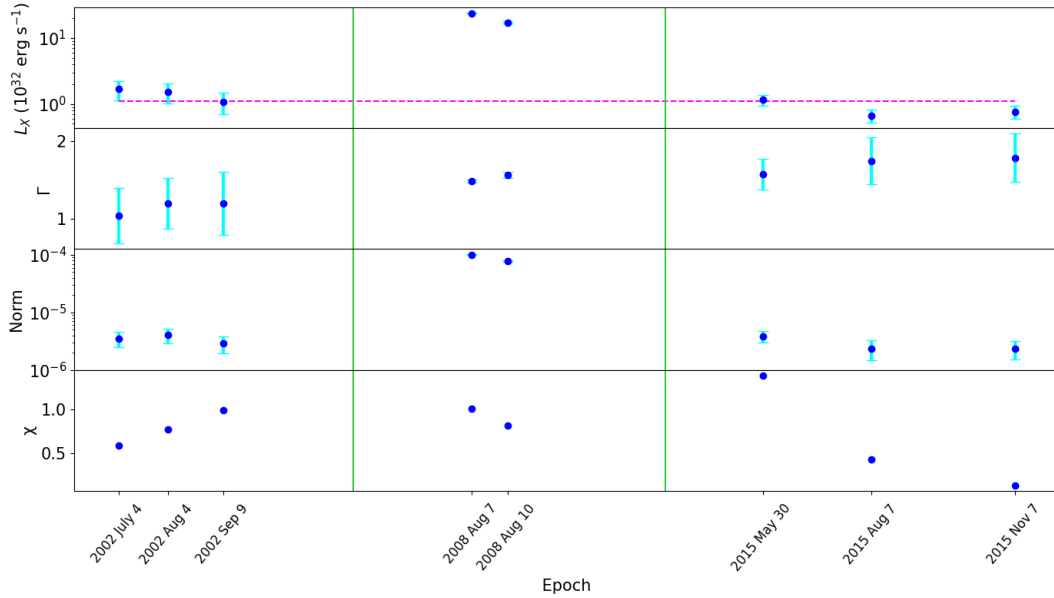
Figure 2.7: Variability of M28I. *Top panel:* Luminosity in 10^{32} erg s^{-1}. Pink dashed-line shows the average luminosity of 101.11×10^{32} erg s^{-1}. *Second panel:* Photon index parameter of the power-law model. *Third panel:* Normalization parameter of the power-law model. *Bottom panel:* Reduced Chi-squared. The green vertical lines separate the epochs visually.

We inspected the spectra of the transitional and redback MSP M28I by dividing them into three epochs: 2002, 2008, and 2015 (Table 2.3). We find that M28I was back in the pulsar state in 2015 with $L_X=[8.3\pm0.9] \times 10^{31}$ erg s^{-1}, an X-ray luminosity similar to that measured from the 2002 observations, and a photon index $\Gamma = 1.7\pm0.2$. This is the lowest L_X measured for M28I to date (see Figure 2.7). From our reanalysis of the 2002 observations, we measure $L_X=[1.3 \pm 0.2] \times 10^{32}$ erg s^{-1}

Table 2.3: Results of the averaged spectral fits for the known pulsars detected by Chandra

Name	Γ	Flux[a] erg cm^{-2} s^{-1}	L_X erg s^{-1}	Fit statistic/dof
M28A	1.33 ± 0.03	$[4.6\pm 0.1]\times10^{-13}$	$[1.66\pm 0.06]\times10^{33}$	$446/480(\chi^2)$
M28C	2.8 ± 0.9	$[6.0\pm 2.0]\times10^{-16}$	$[2.0\pm 0.7]\times10^{30}$	$11/16(CS)$
M28D	4.2 ± 1.3	$[3.0\pm 1.0]\times10^{-16}$	$[9.3\pm 4.3]\times10^{29}$	$14/11(CS)$
M28E	2.6 ± 0.8	$[5.0\pm 2.0]\times10^{-16}$	$[1.8\pm 0.7]\times10^{30}$	$19/18(CS)$
M28F	2.55 ± 0.9	$[3.0\pm 3.0]\times10^{-16}$	$[1.3\pm 1.2]\times10^{30}$	$20/26(CS)$
M28G	3.5 ± 0.7	$[5.0\pm 2.0]\times10^{-16}$	$[1.7\pm 0.6]\times10^{30}$	$23/18(CS)$
M28H	1.0 ± 0.2	$[6.0\pm 1.0]\times10^{-15}$	$[2.3\pm 0.4]\times10^{31}$	$99/101(CS)$
M28I-p[*]	1.1 ± 0.2	$[4.0\pm 0.8]\times10^{-14}$	$[1.44\pm 0.3]\times10^{32}$	$67/82(CS)$
M28I-d[†]	1.51 ± 0.02	$[5.9\pm 0.1]\times10^{-13}$	$[2.14\pm 0.04]\times10^{33}$	$485/367(\chi^2)$
M28I-p[*]	1.7 ± 0.2	$[2.3\pm 0.3]\times10^{-14}$	$[8.3\pm 1.0]\times10^{31}$	$16/12(\chi^2)$
M28J	2.8 ± 0.3	$[1.0\pm 0.3]\times10^{-15}$	$[3.6\pm 1.0]\times10^{30}$	$52/51(CS)$
M28K	2.9 ± 0.4	$[1.1\pm 0.2]\times10^{-15}$	$[4.1\pm 0.8]\times10^{30}$	$35/36(CS)$
M28L	1.55 ± 0.06	$[5.0\pm 0.8]\times10^{-14}$	$[1.8\pm 0.3]\times10^{32}$	$67/71(\chi^2)$
M28M	3.6 ± 1.3	$[7.4\pm 1.9]\times10^{-16}$	$[2.7\pm 0.7]\times10^{30}$	$4/12(CS)$

a Unabsorbed flux in the 0.5-10.0 keV band. * Includes 2002 observations (M28I-p: Pulsar state). † Includes 2008 observations (M28I-d: Disk state). * Includes 2015 observations (M28I-p: Pulsar state). CS and χ^2 indicate the fit obtained with C-statistic and Chi-Squared statistics, respectively.

(slightly lower than that measured by Linares et al. 2014b, yet consistent at the 2-sigma confidence level). We measure L_X=[2.14±0.04] × 10^{33} erg s^{-1} from the 2008 spectra of M28I, i.e., a disk state luminosity consistent with the findings of Linares et al. (2014b). We also analyzed the spectra from 2002 and 2015 jointly and found an average pulsar state luminosity of [1.1±0.2] × 10^{32} erg s^{-1} and a photon index of 1.3±0.3. We inspected the hardness ratio taking the energy bands 0.2 - 2.0 keV and 2.0 - 8.0 keV and found no significant spectral variability along the orbit.

During the X-ray association analysis, we find that the radio position of M28L agrees with source 22 from Becker et al. (2003) (see Table A.1 in appendix). Thus,

we study the possible X-ray counterpart of the black widow M28L using a 0.9 arcsec radius region which includes the radio position and source 22 from Becker et al. (2003) (manually centered to minimize contamination from nearby sources). We find an average luminosity of $L_X = [1.8 \pm 0.1] \times 10^{32}$ erg s^{-1} and a photon index of 1.55 ± 0.06 (see Table 2.3 and Figure A.5). As mentioned above and as noted previously [Bogdanov et al. 2011], this region is severely crowded and there may be contamination from other sources (mainly M28I and perhaps also source 21, see Figure 2.6). Thus, this luminosity must be interpreted with care, and we consider the counterpart to M28L as tentative.

The spectra of the RB M28H are well fitted by the power-law model yielding an $L_X = [2.3 \pm 0.4] \times 10^{31}$ erg s^{-1} with a photon index $\Gamma = 1.0 \pm 0.2$. We set an upper limit on L_X for the second 2015 observation, which appears consistent with a constant luminosity (see Figure A.5). For the BWs, M28G and M28J, we measure average luminosities of $L_X = [1.7 \pm 0.6] \times 10^{30}$ erg s^{-1} and $[5.2 \pm 1.0] \times 10^{30}$ erg s^{-1}, respectively. We find photon indices in the $2.5 - 4$ range (Table 2.3), indicating softer spectra than the redbacks above. We analyzed the spectrum of the newly discovered BW M28M using the best available data from 2008 fitting with a power-law model (Figure A.4). The best-fit yields $L_X = [2.7 \pm 0.7] \times 10^{30}$ erg s^{-1} which is similar to the measured luminosities of the other BWs in M28 and in the GC 47 Tucanae [Bogdanov et al. 2006]. We also set upper limits on L_X for the observations where these are not detected (see Figure A.5).

2.3 Pulsed Radio Emission from M28-I

We reanalyzed seven different GBT observations of M28 from 2015, at MJDs 57137.49, 57172.16, 57186.14, 57187.13, 57261.90, 57333.71, and 57382.80, spanning from 2015 April 25 to 2015 December 26 using SPIDER_TWISTER and PRESTO (see Figure A.1). M28I was detected in each of the observations, although with large amounts (i.e. factors of several) of flux variability, even when the highly irregular eclipses had not completely eliminated the pulsed radio emission in portions of the scans.

Since two of the GBT observations (57172.16 and 57333.71) were simultaneous with those from *Chandra*, the pulsar was definitively in the active radio pulsar state at the time of the X-ray observations, and likely throughout most of 2015. The radio timing observations of M28, and detections of M28I, from our GBT campaign are shown in Figure 2.3.
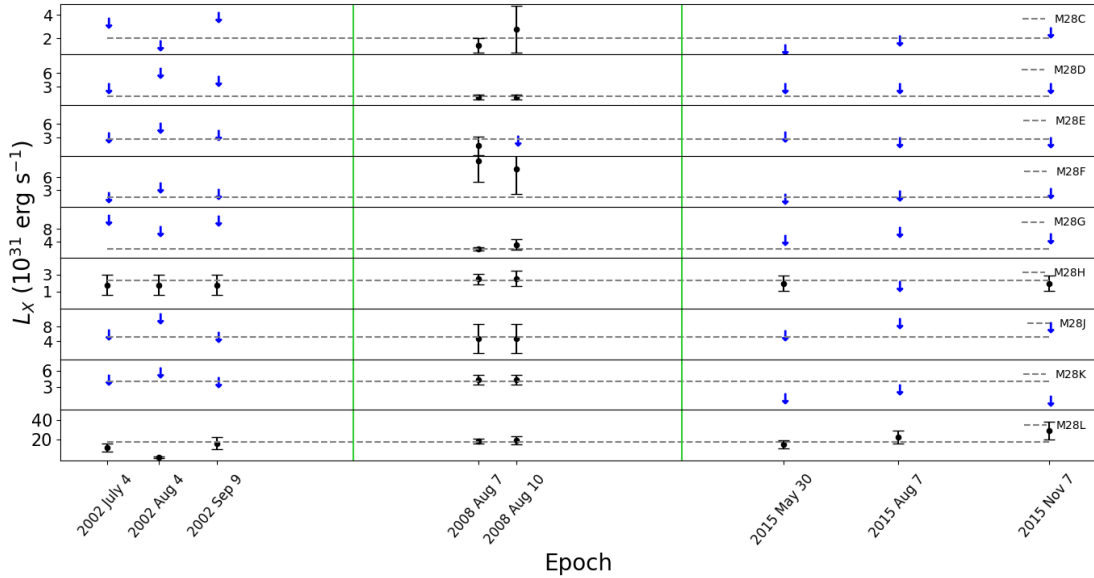
Figure 2.8: Luminosity evolution for the faint pulsars. Blue arrows show upper limits, black filled circles indicate detections. Horizontal dashed lines indicate the average luminosity for individual sources. The green vertical lines separate the epochs visually.

2.4   Neutron Star Mass and Radius

We present the X-ray spectral analysis of the qLMXB in M28, and the resulting NS mass (M) and radius (R) constraints. Measuring the X-ray flux of the qLMXB, we found that the source shows no significant variability across observations between 2002 and 2015. We find a 25% decrease in count rate in the 2015 observations, which we attribute to molecular contamination[7] of the ACIS detector (see Figure A.6). We analyze the full *Chandra* dataset, for a total exposure time of 330 ks (39% longer than what was available for previous studies, Servillat et al. 2012). The increase in collected net counts is lower (30%), due to the drop in the count rate mentioned above.

In order to study the effect of different atmosphere compositions on M-R constraints, we performed the spectral fits using two different models, NSATMOS [Ho and Heinke 2009] and NSX [Heinke et al. 2006], which model a hydrogen and helium NS atmosphere, respectively. These models are valid for negligible magnetic fields (less than 10^9 G), in agreement with the weak fields expected for NSs in qLMXBs [Di Salvo and Burderi 2003]. We also included the pile-up component in

---

[7]https://cxc.harvard.edu/proposer/POG/html/chap6.html#tth_sEc6.5.1.

every spectral fit. We show the folded X-ray spectra, best-fit models, and residuals in Figure 2.9.
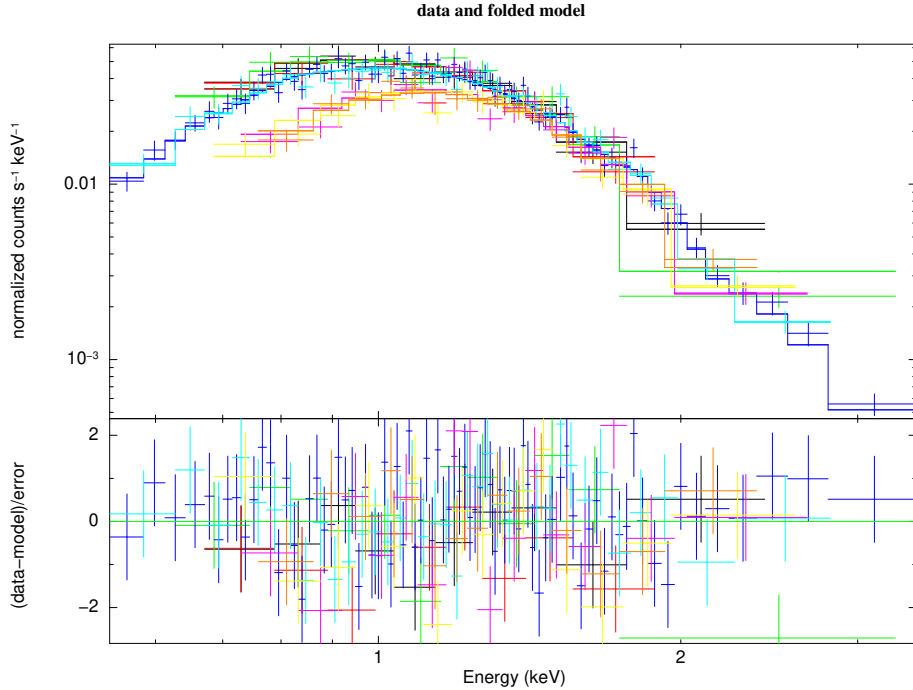
Figure 2.9: X-ray spectra of the qLMXB fitted to a hydrogen atmosphere model (PILE-UP(TBABS*NSATMOS)). Colors indicate different data sets taken with *Chandra*-ACIS observatory.

We first fitted the 2002-2008 spectra to compare directly with Servillat et al. (2012). We left the α parameter of the pile-up model as well as N_H free to vary, to include their uncertainties in our results for M and R. For the hydrogen and helium atmosphere models, our results are consistent with the M and R constraints of Servillat et al. (2012) within the errors (see panels a and c in Figure 2.10).

From now on, we will present the results of our best fits to the full dataset. The 68%, 90%, and 99% confidence regions in the M-R plane are shown in Figure 2.10 for the hydrogen and helium model fits. Next, we present single parameter constraints at the 68% confidence level. From our spectral fits with a hydrogen atmosphere model, we find that R is between $9.2 - 11.5$ km for the once canonical NS mass of 1.4 $M_\odot$. We found $N_H = [0.32 \pm 0.02] \times 10^{22}$ cm^{-2} and a temperature, $T = 0.13 \pm 0.01$ keV. For the helium atmosphere model, which is performed with the same fitting procedure as hydrogen, we found higher radii $R = 13.0 - 17.5$ km for $M = 1.4 M_\odot$ at the same confidence level with an $N_H = [0.35 \pm 0.02] \times 10^{22}$ cm^{-2} and a $T = 0.10 \pm 0.01$ keV. The 0.5–10.0 keV absorbed flux of the source (after

a)

b)

c)

d)
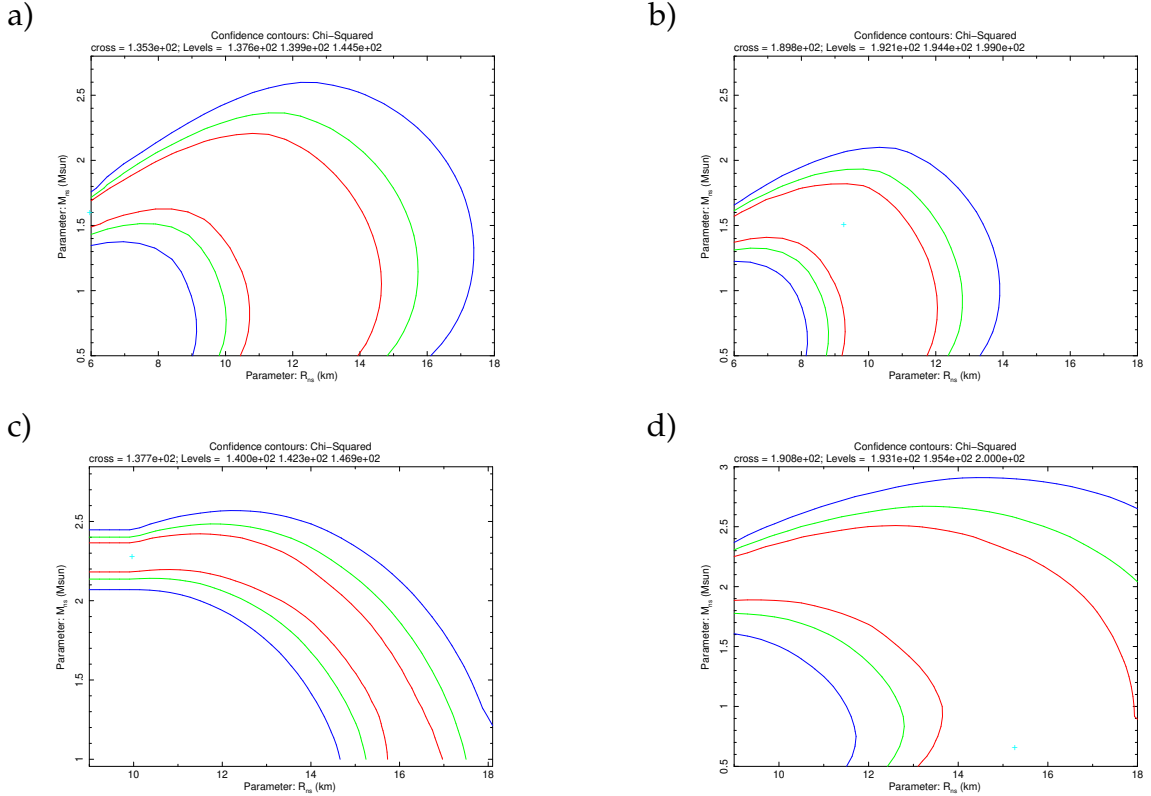
Figure 2.10: Confidence levels (68%,90%, 95% in red, green and blue, respectively) for the mass and radius constraints of the qLMXB, using Hydrogen (upper panel), and Helium (bottom panel) atmosphere models. *Left panels:* Only 2002 and 2008 Chandra observations are included. *Right panels:* All Chandra observations are used. Top left panel: Hydrogen atmosphere model with an $N_H = 0.26 \times 10^{22}$ cm^{-2} (2002-2008). Top right panel: Hydrogen atmosphere model with an $N_H = 0.32 \times 10^{22}$ cm^{-2} (2002-2015). Bottom left panel: Helium atmosphere model with an $N_H = 0.26 \times 10^{22}$ cm^{-2} (2002-2008). Bottom right panel: Helium atmosphere model with an $N_H = 0.35 \times 10^{22}$ cm^{-2} (2002-2015).

removing pile-up effect) is $[1.8 \pm 0.2] \times 10^{-13}$ erg cm^{-2} s^{-1}, which corresponds to $L_x = [6.5 \pm 0.7] \times 10^{32}$ erg s^{-1}.

Our analysis showed that the qLMXB is in a long quiescent regime and its luminosity remains stable over the 13 years. For both *hydrogen* and *helium* models, we obtained fit parameters that are consistent with the expected value range for a typical neutron star (see Figure 2.10). For the hydrogen atmosphere model and M=1.4 M$_\odot$, our constraint on the radius is in the range R=$9.2 - 11.5$ km at the 68% confidence level. From the *helium* model instead, we find higher radii for a 1.4 M$_\odot$ NS, in the range R=$13.0 - 17.5$ km. We note that our updated He model constraints are broader and consistent with lower values of R when including the full

updated dataset, compared to the previous constraints obtained from the 2002-2008 data [Servillat et al. 2012]. We conclude that, as noted by Ho and Heinke (2009) and Servillat et al. (2012), the composition of the NS atmosphere is still the main systematic uncertainty in determining M and R. Other systematic effects, which we do not explore in this work, include the presence of hot spots, distance uncertainty, abundances of the interstellar medium, and absolute flux calibration [Heinke et al. 2014, Bogdanov et al. 2016, Steiner et al. 2018]. We also found different temperatures in the Hydrogen and Helium atmosphere models, 0.13 ± 0.01 keV and 0.10 ± 0.01 keV, respectively (at 1-sigma confidence level).

Recently, joint *NICER* and *XMM* measurements have given constraints on R with a different method: pulse profile modeling with rotating hot spot models [Riley et al. 2021, Miller et al. 2021]. Their reported radius R= $13.7^{+2.6}_{-1.5}$ km is formally consistent with both our H and He constraints. An independent measurement of the NS atmospheric composition would improve the constraints on M and R from this and other thermally emitting qLMXBs.

2.5 New Variable X-Ray Sources

We searched for a long-term L_x variability on timescales of years (2002-2008-2015) using the 46 X-ray sources detected by Becker et al. (2003). We performed a spectral analysis for all 46 X-ray sources fitting the spectrum of each observation with a simple power-law model. Then, we estimated the significance (S) of the flux variations as:

$$S = [\frac{F_{max} - F_{min}}{(EF_{max}^2 + EF_{min}^2)^{1/2}}] \tag{2.1}$$

Here, F_{max} and F_{min} are the maximum and minimum X-ray fluxes, and EF_{max} and EF_{min} are their corresponding errors (see, e.g., Saeedi, Sara et al. 2022).

We find that 13 of the 46 brightest X-ray sources are variable, based on the threshold S>3 (marked with "v" in Table 2.4). Among these, 6 sources were already identified as variables in previous studies (4, 17, M28L, M28I, 29, and 32; see Becker et al. 2003 and Papitto et al. 2013). Source 21, in a crowded region inside the core of M28, is likely contaminated by the nearby and variable M28L (see Figure 2.6), so its variability is questionable and flagged with a question mark in Table 2.4. We thus find 6 new variable X-ray sources in M28, namely: 1, 16, 20, 25, 31, and 33.

Table 2.4: Variability of X-ray sources in M28.

#	$F_{max}-F_{min}$	$(EF^2_{max} + EF^2_{min})^{1/2}$	S*	Var*	#	$F_{max}-F_{min}$	$(EF^2_{max} + EF^2_{min})^{1/2}$	S*	Var*
1	3.10	0.90	3.2	v†	24	0.73	0.29	2.5	
2	1.50	1.30	1.1		25	3.50	0.50	7.2	v†
3	0.23	0.14	1.6		26	3.25	0.80	2.7	
4	24.0	5.0	5.3	v	27	0.11	0.30	0.3	
5	0.20	0.09	2.3		28	4.50	1.90	2.3	
6	0.32	0.25	1.3		29	4.80	0.60	8.4	v
7	0.13	0.14	0.9		30	1.00	0.50	2.2	
8	0.38	0.14	2.7		31	0.92	0.27	3.4	v†
9	0.45	0.19	2.4		32	3.30	0.90	3.5	v
10	3.22	0.37	1.9		33	0.79	0.21	3.8	v†
11	0.29	0.17	1.7		34	0.19	0.18	1.1	
12	1.10	0.40	2.5		35	0.23	0.12	1.8	
13	0.22	0.09	2.5		36	0.21	0.16	1.3	
14	0.78	0.34	2.3		37	0.49	0.30	1.6	
15	0.50	0.35	1.4		38	0.93	0.36	2.5	
16	0.85	0.26	3.3	v†	39	0.14	0.10	1.3	
17	6.40	1.40	4.5	v	40	0.57	0.40	1.4	
18	0.85	1.55	0.5		41	0.23	0.17	1.3	
19	9.52	0.23	2.0		42	0.91	0.78	1.2	
20	2.30	0.70	3.4	v†	43	0.11	0.17	0.7	
21	2.90	0.40	6.4	v?	44	0.16	0.18	0.9	
22	6.40	1.40	4.6	v	45	0.22	0.17	1.2	
23	48.0	10.0	44.6	v	46	0.19	0.14	1.4	

The first column shows source ID number from Becker et al. (2003). * Significance of the flux variations. * Variability. † Newly discovered variable sources. F_{max} and F_{min} indicate maximum and minimum fluxes in units of 10^{-14} erg cm^{-2} s^{-1}. EF_{max} and EF_{min} are their corresponding errors.

We show zoomed multi-epoch ACIS images of these new variables in Figure 2.12, together with their best-fit L_X and Γ. We also mark their locations in Figure 2.1.

GCs are rich environments in terms of interacting binary systems such as LMXBs, cataclysmic variables (CVs), active binaries (ABs), MSPs, and perhaps black hole binaries [Verbunt and Lewin 2005, Bahramian et al. 2020]. In the search for variable sources in the GC M28 through the years 2002 - 2015, we have found six new variable sources with luminosities $L_X < 10^{33}$ erg s^{-1} (see Figure 2.12). In this Section, we discuss their possible nature. In Figure 2.11, we show minimum and maximum X-ray luminosity values with photon indices for the variable sources that we detected. We do not see any photon index $\Gamma > 3$, which suggests that the variability is caused by non-thermal emission in these sources. The X-ray luminosities are between $10^{30} - 10^{33}$ erg s^{-1}. For all these variable sources, as the L_X increases their photon index Γ increases (except source 32 where Γ is constant).

In case of source 1, which is located outside the half-light radius of the cluster (Fig. 2.1), L_X increases monotonically from $[1.8 \pm 0.8] \times 10^{30}$ to $[1.1 \pm 0.2] \times 10^{32}$ erg s^{-1}, i.e. a factor of about 60 over 13 years. Source 20 shows a similar mono-

tonic increase in L_X, by about a factor of 30. In both cases, the photon index stays approximately constant (within the errors) in the range 1-2.5. This strong variability and relatively high L_X (reaching 10^{32} erg s^{-1}) is perhaps reminiscent of quiescent LMXBs. While qLMXBs can be strongly variable and reach high Lx values, typically they get harder as they get brighter (see Rutledge et al. 2002; Fridriksson et al. 2010; Bahramian et al. 2014; and most generically, Wijnands et al. 2015). Sources 16 and 31, are both just outside the core and increasing their luminosity in 2008, then becoming fainter again in 2015. Source 25 is within the core radius and its luminosity fluctuates between $L_X \sim 10^{31} - 10^{32}$ erg s^{-1}, changing by about a factor 4.

In the case of source 33, within the core radius, it is found to be blended with source 32 in the 2002 observation as seen in Figure 2.12. Source 32 was also detected as a variable in 2003 by Becker et al. (2003), and it was not detected in the 2008 and 2015 observations. Taking advantage of the absence of source 32, we find variability in the flux of source 33 increasing its brightness from 2008 to 2015. In the 2008 epoch, L_X of source 33 is $[7.8 \pm 0.2] \times 10^{30}$ erg s^{-1} with a $\Gamma = [2.5 \pm 0.2]$. In the 2015 epoch, L_X is $[2.9 \pm 0.8] \times 10^{31}$ erg s^{-1} with a $\Gamma = [2.1 \pm 0.3]$.

Identifying components at other wavelengths may reveal the true nature of these intriguing variable low-L_X sources. Some CVs are expected among our variable sources since there are from 100 to 1000 times more white dwarfs than NSs in a GC [Maccarone and Knigge 2007]. However, since background AGN can produce high X-ray/optical flux ratios, they can act as CVs [Bassa et al. 2005]. From the observational point of view, an alternative approach to identifying X-ray sources could be to simultaneously combine the data taken in different energy bands (X-ray, UV, optical, IR). In particular, JWST IR and/or HST optical observations may help identify the six newly identified X-ray sources in our *Chandra* study.
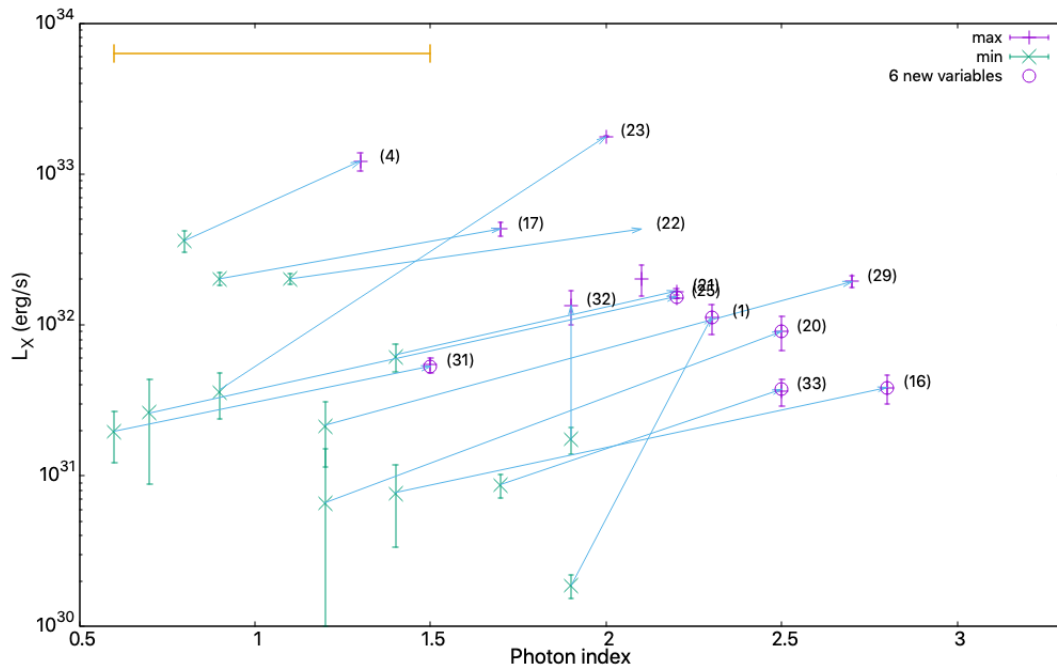
Figure 2.11: Maximum (red +) and minimum (green x) X-ray luminosities vs. photon index, for the 13 detected variable sources in M28. Source ID numbers are shown between parentheses, and the 6 newly discovered variables are marked with red circles. The yellow line on the top left corner represents the average error for the photon index which corresponds to $\Gamma = \pm 0.45$.

((a)) Source 1 (OBS ID:2685).
$L_X = (1.8 \pm 0.8) \times 10^{30}$ erg s^{-1}
$\Gamma = 2.3 \pm 0.6$

((b)) Source 1 (OBS ID:9132).
$L_X = (4.6 \pm 0.5) \times 10^{31}$ erg s^{-1}
$\Gamma = 1.9 \pm 0.1$

((c)) Source 1 (OBS ID:16750).
$L_X = (1.1 \pm 0.2) \times 10^{32}$ erg s^{-1}
$\Gamma = 1.9 \pm 0.2$

((d)) Source 20 (OBS ID:2685).
$L_X = (6.1 \pm 5.0) \times 10^{30}$ erg s^{-1}
$\Gamma = 2.5 \pm 1.1$

((e)) Source 20 (OBS ID:9132).
$L_X = (3.1 \pm 0.5) \times 10^{31}$ erg s^{-1}
$\Gamma = 1.5 \pm 0.3$

((f)) Source 20 (OBS ID:16749).
$L_X = (9.1 \pm 0.2) \times 10^{31}$ erg s^{-1}
$\Gamma = 1.6 \pm 0.4$

((g)) Source 25 (OBS ID:2685).
$L_X = (1.0 \pm 0.3) \times 10^{32}$ erg s^{-1}
$\Gamma = 1.2 \pm 0.2$

((h)) Source 25 (OBS ID:9132).
$L_X = (2.6 \pm 0.3) \times 10^{31}$ erg s^{-1}
$\Gamma = 2.0 \pm 0.1$

((i)) Source 25 (OBS ID:16750).
$L_X = (1.1 \pm 0.2) \times 10^{32}$ erg s^{-1}
$\Gamma = 1.6 \pm 0.2$

((j)) Source 33 (OBS ID:2684).
$L_X = (2.7 \pm 2.0) \times 10^{31}$ erg s^{-1}
$\Gamma = 2.1 \pm 0.7$

((k)) Source 33 (OBS ID:9132).
$L_X = (7.8 \pm 0.2) \times 10^{30}$ erg s^{-1}
$\Gamma = 2.5 \pm 0.2$

((l)) Source 33 (OBS ID:16750).
$L_X = (2.9 \pm 0.8) \times 10^{31}$ erg s^{-1}
$\Gamma = 2.1 \pm 0.3$

Figure 2.12: Newly discovered variable sources in M28. Chandra-ACIS archival observations of six sources in three epochs (from left to right): 2002, 2008, and 2015. Green circles show the sources from Becker et al. (2003).

((a)) Source 16 (OBS ID:2684). $L_X = (7.1\pm) \times 10^{30}$ erg s^{-1} $\Gamma = 2.4 \pm 1.2$

((b)) Source 16 (OBS ID:9132). $L_X = (1.9 \pm 0.4) \times 10^{31}$ erg s^{-1} $\Gamma = 1.6 \pm 0.2$

((c)) Source 16 (OBS ID:16750). $L_X = (3.4 \pm 3.2) \times 10^{30}$ erg s^{-1} $\Gamma = 2.8 \pm 1.2$

((d)) Source 31 (OBS ID:2684). $L_X = (3.9 \pm 0.2) \times 10^{31}$ erg s^{-1} $\Gamma = 1.0 \pm 0.6$

((e)) Source 31 (OBS ID:9132). $L_X = (5.8 \pm 0.1) \times 10^{31}$ erg s^{-1} $\Gamma = 1.1 \pm 0.1$

((f)) Source 31 (OBS ID:16748). $L_X = (1.7 \pm 0.9) \times 10^{31}$ erg s^{-1} $\Gamma = 1.4 \pm 0.7$
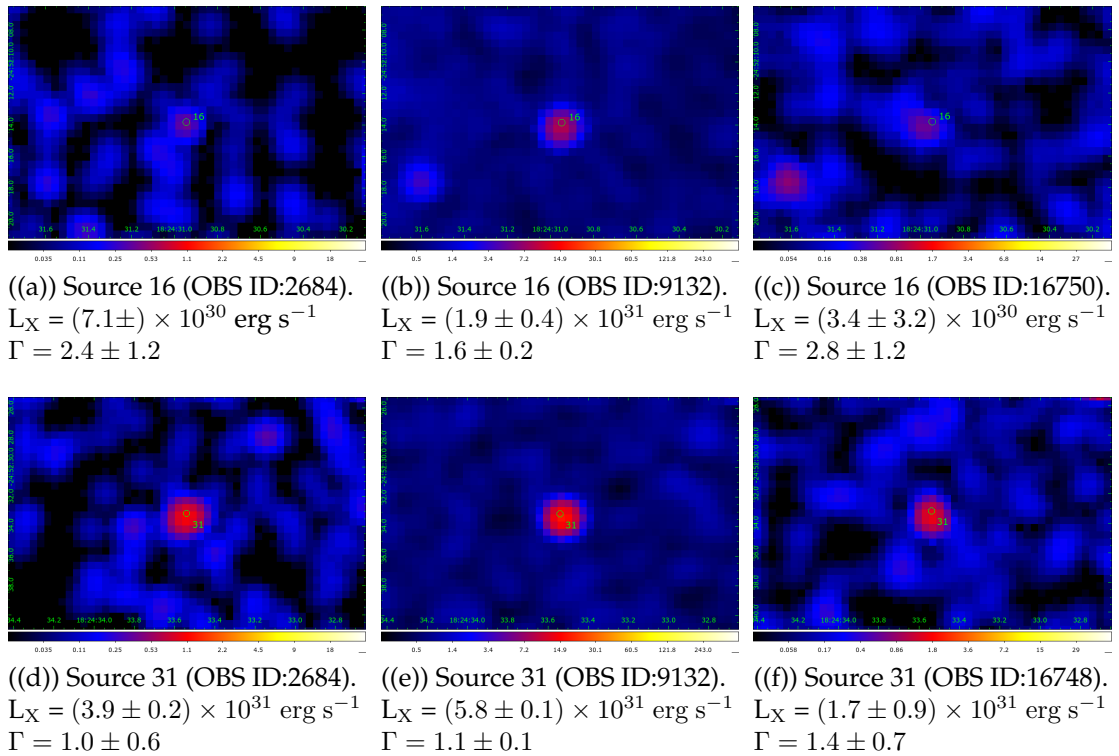
Figure 2.13: (Cont. of Fig. 2.12) Newly discovered variable sources in M28. Chandra-ACIS archival observations of six sources in three epochs (from left to right): 2002, 2008, and 2015. Green circles show the sources from Becker et al. (2003).

Chapter 3

SPMHD Simulations of the Pulsar-Disk Interaction

Numerical simulations have become a powerful tool in fluid mechanics. The large-scale dynamics of astrophysical plasma flows can often be described within a fluidistic approximation known as one-fluid magnetohydrodynamics which makes it accessible to simulations of complex astrophysical scenarios. Among them, pulsar electrodynamics and pulsar-disk interaction are of greatest interest and related to the tMSP enigma. From the theoretical side, the details of the physical mechanisms driving the changes in the state of tMSPs are not yet well understood. Starting with the work by Shvartsman (1970) performed years before the discovery of the first tMSP, several works identified the different modes of interaction between the nearby disk and the NS in low-mass X-ray binaries with analytical, albeit phenomenological, approaches [Shvartsman 1971, Pringle and Rees 1972, Davidson and Ostriker 1973]. According to these works, steady accretion from the disk towards the compact object can only exist in regions where the density of kinetic energy exceeds the magnetic pressure. A comparison of these two energy densities allows us to discern between accreting and non-accreting states of the NS as a function of its polar magnetic strength and orbital parameters, leading to a further classification of these sources as accreting X-ray pulsars, and standard radio pulsars respectively [Lipunov 1992].

Direct numerical simulations of the interaction between the magnetic field of the central star and the accretion disk in compact binary systems were carried out, among others, by Zanni and Ferreira (2009b; 2013) in connection with T-Tauri stars and by Parfrey et al. (2017) in the MSP scenario. These works focused on the study of the torque exerted by the disk onto the central star by the magnetosphere and were carried out in axial symmetry and with a general-relativistic (GR) MHD code

in the last case. An axisymmetric GR-MHD code was also used by Parfrey and Tchekhovskoy (2017) to numerically reproduce, for first time, the different possible accretion regimes in these compact binary sources. It is worth noting that all these studies assumed that the structure of the magnetic field around the NS can be described with the dipole-like geometry characteristic of an aligned magnetic rotator. Promising full three-dimensional MHD simulations of the structure of the wind around the pulsar have been recently developed by Cerutti et al. (2016; 2020b) and by Romanova et al. (2021). As these calculations are free of geometrical constraints they can hold the pulsar radiation emitted by oblique rotators from first principles.

Ekşi and Alpar (2005) investigated the different outcomes of the pulsar-disk interaction in vacuum by comparing the electromagnetic density of energy estimated with the full Deutsch (1955) solution to the density of gravitational energy. The solution obtained by Deutsch 1955 (see also Michel and Li 1999) consists of a suite of analytical expressions giving the time-dependent electric ($\mathbf{E}$) and magnetic ($\mathbf{B}$) fields produced by both aligned and oblique magnetic rotators at any distance from the source of $\mathbf{E}$ and $\mathbf{B}$. To carry out the comparisons Ekşi and Alpar (2005) made useful analytical approximations to the electromagnetic density of energy $\left(\langle E^2 \rangle + \langle B^2 \rangle \right) / (8\pi)$, where the brackets indicate a period averaged magnitude. This way they managed to better understand the different outcomes of the pulsar-disk electromagnetic interaction on purely energetic grounds.

In this part of the thesis, we study the interaction of the magnetic field with the nearby accretion disk in a vacuum by varying the inclination angle using energy arguments, similar to those described in Ekşi and Alpar (2005), but carrying out detailed MHD numerical simulations which incorporate realistic disk structures into the numerical simulations. To perform the simulations we use an axisymmetric SPMHD code (Axis-SPMHD) that was recently developed by García-Senz et al. (2023a). To our knowledge, this is the first time that an SPMHD code has been used to simulate the interaction of an MSP with a surrounding accretion disk. Our study focuses on the interaction of the time-averaged magnetic field of the NS, $\langle B^2 \rangle^{1/2}$, with the disk, which, as we will see, is severely affected by heating due to disk-surface-induced electric currents, especially for oblique rotators. This is perhaps the simplest setting to get insight into the stability and endurance of the disk in the presence of the NS magnetic field. In these simulations, the inner disk radius[1] (R_{in})

---

[1]Here taken as the closest point of the disk from the NS where the radial velocity is still small, $v_r \ll v_{\text{orb}}$

and the inclination angle have been taken as free parameters and conveniently varied so that the ensuing impact on the disk structure is further analyzed.

3.1 Electromagnetic pulsar-disk interaction in vacuum

The effects of the electromagnetic radiation from the pulsar onto the nearby accretion disk is a forefront topic of great complexity. It involves many pieces of physics such as the structure of the time-dependent magnetic $\mathbf{B}(t)$ and electric fields $\mathbf{E}(t)$ radiated by the pulsar and its further interaction with the surrounding plasma. The electromagnetic radiation may interact directly with the accretion disk [Ekşi and Alpar 2005] or the interaction is mediated by a relativistic pulsar wind [Parfrey et al. 2017] or perhaps there is a mix of both mechanisms. Nevertheless, the qualitative behavior of the pulsar-disk interaction and the connection with the tMSP phenomena can be understood with a simple energy model, as shown by Cohn et al. (2013), Papitto et al. (2013), Linares (2014a), Papitto and de Martino (2022a).

Consider first that the energy radiated by the pulsar is that of a magnetized oblique rotator in a vacuum, whose properties have been thoroughly described by Deutsch (1955) and Michel and Li (1999). A glimpse at Figure 3.1 gives an idea of the richness of the $B(t)$ around the spinning NS. The components of $B(t)$ in spherical coordinates fluctuate from pure dipole ($B_\theta \neq 0; B_r = B_\varphi = 0$) for strictly aligned rotators (first column) to an azimuthal, B_φ-dominated radiation for misaligned rotators at large distances. The latter case corresponds to a typical electromagnetic wave (e.m.w.) propagating through the vacuum [Cerutti et al. 2020a]. It is worth noting that the aligned rotator solution is unstable and not very realistic indeed because even a small value of the magnetic axis angle produces a big change in the electromagnetic field around. Still, the constant field B_θ takes over the other oscillating components for $x = r/R_{LC} \leq 1$ and inclination angle, $\xi \leq 20^0$, as shown in the two first rows in Figure 3.1.

The accretion of matter, which is ultimately responsible for the X-ray state of the NS, is only plausible if the electromagnetic pressure remains below the ram pressure of the infalling matter coming from the disk. Figure 3.2 gives the value of these pressures, or energy densities u_x where x is the associated physical magnitude, as a function of the distance to the NS and for different accretion rates and magnetic angles [Papitto and de Martino 2022b]. In particular, the green line in Figure 3.2 shows the approximate electromagnetic density of energy,
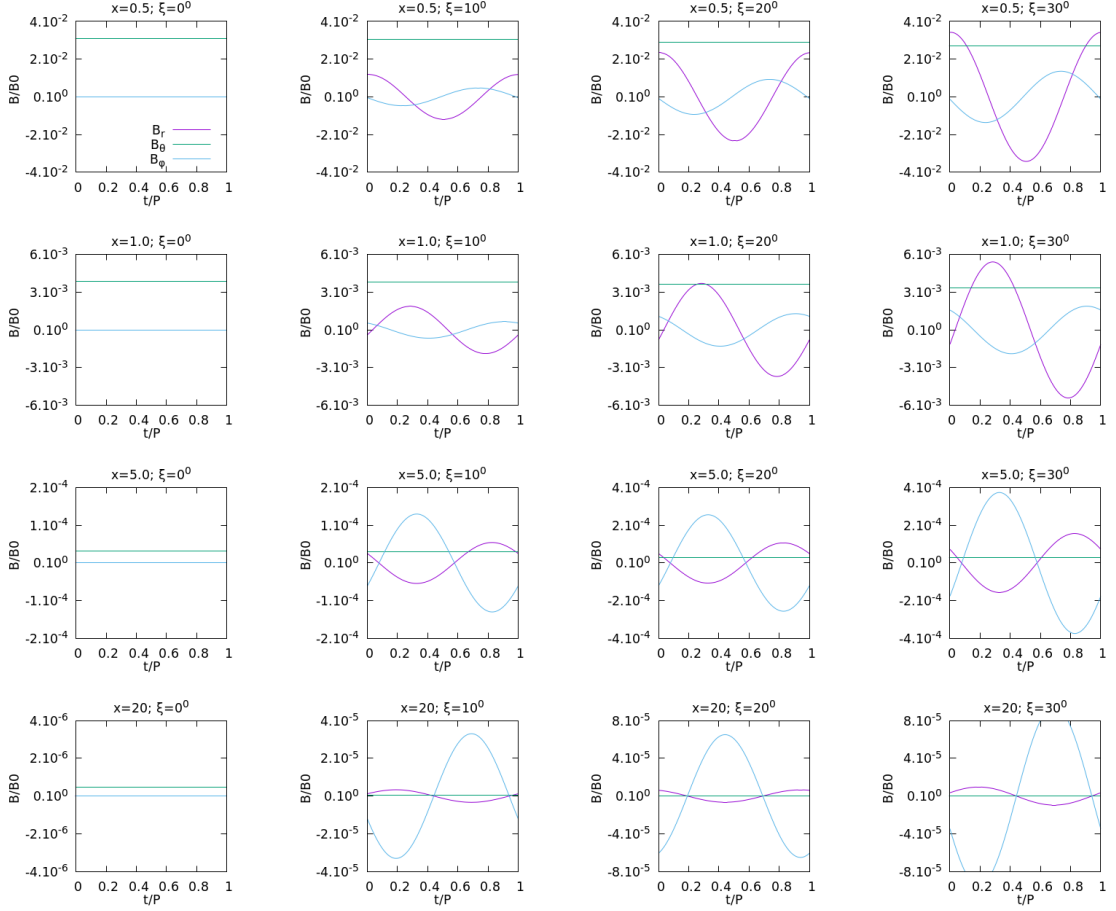
Figure 3.1: Components of the normalized magnetic field (B_0 stands for the magnetic field on the neutron star equator) for tilt angles $\xi = 0^0$ (aligned rotator) and $\xi = 10^0, 20^0, 30^0$ (oblique rotators) as function of normalized time (P is the period of the pulsar) at four normalized distances from the pulsar $x = r/r_{\mathrm{LC}} = 0.5, 1, 5, 20$ respectively.

$$\mathrm{u}_{em} = \begin{cases} \frac{\mu^2}{8\pi r^6}; & \text{dipolar for } r \leq R_{LC}, \\ \frac{\mu^2}{8\pi R_{\mathrm{LC}}^4 r^2}; & \text{e.m.w. for } r > R_{\mathrm{LC}}, \end{cases} \tag{3.1}$$

and the magenta line is that of the gravitational density of energy of the infalling gas,

$$\mathrm{u}_{\mathrm{grav}} = \frac{\sqrt{2GM_{\mathrm{NS}}}\ \dot{M}_{\mathrm{acc}}}{4\pi r^{\frac{5}{2}}}, \tag{3.2}$$

where μ in Eq. 3.1 is the magnetic dipole moment of the NS whereas M_{NS} and $\dot{M}_{\mathrm{acc}}$ in Eq. 3.2 are the NS mass and mass-accretion rate respectively. The intersection of lines defined by Eqs. 3.1 and 3.2 roughly defines the Alfven radius R_{A}, which is
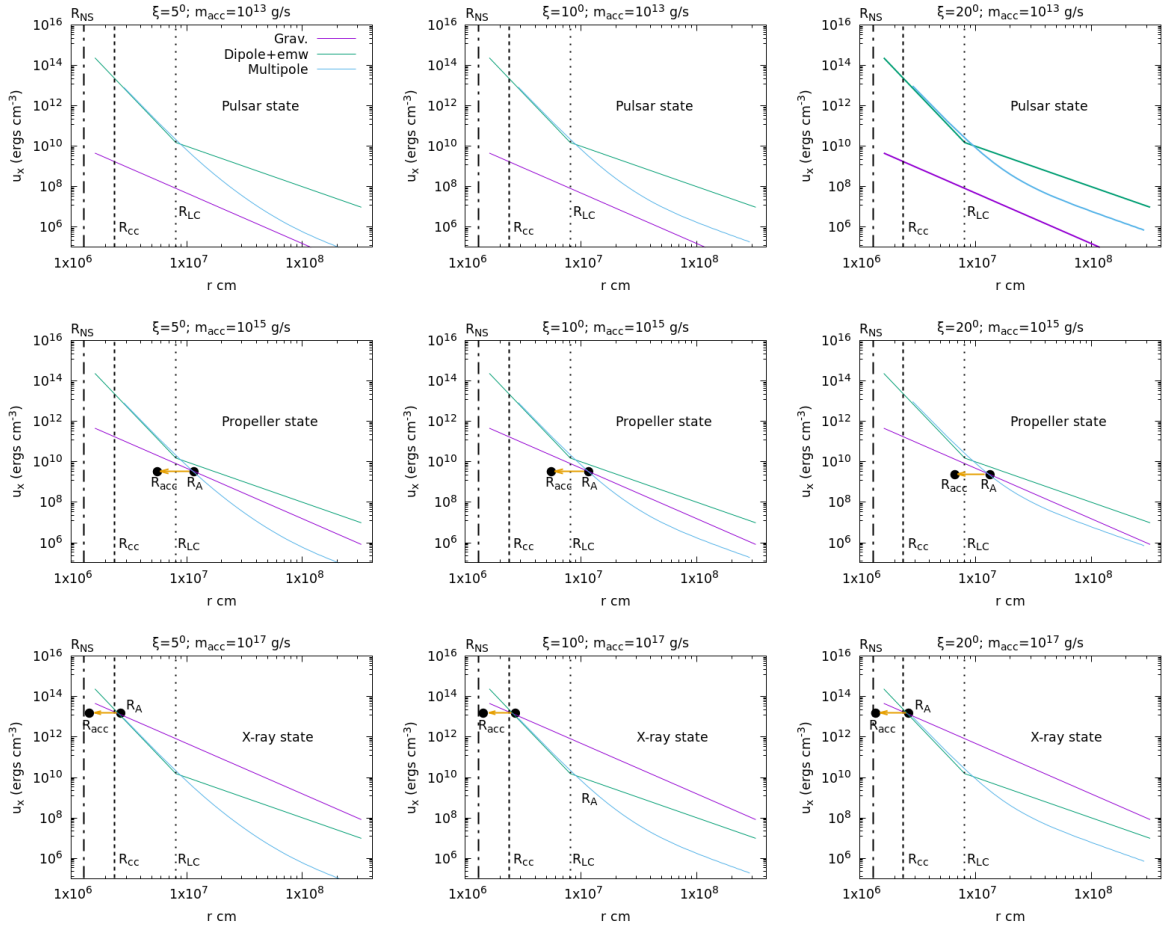
Figure 3.2: Accretion versus magnetic power for different accretion rates and tilt angles as a function of the distance to the neutron star. The head of the yellow arrow points to the accretion radius taken as one-half of the Alfven radius R_A. The vertical lines indicate the neutron star radius, the co-rotation radius, and the light cylinder radius respectively.

bounded to the accretion radius, usually taken as $R_{acc} = \beta R_A$ ($\beta \simeq 0.5$). Depending on the locus of R_{acc} the different states of the tMSP ensue.

According to Figure 3.2 we distinguish the three possible tMSP states: [1] pulsar state (no intersection, first row in Figure 3.2), calculated with the mass-accretion rate, $\dot{M}_{acc} = 10^{13}$ g/s. [2] disk or "propeller" state, with $\dot{M}_{acc} = 10^{15}$ g/s, leading to $R_{co} \leq R_{acc} \leq R_{LC}$, (second row in Figure 3.2) where R_{co} and R_{LC} stand for the co-rotation radius and the light cylinder radius ($R_{LC} = cP/2\pi$, where c is the speed of light and P is the rotational period of the pulsar). For the tMSP PSR J1023+0038, taken as reference in this work, P_s is 1.69 ms, and R_{LC} is 80 km. [3] for larger accretion rates, $\dot{M}_{acc} > 10^{17}$ g/s, (third row in Figure 3.2) accretion of matter is not

blocked and $R_{acc} \leq R_{co}$). In this last case $R_{acc} \simeq R_{NS}$ and the tMSP settles in the outburst or "X-ray" state.

Figure 3.2 also shows that the slope of the full Deutsch solution superpose to the pure dipole for $r \leq R_{LC}$ but diverges from the line defined by Eq. 3.1 for $r > R_{LC}$. Nevertheless, at larger distances, the Deutsch and the e.m.w lines go parallel, especially at magnetic angles $\xi \geq 20^0$. It is worth noting that the slope of the gravitational energy density $u_{grav} \propto r^{-5/2}$ (Eq. 3.2) is that of the free-fall moving material in the accretion column, which differs from the density of energy stored in the rotational velocity field in the disk,[2] $u_{rot} \simeq \rho v_\varphi^2 \propto r^{-23/8}$. The intersection between the electromagnetic energy density and $u_{rot} \propto r^{-23/8}$ better defines the truncation radius of the disk, R_T, which would settle to the right of R_A in Figure 3.2.

In this work we still keep with the energy approach to the pulsar-disk interaction made by Ekşi and Alpar (2005) but we go a step forward by introducing the disk structure in the simulation. This allows us to study the interaction of the multipolar radiation on different regions of the accretion disk in more detail. To make the study numerically tractable we adopt two simplifying hypotheses:

- Following Ekşi and Alpar (2005) the time-dependent magnetic field is replaced by its time-averaged value on a period P so that $\mathbf{B}$ only depends of the spatial coordinates $\mathbf{B}(r) = <B_r^2>^{1/2} \hat{r} + <B_\theta^2>^{1/2} \hat{\theta} + <B_\varphi^2>^{1/2} \hat{\varphi}$, where $(\hat{r}, \hat{\theta}, \hat{\varphi})$ are unit vectors in spherical coordinates and $<B_i^2> (r) = 1/P \int_0^P B_i^2(r)$. This is justified because the period of the pulsar is so small that the disk reacts to the average field of many pulsar rotations.

- We consider that the disk has axial symmetry with respect to the NS axis of rotation. The axisymmetric approach assumes that any magnitude along a particular longitudinal section of the disk and at a distance (r) from the rotation axis has, after being time-averaged, the same behavior as that at the same distance in any other section and can therefore be described with only two variables (r, z) where $r = \sqrt{x^2 + y^2}$. Working in axial geometry boosts the resolution and allows us to simulate a good fraction of the accretion disk investing moderate computational resources.

---

[2]Admitting keplerian rotating velocity $v_\varphi = \sqrt{GM_{NS}/r}$ and a density profile typical of the thin disk approach $\rho \propto \dot{M}_{acc} r^{-15/8}$ [Frank et al. 2002b]

3.2 Disk Initial Models

The axial MHD code relies upon the 3D-SPMHD code by Price (2012b), Price et al. (2018) but restricting it to the axisymmetric (r, z) plane ($r = \sqrt{x^2 + y^2}$) and adding the pertinent non-cartesian contributions (called the hoop-stress terms) to the hydrodynamic Euler equations (see Appendix B for more details). Because of its Lagrangian nature, it is adequate to describe systems with complicated geometries surrounded by large voids and immersed in the pulsar's magnetic field. Assuming axial symmetry allows for a good spatial resolution, which is a crucial requirement to study the evolution of thin accretion disks characterized by a low aspect ratio[3].

In many binary systems undergoing mass transfer the expelled material has sufficient angular momentum to form an accretion disk. This is the case of many millisecond pulsars and more particularly of transitional pulsars oscillating between pulsar and X-ray states. In these cases, the companion star is usually a low-mass main sequence star and accretion takes place by means of the Roche-Lobe overflow mechanism. The structure of the disk around the pulsar can roughly be modeled with the analytical thin disk approximation [Shakura and Sunyaev 1973].

To build the initial models used in this work we first calculate an analytical model of the thin disk following the expressions by Frank et al. (2002b) and with the input parameters summarized in Table 3.1. The data in Table 3.1 correspond to the well-known tMSP PSR J1023+0038 [Archibald et al. 2009b] which is the one considered in this work. We produce a suite of 1D disk models at distances x_{disk} = $R_{\mathrm{in}}/R_{\mathrm{LC}}$ (x_{disk} = 0.5, 1, 5, 25). We then map the 1D distributions into a 2D axisymmetric distribution of SPH particles. The ensuing disks are further relaxed to remove the excess of spurious numerical noise with the procedure described below. Finally, the stability of the disks is checked by running the hydrodynamic code with the magnetic field switched off during a time $\tau \geq P_{\mathrm{in}}$ where P_{in} is the period of the inner disk. The stability is analyzed by monitoring the density and thermal history of several bunches of particles located at different positions along the symmetry axis of the disk. These particles are used later to track the evolution of the disk once the pulsar radiation is turned on.

To relax the disk, we use the technique described in García-Senz et al. (2020). First, the SPH particles are radially distributed according to the density profile

---

[3]A typical ratio between the characteristic thickness, H, and the longitudinal size, ℓ, of the disk in many of our simulations is $\frac{H}{\ell} \simeq 0.03$.
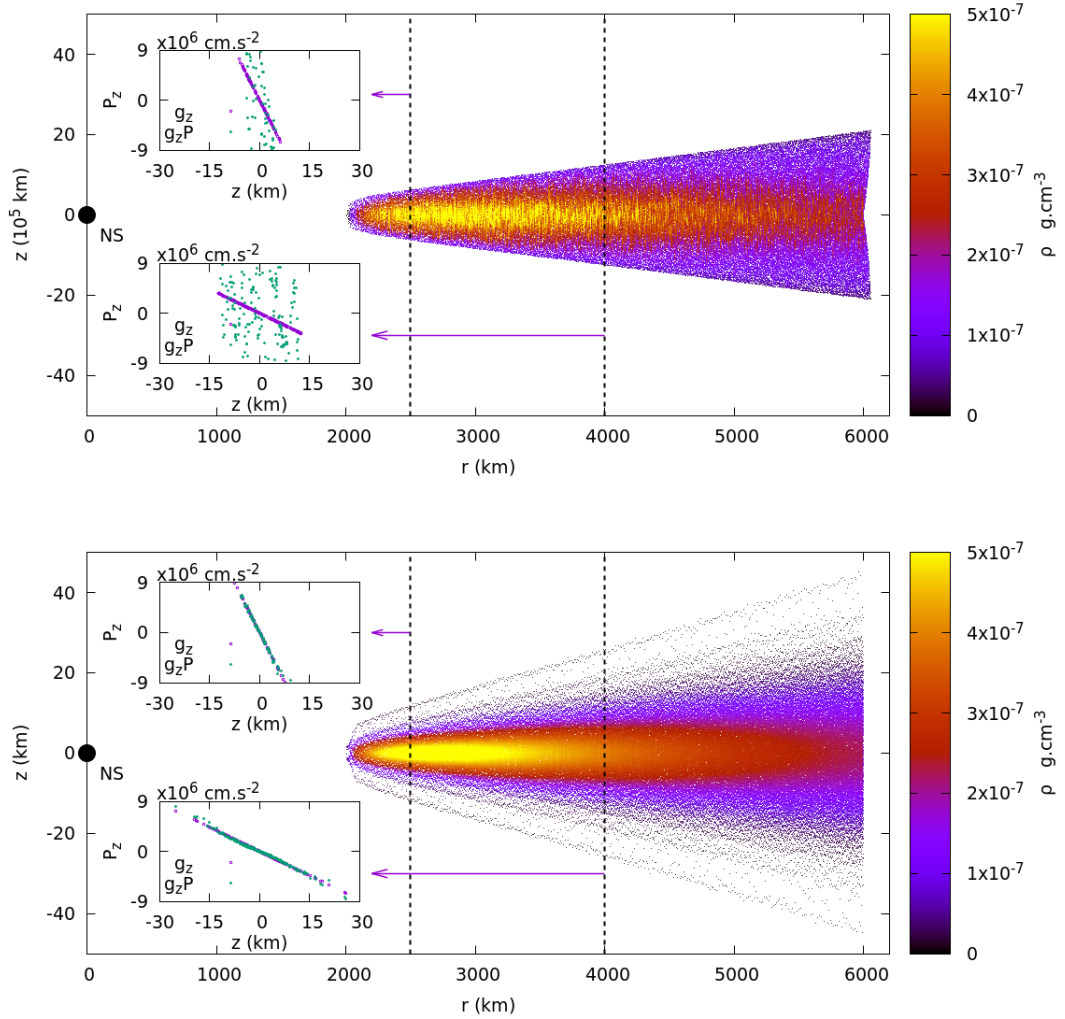
Figure 3.3: Density distribution of the disk with inner radius at $R_{\mathrm{in}} = 2000$ km ($25R_{\mathrm{LC}}$) from the pulsar without the magnetic field. *Upper panel* shows the disk before relaxation. *Lower panel* shows the disk after relaxation. The z-component of gravity and gradient of pressure along the dotted lines at $r = 4000$ km and $r = 2500$ are shown in the sub-figures.

$\rho(r)$, and randomly in the vertical, z-direction, but with a weight so that $\rho(r,z)$ exponentially decays with the altitude at disk coordinate r, as demanded by the thin disk solution. Such rough axisymmetric disk is then relaxed so that the angular velocity of particle a is,

MSP	M_{NS}	M_{comp}	$\dot{M}_{\mathrm{acc}}$	x_{disk}	α_{v}	R_{NS}	B_0	P_{s}	P_{orb}
	$M_\odot$	$M_\odot$	g/s	$R_{\mathrm{in}}/R_{\mathrm{LC}}$	-	km	G	ms	hr
$PSR J1023 + 0038$	1.4	0.2	10^{13}	$0.5, 1, 5, 25$	0.5	15	9.6×10^7	1.69	4.75

Table 3.1: Main parameters of the MSP scenario used to build the accretion disks. Column 6 is the chosen value of the α_{r}-parameter (viscosity) of the turbulent disk. M_{NS} , R_{NS} , M_{comp} , $\dot{M}_{\mathrm{acc}}$, x_{disk} , B_0 , P_{s} , P_{orb} are the mass of the NS, the radius of the NS, the mass of the companion star, mass-accretion rate, inner disk location, magnetic field of NS, spin period of NS and orbital period, respectively.

$$\omega_a = \frac{\omega_c}{\left(1 + \frac{r_a^2}{r_c^2}\right)^m} \tag{3.3}$$

with $m = 3/4$ (Keplerian disk), $r_{\mathrm{c}} = 2 \times 10^6$ cm and ω_{c} is a time-dependent constant determined enforcing the conservation of the total angular momentum, J_{disk}, of the disk at each iteration step [García-Senz et al. 2020]. At each integration step, particles are displaced a distance proportional to the value of the particle acceleration and to its smoothing length h. This procedure ensures that all regions of the disk achieve equilibrium, even those regions of the disk where the characteristic relaxation time is larger. Particle positions (r, z) are then updated with the following prescription,

$$(r, z) = (r_0, z_0) + \eta h \left(\frac{|a_r|}{\sqrt{f_{pr}^2 + f_{gr}^2 + f_c^2}} u_r, \frac{|a_z|}{\sqrt{f_{pz}^2 + f_{gz}^2}} u_z \right) \tag{3.4}$$

where f_p, f_g, f_c symbolize the pressure, gravity and centripetal forces respectively and (u_r, u_z) is the unit vector pointing along the acceleration vector (a_r, a_z). The parameter $\eta = 10^{-4} \times (r/R_{\mathrm{in}})^n$, where R_{in} is the position of the inner disk and $n \simeq 0.6$, controls the amount of displacement so that it is larger in the regions of the disk with $r >> R_{\mathrm{in}}$. In this way, the initial 2D distribution of SPH particles settles in a balanced disk structure which preserves the total mass and total angular momentum obtained with the analytical thin disk approach.

A representative example is shown in Figure 3.3 which depicts the density color map of the disk before (upper panel) and after (lower panel) the relaxation process is applied to the $R_{\mathrm{in}}/R_{\mathrm{LC}} = 25$ configuration. As it can be seen the disk reacts to keep the vertical equilibrium, resulting in a thicker structure fulfilling $g_z = -\frac{1}{\rho}\frac{\partial P}{\partial z}$ everywhere. This is shown in the small sub-figures inside the color map boxes depicting g_z and $P_z = -\frac{1}{\rho}\frac{\partial P}{\partial z}$ along the lines $r = 2500, 4000$ km respectively.

Unlike the initial disk, which is not in vertical equilibrium, the particle distribution after relaxation is fairly well balanced.

3.3 Numerical Simulations

Having obtained stable initial disks (see Figure 3.3), we now examine scenarios without a magnetic field to check the stability of the disk and with magnetic field strength ($B_0 = 9.6 \times 10^7$ G for the pulsar $J1023 + 0038$, Deller et al. 2012) using the initial disk models to understand how the disk reacts to the magnetic field. The plasma resistivity, which controls the amount of magnetic dissipation is taken as $\xi = \alpha_r V_A h$ where $\alpha_r = 1$ (dimensionless resistivity parameter), V_A is the Alfven velocity and h is the smoothing length (see Appendix B). Therefore the scale of the dissipation is artificially expanded to the local resolution of the code which is a common practice indeed. A default value of $\alpha_r = 1$ was chosen in all simulations. The location of the inner radius of the disk is an important parameter determining the outcome of the interaction. Hence, we locate the disk at four different distances we discuss in this chapter. The numerical simulations in this study employ the SPMHD method which discretizes the governing equations of MHD using Lagrangian particles, where each particle represents a volume element of the fluid. A critical aspect of our simulation methodology includes an algorithm designed to identify and remove problematic particles, ensuring numerical stability and accuracy. When a particle is removed, the algorithm reorders the particle indices throughout the simulation domain, which involves updating pointers to particles in various regions of the disk.

Model	Number of Particles	R_{in} km	R_{out} km	R_{in} LC	P_{in} s	P_{out} s
A	2×10^5	2000	6000	25	1.3	6.7
B	4×10^5	400	4000	5	0.16	3.7
C	15×10^5	80	2000	1	0.01	1.3
D	15×10^5	40	2000	0.5	0.004	1.3

Table 3.2: Main parameters characterizing the different pulsar-disk scenarios that we simulate. R_{in} and R_{out} represent the inner and outer disk radii, respectively. P_{in} and P_{out} represent Keplerian periods at inner and outer disks, respectively. LC stands for the light cylinder.

3.3.1 R_{in} at 25LC: The Reference Calculation

Our primary calculations are centered around the position of the inner disk radius, located at $R_{in} = 25R_{LC}$. To explore the stability of the disk, we initially conducted simulations without incorporating a magnetic field. After constructing an initial model of the disk (Section 3.1), we let the particles move freely under the action of gravity and pressure forces and with $B = 0$. We monitored the evolution of the disk during $t = 16$ s which corresponds to 12 Keplerian orbits of the inner disk region and found that the disk is fairly stable (Figure 3.4, 3.5, and Table 3.3).
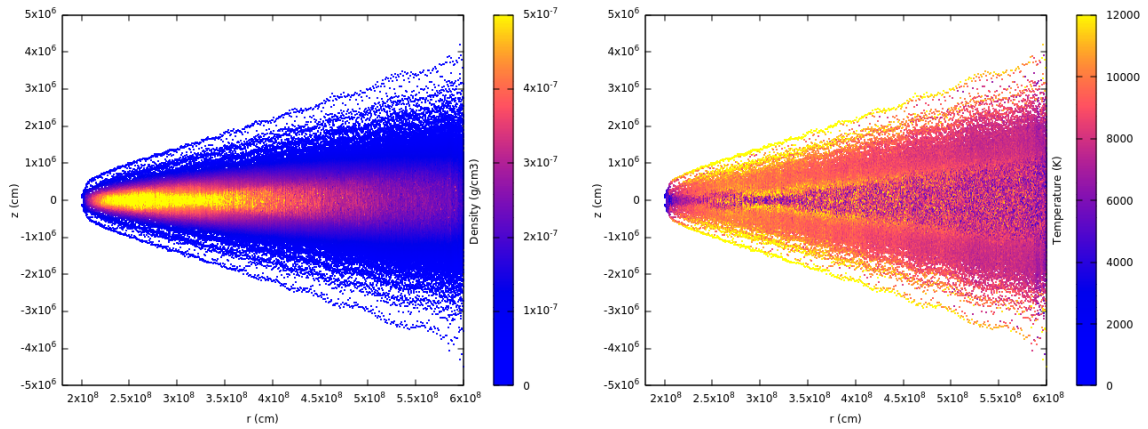
Figure 3.4: Density (left panel) and temperature (right panel) distribution of the disk at 25R_{LC} at t=16 s where the magnetic field has been deactivated from the beginning of the simulation.

3.3.1.1   Aligned Rotator: $B \neq 0$, $\xi =0°$

In this part, we activate the magnetic field strength as $B_0 = 9.6 \times 10^7$ G. In the case of $B \neq 0$, for aligned ($\xi = 0°$) rotators, we manage to simulate the disk evolution during 4.5 seconds, completing 3.5 Keplerian orbits. During that time the disk behaved well without strong signatures of instability, except in a small region around R_{in} (Figure 3.6, Table 3.3). Figure 3.7 demonstrates the evolution of the density and temperature ratios relative to their initial values over the simulation time for three distinct regions within the disk (close, middle, and far). The left panel illustrates the density changes, while the right panel shows the temperature variations. We took three distinct regions within the disk: 2500 km, 4000 km, and 5500 km, each consisting of 5 particles and taking the average.

The observed variations in density and temperature ratios across the different regions of the disk provide insights into the stability of the disk under simu-
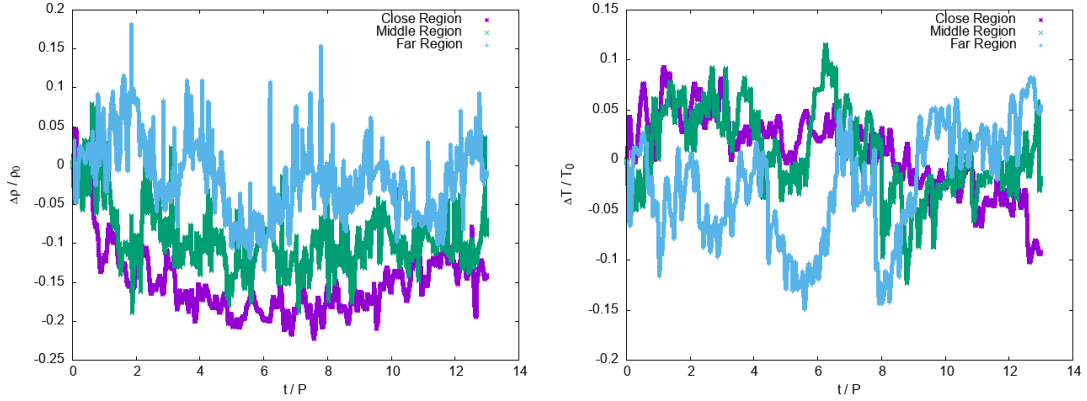
Figure 3.5: The ratio of the temperature/density change to the initial temperature/density for the 25LC case and B=0. Density evolution is shown on the left panel and temperature evolution on the right panel (at t=16 s). The x-axis represents the simulation time normalized by the Keplerian period at the inner edge of the disk (t/P). The three regions, designated as close, middle, and far, are located at 2500 km, 4000 km, and 5500 km within the disk, respectively.

lated conditions. The close region, located at 2500 km, demonstrates substantial instability with pronounced fluctuations in both density and temperature. This suggests that particles in this region are more affected and unstable, potentially due to stronger interactions with the NS's magnetic field. In contrast, the middle (4000 km) and far (5500 km) regions exhibit more stable behavior with relatively minor fluctuations in density and temperature. This indicates that particles in these regions are less affected by the magnetic field during the time covered by the simulation, likely due to weaker magnetic influences as the distance from the NS increases. These findings highlight the complex dynamics of accretion disks around NS, where regions closer to the NS are more prone to become destabilized. This behavior aligns with theoretical expectations, as the intense gravitational and magnetic interactions near the NS can induce significant perturbations in the disk [Frank et al. 2002a]. It is crucial to consider that numerical factors can influence the simulation results, especially around R_{in} because it is difficult for SPH to estimate the gradients accurately, although in any case, it affects a very low amount of mass. Future studies should aim to refine the numerical models and explore the effects of different initial conditions and simulation parameters to obtain more accurate results.
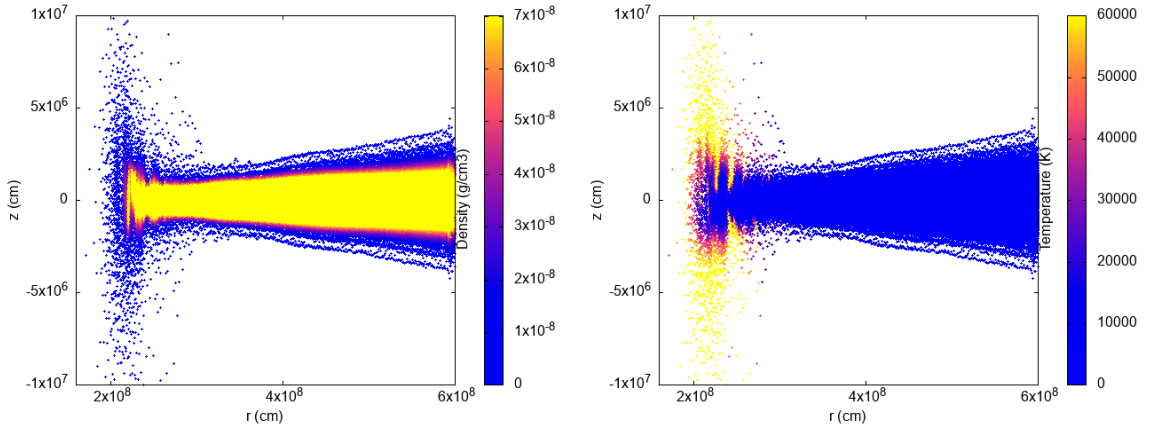
Figure 3.6: Density (left panel) and temperature (right panel) distribution of the disk at $25R_{LC}$ where the magnetic field is activated ($\xi =0°$, t=3.5 s).
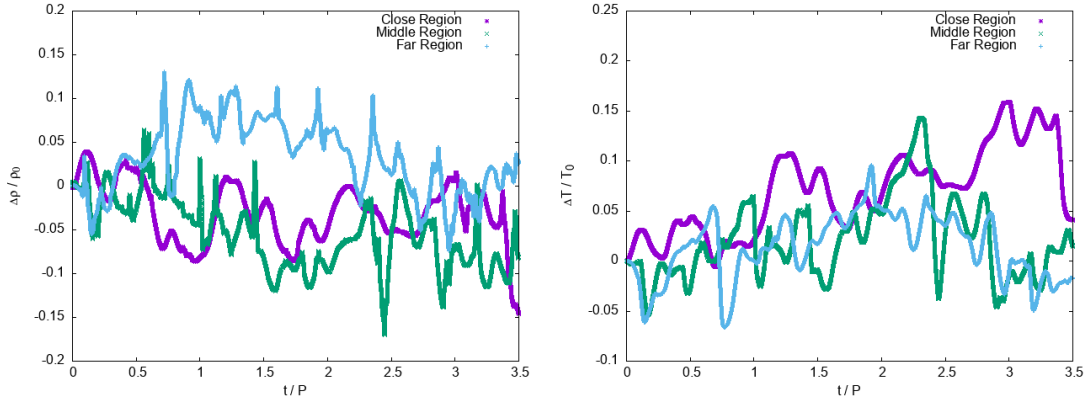
Figure 3.7: The ratio of the temperature/density change to the initial temperature/density. Density evolution is shown on the left panel and temperature evolution on the right panel ($\xi =0°$, 25LC, t=3.5 s). The x-axis represents the simulation time normalized by the Keplerian period at the inner edge of the disk (t/P). The three regions, designated as close, middle, and far, are located at 2500 km, 4000 km, and 5500 km within the disk, respectively.

3.3.1.2 Oblique Rotators: $B \neq 0$, $\xi =$5°, 10°, 20°, 30°

For the simulations with inclination angles $\xi =$5°and $\xi =$10°, the inner disk completes one full Keplerian orbit (Figure 3.8). Since the aim is to track the disk for as much time as we can before numerical reasons impede us from continuing with the simulation, the stability of the disk in these cases is difficult to maintain as the inclination angle increases. For inclination angles of 20°and 30°, the simulations ran for approximately 1.7 and 1.6 s (respectively) before crashing, being able to complete one Keplerian orbit by the inner disk. This occurs because, as the inclination angle increases, more particles are stripped from the disk. As these

Model	ξ	Time	Orbits	Model	ξ	Time	Orbits
		sec				sec	
	0°	3.8	≈3		0°	0.04	3
	5°	2.3	≈2		5°	0.03	2
A	10°	2.3	≈2	C	10°	0.02	2
	20°	1.7	1		20°	0.02	2
	30°	1.6	1		30°	0.02	2
	0°	0.6	≈4		0°	0.02	3.5
	5°	0.4	2.5		5°	0.02	3
B	10°	0.3	2	D	10°	0.02	3
	20°	0.3	2		20°	0.02	3
	30°	0.3	1.5		30°	0.02	3

Table 3.3: Disk dynamics and parameters summary. ξ represents the inclination angle. Time indicates the total simulation duration. Orbits indicate the number of completed Keplerian orbits at the inner disk.

particles move farther from the disk, they become isolated, leading to numerical issues. While removing problematic particles mitigates this, it does not completely resolve the problem. The results from Figures 3.8 and 3.9 indicate that the inclination angle plays a crucial role in the stability of the accretion disk around NS. At lower inclination angles (5°and 10°), the disk structure remains more stable, with less significant changes in density ratios, especially in the middle and far regions at the disk. As the inclination angle increases (20° and 30° , see Appendix B), the disk becomes more unstable, as evidenced by the diffuse density structure and increased density fluctuations.

3.3.1.3   The Role of Induced Surface Currents in Heating Processes

Joule heating and dissipation are important processes in the dynamics of accretion disks, especially in regions close to the NS. The amount of Joule heating generated is directly related to the plasma's resistivity, which governs the conversion of electrical energy into thermal energy. Specifically, the power of Joule heating, P is given by $P = \alpha_r J^2$, where $\alpha_{\rm r}$ is the resistivity and J is the current density. Figure 3.10 shows the physical effect of the heating in the disk for the cases $\xi = 10°$ and $\xi = 30°$. The origin of this effect is the induced plasma current known as Joule heating. Joule heating occurs due to the dissipation of magnetic energy as electric currents interact with the resistive material in the disk [Cairns 2009]. This heating can increase the temperature and pressure within the disk, contributing to the ablation
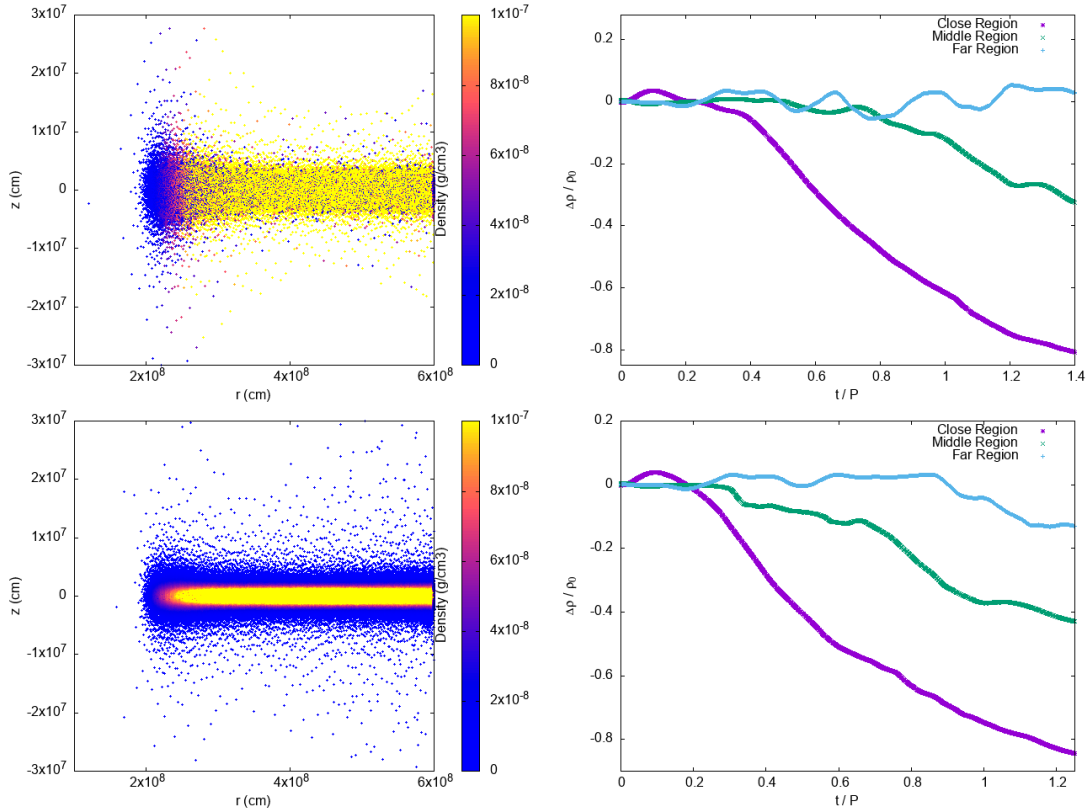
Figure 3.8: Disk structures at 25LC distance (left panels) and the ratios (right panels) of the density change to the initial density for $\xi = 5°$ (upper panel) and $\xi = 10°$ (bottom panel). The x-axis of the right panels represents the simulation time normalized by the Keplerian period at the inner edge of the disk (t/P). The three regions, designated as close, middle, and far, are located at 2500 km, 4000 km, and 5500 km within the disk, respectively.

of disk material and the development of instabilities. The close region's significant instability, as shown in both figures, can be attributed to intense Joule heating due to strong magnetic fields and electric currents near the NS. This heating can lead to increased thermal pressure, causing density fluctuations and ejection of matter. At higher inclination angles, the magnetic field lines can be more twisted and interact more vigorously with the disk material producing stronger electric currents, leading to increased Joule heating and greater dissipation of magnetic energy. This can explain the observed increase in instability for higher inclination angles, as the enhanced heating and dissipation disrupt the disk structure. These findings align with theoretical predictions that magnetic and gravitational interactions, combined with Joule heating and energy dissipation, play crucial roles in the stability of accretion disks [Frank et al. 2002b]. Higher inclination angles exacerbate these interactions, leading to more pronounced instabilities.
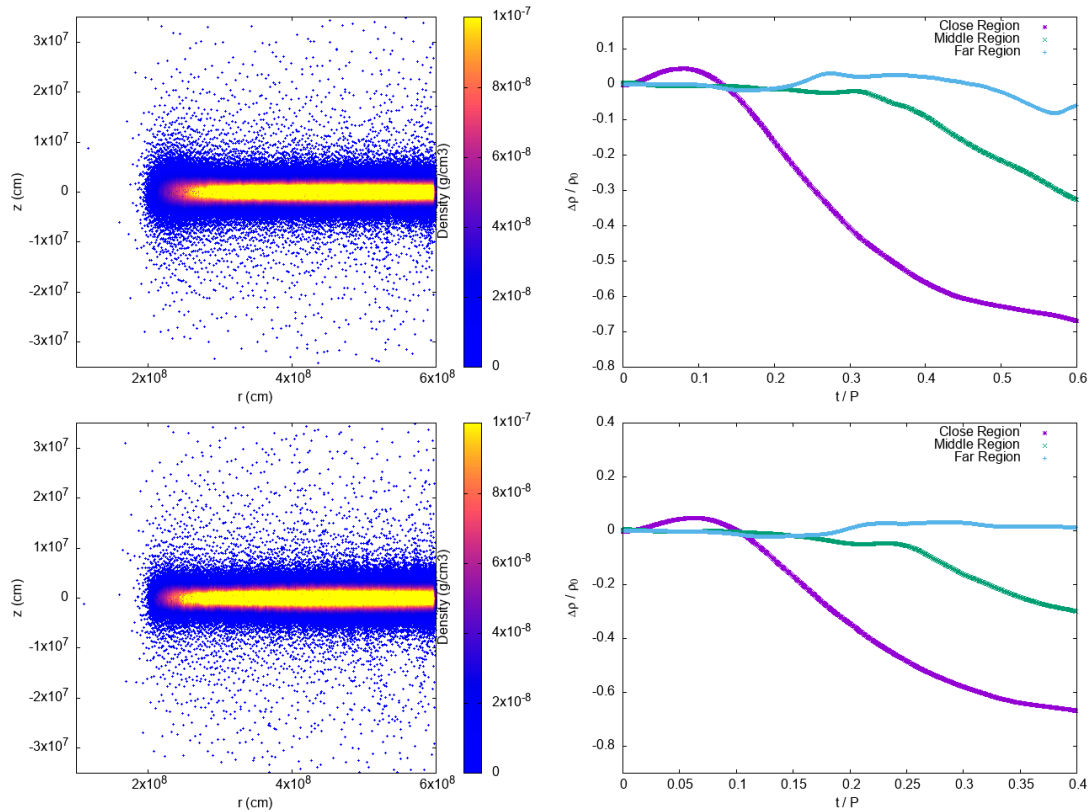
Figure 3.9: Disk structures at 25LC distance (left panels) and the ratios (right panels) of the density change to the initial density for $\xi = 20°$ (upper panel) and $\xi = 30°$ (bottom panel). The x-axis of the right panels represents the simulation time normalized by the Keplerian period at the inner edge of the disk (t/P). The three regions, designated as close, middle, and far, are located at 2500 km, 4000 km, and 5500 km within the disk, respectively.
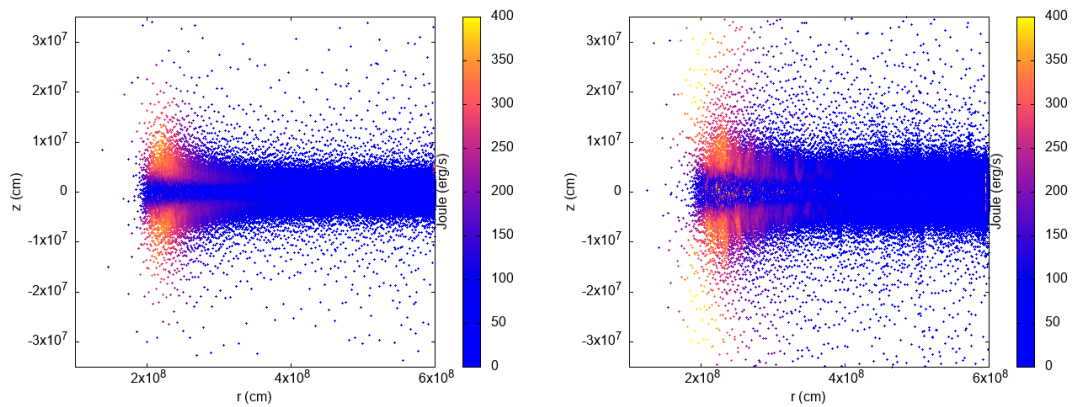
Figure 3.10: Disk structures at 25LC distance showing the Joule heating at t=1.6 s for $\xi = 10°$ (left panel) and $\xi = 30°$, (right panel).

3.3.1.4   Sensitivity of Resistivity parameter α_r

Joule heating is a common phenomenon in plasmas subjected to magnetic field forces, playing a crucial role as a dissipation mechanism in MHD shocks. The amount of Joule heating generated depends on the physical resistivity, which operates on scales that multi-dimensional hydrocodes often cannot resolve. To address this, some numerical formulations incorporate artificial resistivity, scaling the phenomena to the characteristic resolution of the grid or the smoothing length in SPH codes, which is significantly larger than the true physical resistivity. This approach is also effectively used to manage shock waves, typically yielding good results.

In our study, while we primarily maintained the resistivity at α_r=1, we also investigated the impact of varying resistivity parameters on the behavior of the disk by setting the resistivity to values of 0.2 and 5, which is a considerable variation compared to the commonly used value of 1 in the literature. Our findings revealed that with a lower resistivity parameter of $\alpha_\mathrm{r} = 0.2$, the disk showed greater expansion (see Figure 3.11). Lower resistivity values tend to reduce the amount of magnetic energy transformed into heat with the net effect of increasing the magnetic destabilization of the disk. Despite the significant variation in α_r, the qualitative behavior of the disk remains consistent, although notable quantitative differences arise. On the other hand, higher resistivity values tend to increase the dissipation of magnetic energy into heat, potentially leading to more compact disk structures. These results highlight the critical role of resistivity in dictating the physical state and evolution of accretion disks in MHD simulations. Understanding this sensitivity is essential for accurately modeling disk behavior and for interpreting observational data in astrophysical contexts.

3.3.2   Disk behaviors at varying $\mathbf{R}_\mathrm{in}$ Separations

In this section, we examine the behavior of the accretion disk at various distances from the pulsar (R_in = 0.5LC, 1LC, 5LC). We conducted a series of simulations, maintaining a constant magnetic field strength of $B_0 = 9.6 \times 10^7$ G. The simulations were performed with inclination angles of 5°, 10°, 20°, and 30°to assess the impact of these angles on the disk's stability and dynamics.

3.3.2.1   Closest Point to the Pulsar: 0.5LC

This part discusses the investigation of the dynamic behavior of the accretion disk at its closest proximity to the pulsar that we chose. This critical zone is where the
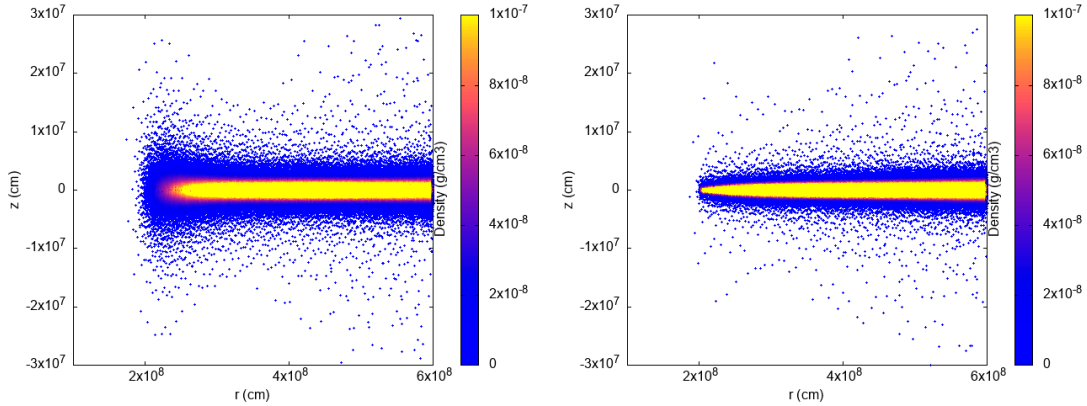
Figure 3.11: An example of the disk structure at 25LC distance with different resistivities for the inclination angle $\xi =10°$, t=1.6 s (left panel: $\alpha_r = 0.2$, right panel: $\alpha_r = 5$).

gravitational and magnetic forces exert their strongest influence on the disk material. Since the location of the inner disk radius is close to the accretion radius, the study by Ekşi and Alpar (2005) suggests that the inner disk radius will be stable beyond the light cylinder. Our simulations focus on the inner disk's stability and response to varying inclination angles under the averaged magnetic field strength. With the magnetic field switched on, we simulated the system during five Keplerian orbits at inclination angles 5°, 10°, 20°. According to Figures 3.12, B.1, and B.2 (see Appendix), all these seem to maintain the stability of the disk except in a very small region around the apex of the disk involving a low amount of mass. Furthermore, a good deal of the ablated mass in that region falls towards the NS and is automatically removed from the simulation when $r < 30$ km. Thus, the accretion flow is not interrupted. The color map of case $\xi = 30°$ (bottom panels in Figure 3.12) shows a more inflated wing of the disk due to the Joule heating. Also, the particles at the apex look more unstable when compared to low-inclination angles. However, the other two more distant regions of the disk do not reveal signs of instability. We therefore conclude that this configuration is stable at not too high inclination angles and the tMSP is well settled in the X-ray emission mode. Indeed R_{in} is close to the accretion radius for which the energy arguments predict stability (see Fig. 3.2 or Fig. 4 in Ekşi and Alpar 2005).

Examining Figure 3.12, we can vividly compare the behavior of the accretion disk at an inclination angle of 30° with that at lower angles. Figure 3.12 illustrates how the disk's structural integrity is maintained at lower inclination angles, completing five Keplerian orbits, whereas at 30°, the disk struggles to sustain itself,
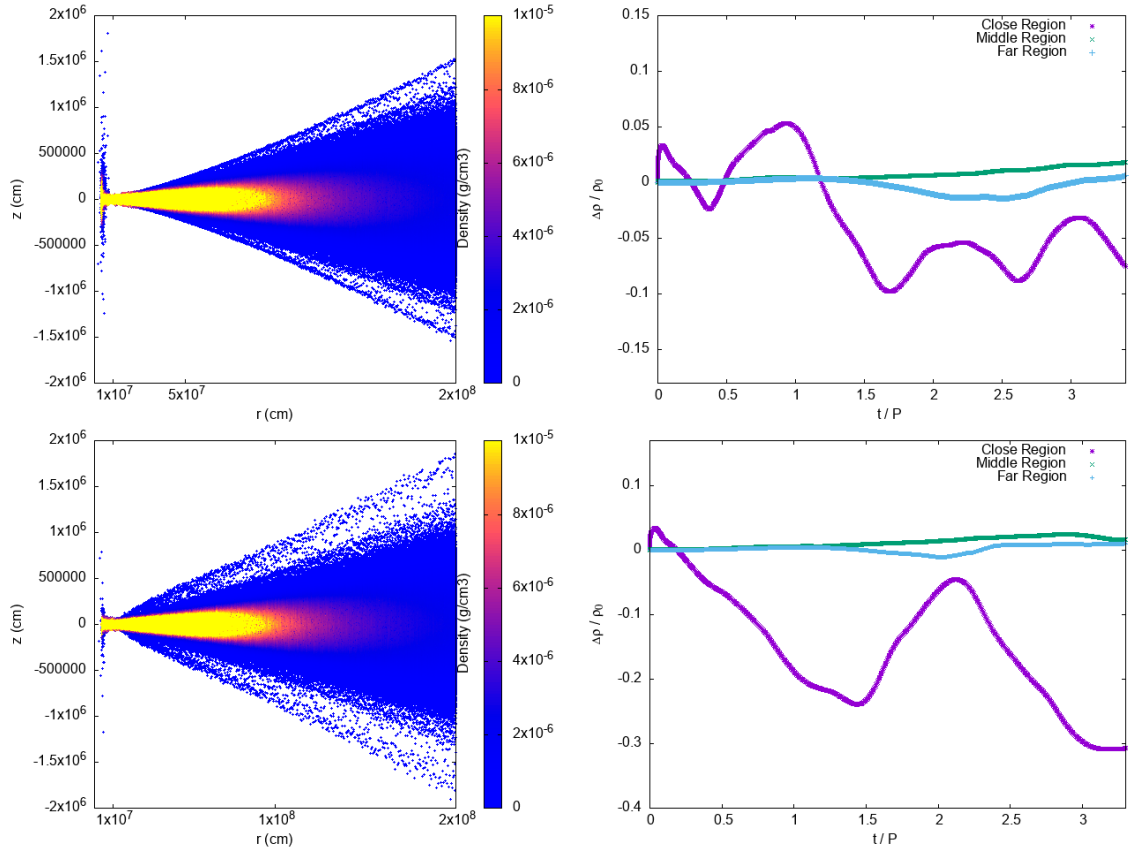
Figure 3.12: *Upper panel* shows the R_{in}=0.5LC simulations performed with $\xi = 0°$ (elapsed time is 0.02 s). *Bottom panel* shows the R_{in}=0.5LC simulations performed with $\xi = 30°$ (elapsed time is 0.01 s). *Left panel:* Disk structure with density distribution. *Right panel:* The ratio of the density changes to the initial density. The x-axis of the right panels represents the simulation time normalized by the Keplerian period at the inner edge of the disk (t/P). The three regions, designated as close, middle, and far, are located at 100 km, 800 km, and 1500 km within the disk, respectively.

completing only 3 orbits before ablated particles caused numerical problems and the calculation stopped. At 30°, although Figure 3.12 shows some expansion at the disk's edges, the induced perturbation is small compared to scenarios with larger R_{in}, and the disk would not be significantly affected. These observations underscore the critical impact of inclination angles on the accretion disk's behavior and highlight the delicate balance required for its stability in the extreme environment near the pulsar.

3.3.2.2 R_{in} at 1LC

This section investigates the orbital characteristics of the disk at a distance of 1LC from the pulsar, focusing on specific inclination angles 0°, 5°, 10°, 20°, and 30°. The results presented in Figure 3.13 show the outcomes of numerical simulations of the disk, focusing on the density distribution and its temporal evolution. The upper panels show the results for an inclination angle $\xi = 0°$, while the bottom panels correspond to $\xi = 30°$. At an inclination angle of 0°, where the NS's spin axis is aligned with the magnetic axis, the inner disk managed to complete 3 Keplerian orbits in the simulations (Figure 3.13). As the inclination angle increases to 5°, the number of Keplerian orbits completed decreases to 2 according to our simulations. Similarly, for 10°, the disk completes approximately 2 Keplerian orbits. Finally, at 20°and 30°inclinations, the disk completes 1 Keplerian orbit before being stopped by numerical reasons (see Appendix B). The observed density fluctuations in the close region (purple curve in Figure 3.13) are more pronounced, indicating stronger heating and dissipation effects near the pulsar. It appears that at low inclination angles, the disk largely maintains its properties. However, at an inclination of approximately 30°, while there is some disruption in the disk structure, it is not severe enough to cause significant changes. This can be attributed to the higher magnetic field strength and stronger gravitational forces closer to the NS, which enhance the magnetic reconnection and dissipative processes as the Joule heating process converts magnetic energy into thermal energy, increasing the temperature and causing density changes [Goodman and Xu 1994].

3.3.2.3   The Inner Disk at 5LC Distance from the Pulsar

Figure 3.14 provides insights into the behavior of accretion disks around neutron stars when the inner edge of the disk is located at 5LC. Similar to Figure 3.13, the upper panels represent simulations performed with an inclination angle $\xi = 0°$, while the bottom panels show results for $\xi = 30°$. The left panels illustrate the disk structure with density distribution, and the right panels show the ratio of the density change to the initial density over time for different regions of the disk. At 0°, the inner disk completes 3.5 Keplerian orbits (Figure 3.14). When we increase the inclination to 5°, the disk completes approximately 2.5 Keplerian orbits. Moving outward to 10°, and 20° at each of these angles, the disk completes approximately 2 Keplerian orbits, and 30° completes approximately 1 Keplerian orbit (Appendix B for more).
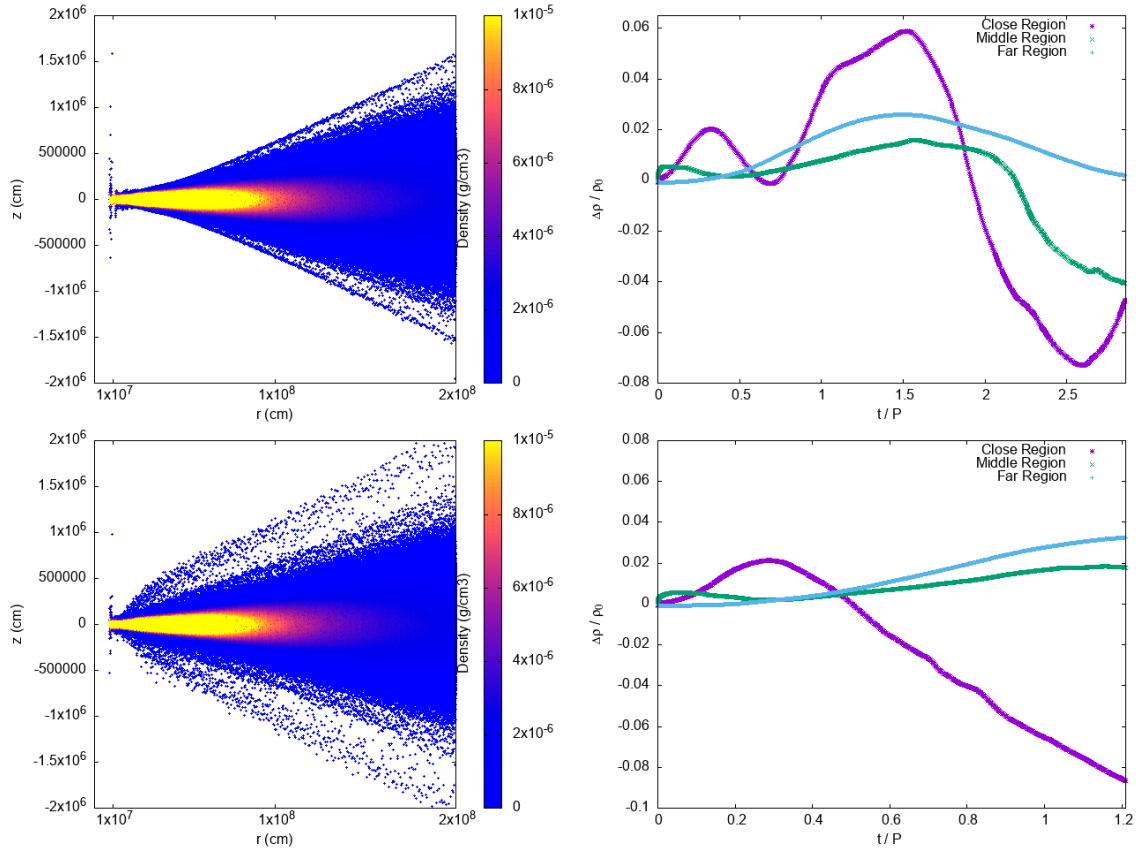
Figure 3.13: *Upper panel* shows the R_{in}=1LC simulations performed with ξ =0°. *Bottom panel* shows the R_{in}=1LC simulations performed with ξ =30°. *Left panel:* Disk structure with density distribution. *Right panel:* The ratio of the density changes to the initial density. The x-axis of the right panels represents the simulation time normalized by the Keplerian period at the inner edge of the disk (t/P). The three regions, designated as close, middle, and far, are located at 200 km, 1000 km, and 1800 km within the disk, respectively.

The left panels of Figure 3.14 depict the density distribution of the accretion disk with the inner edge at five times the light cylinder radius. As in the previous figure, the density is highest near the central plane of the disk and decreases with vertical distance from this plane. The density is more dispersed compared to the simulations with $R_{in} = 1$ LC, reflecting the larger radial extent and potentially weaker gravitational influence at this distance. In the case of ξ =0° (upper right panel), the density exhibits fluctuations, yet its values remain similar to those in the $R_{in} = 1$LC scenario. This suggests that the effects of the magnetic field are not very different when R_{in} is beyond the LC. The fluctuations in the close region (purple curve) show some variability, but overall, the changes are relatively moderate. For ξ =30° (bottom right panel), the density fluctuations are more significant, es-

pecially in the close region but also in the wings of the disk at a larger distance. The purple curve shows a pronounced decrease in density over time, indicating stronger dissipation effects and possibly more active magnetic reconnection processes in this region. The middle and far regions exhibit more stable density ratios, with the far region (blue curve) showing the least variation.

At five times the light cylinder radius, the accretion disk experiences different heating and dissipation dynamics compared to the inner edge at one light cylinder radius. Joule heating, caused by the interaction of magnetic fields and conducting plasma, is more intense at this larger distance, as seen in Figure 3.14.
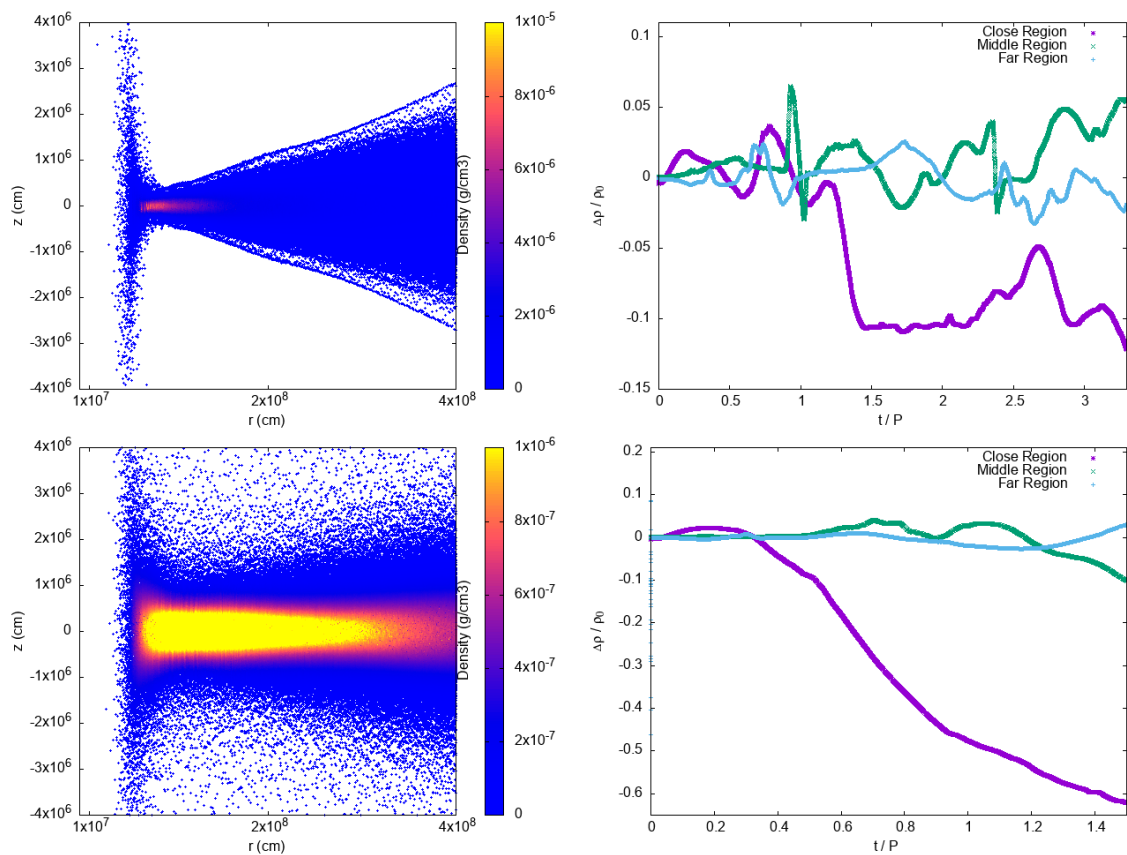
Figure 3.14: *Upper panel* shows the R_{in}=5LC simulations performed with ξ =0°. *Bottom panel* shows the R_{in}=5LC simulations performed with ξ =30°. *Left panel:* Disk structure with density distribution. *Right panel:* The ratio of the density changes to the initial density. The x-axis of the right panels represents the simulation time normalized by the Keplerian period at the inner edge of the disk (t/P). The three regions, designated as close, middle, and far, are located at 1000 km, 2000 km, and 3500 km within the disk, respectively.

Chapter 4

Conclusions

4.1 Comprehensive Study of M28 Through X-ray Data

The study presented in Chapter 2 ("The Neutron Star Population in M28", published in The Astrophysical Journal; Vurgun et al. 2022) focuses on the detailed analysis of NSs within the globular cluster M28. Using extensive data from the Chandra X-ray Observatory combined with radio observations from the Green Bank Telescope, we investigate various characteristics of the cluster's known compact binary MSPs. Our most significant finding is the discovery of a double-peaked X-ray orbital flux modulation during the pulsar state of the transitional MSP M28I. The maximum X-ray luminosity is observed around inferior conjunction of the pulsar. Based on the theoretical models proposed by Wadiasingh et al. (2017), we argue that this double-peaked modulation is indicative of an intrabinary shock structure within M28I. These models suggest that the observed X-ray modulation is caused by a shock front that forms due to the interaction between the pulsar wind and the material from the companion star. The "wrapped" or curved nature of this shock front around the pulsar is consistent with the double-peaked structure in the X-ray light curve. As the system orbits, the line of sight to the shock front changes, causing the observed variations in X-ray flux. This discovery provides valuable insights into the transitional MSPs, particularly the processes that occur during their pulsar state. This finding not only supports the models of Wadiasingh et al. (2017) but also enhances our understanding of the emission processes and the physical conditions within transitional MSP systems.

Another key finding of this work is the precise constraints we have placed on the mass and radius of the NS in the qLMXB in the cluster. By analyzing the X-ray spectra and fitting them with atmospheric models, we have derived robust estimates for the NS radius under different assumptions regarding the composition of

the star's atmosphere. Using the hydrogen atmosphere model, our results suggest that the radius of the NS is between 9.2 and 11.5 km. This model assumes that the NS atmosphere is primarily composed of hydrogen, which affects the emitted X-ray spectrum and thus our radius estimates. In contrast, when applying the helium atmosphere model, we find that the NS radius ranges from 13.0 to 17.5 kilometers. This larger radius estimate arises from the different spectral properties of helium and implies a different interpretation of the X-ray data. Both sets of radius estimates are based on the assumption of a NS mass of 1.4 solar masses, a commonly used reference value in such analyses. These findings are significant because they provide critical insights into the equation of state of NS matter. Our results indicate that the choice of atmospheric model has a substantial impact on the inferred NS radius, highlighting the importance of accurate atmospheric modeling in such studies. These constraints on the NS radius also contribute to the ongoing efforts to discriminate between different theoretical models of the NS interior, thus advancing our understanding of the fundamental properties of dense matter.

Additionally, we have identified six new variable low-luminosity X-ray sources in the globular cluster M28. These discoveries add valuable data to the growing body of knowledge about long-term variability among X-ray sources in globular clusters. These findings support the recycling theory of MSPs as the variability observed in these new X-ray sources may represent different stages or phenomena within this recycling process, such as changes in accretion rates, magnetic field interactions, or transitions between accretion and rotation-powered states. By monitoring these sources over extended periods and using multi-wavelength observations, we can better understand their behavior and the underlying physical mechanisms driving their variability.

4.2 Stability of the Accretion Disks

The second part of the thesis investigates the interaction between a NS and its surrounding accretion disk under the influence of magnetic pressure from the pulsar. The study explores under what conditions the disk remains stable for different values of its inner radius and the inclination angle between the spin and magnetic axes. Our numerical study is, perhaps, the most simple to approach this problem as the NS magnetic field is reduced to its time-constant quadratic average and axisymmetric geometry is adopted from the onset. With these assumptions,

the stability of the disk upon switching on/off the magnetic field is analyzed by monitoring the disk evolution during, at least, one rotational period of the disk's inner radius. In this context, it is hypothesized that the electromagnetic field operates within a vacuum, devoid of any material medium that could interact with it. Additionally, it is assumed that Newtonian dynamics provide a suitable and sufficient approach to describe the system's behavior, implying that relativistic or quantum mechanical effects (such as magnetic field quantization or quantum electrodynamics) are not considered significant for the analysis. The study of the inner accretion disk's orbital characteristics around a NS reveals significant insights into the dynamics influenced by the inclination angle (between the NS's spin axis and its magnetic axis). The simulations performed in this thesis highlight how the inner accretion disk's orbital parameters change with different inclination angles at varying distances from the pulsar. By examining these variations, our findings indicate that the disk, if truncated at 2000 km from the pulsar, remains stable for 5 seconds, completing 4 Keplerian orbits. As the disk location moves closer to the pulsar, we observe a reduction in the simulation duration.

We also find that increasing the inclination angle of the pulsar spin results in a notable decrease in the disk stability. This finding underscores the critical role of the inclination angle in governing the dynamics and stability of the disk surrounding the pulsar. Inclination angles determine the angle at which magnetic field lines intersect the disk and the dominant component (polar or azimuthal) influencing the efficiency of Joule heating processes. A higher inclination angle typically results in more complex magnetic field configurations and potentially higher current densities within the disk. This intensification of magnetic interactions enhances Joule heating, where magnetic energy is converted into thermal energy due to resistive dissipation. Consequently, changes in the inclination angle can lead to variations in the amount of Joule heating experienced by the disk material, impacting its stability and evolutionary trajectory. Observationally, these correlations could manifest in observable properties such as emission spectra and variability, providing crucial insights into the dynamic interplay between magnetic fields and disk dynamics in NS systems. According to Ekşi and Alpar (2005), if the inner radius of the disk extends beyond the pulsar's light cylinder, the disk can withstand radiation pressure. Consequently, pulsar activity initiates, although the disk's presence may disrupt coherent radio band emissions depending on its inclination angle. Our study also supports that the fate of the disk can depend on the inclination angles. This is in agreement with Ekşi and Alpar (2005) results

and provides an independent proof of their results but based on direct numerical simulations.

4.3 Influence of Magnetic and Spin Axis Alignment on MSP Emission States

To connect the two parts studied in this thesis, we explored how the transitional behavior of MSPs between radio and X-ray emissions might be influenced by the inclination angles. In general, these transitions are typically associated with changes in the accretion rate and the magnetic field's interaction with the accretion disk [Linares 2014a]. In our study, we already report that M28I experiences transitions from a rotation-powered state to an accretion-powered state. Figure 2.3 shows that M28I was detected in the disk state in 2008 and 2013. It is also evident from Figure 2.3 that, since the radio observations (57172.16 and 57333.71) coincided with those from *Chandra*, we confirm that the pulsar was conclusively in an active radio pulsar state during the X-ray observations and likely throughout most of 2015. We investigated the disk-pulsar interactions via SPH simulations to explore the reason behind these transitions. We have also demonstrated that the disk structure is significantly altered by the presence of the pulsar's magnetic field, particularly when the inner edge of the disk is far beyond the light cylinder radius. This effect is especially pronounced in oblique rotators (see Figures B.3, and B.5). This raises the question of how the inner disk radius and the inclination angle can affect the survival and evolution of the accretion disk. The connection between these studies can be elucidated by considering the impact of the inclination angle on the transitional behavior of tMSPs, although transitions between states might also be influenced by changes in the accretion rate. When the NS is in the radio state, the alignment of the magnetic axis can make the radio pulses more visible, particularly if the magnetic poles sweep across our line of sight. Hence, different inclination angles can affect the efficiency and rate of accretion, thereby influencing the likelihood of state transitions. It can also be inferred that most redbacks, which remain in the pulsar state, may have high inclination angles. The exerted torque between the disk and the pulsar appears insufficient to induce significant changes in the magnetic axis over short timescales, but this point requires further investigation. In those systems with relatively low magnetic inclination, state transitions might be triggered by large excursions of the inner disk radius outside the light cylin-

der. However, an efficient physical mechanism driving these changes has yet to be identified.

Appendix A

Details of the X-ray and radio analysis

In this appendix, we present the radio and X-ray positions of the known pulsars, together with their uncertainties and angular separations between the X-ray and radio positions (see Table A.1). We include the individual X-ray spectral fits for the pulsars in M28 (Figures A.2, A.3 and A.4). We also present the measurements and upper limits on the X-ray luminosity of the faint sources in M28 (Figure A.5). Finally, we show the molecular contamination effect on the long-term count rate light curve of the qLMXB (Figure A.6).

Table A.1: Radio and X-ray positions of the pulsars in M28 and their positional uncertainty

Source	RA_{Radio}	DEC_{Radio}	$RA_{\mathrm{X-ray}}$	$DEC_{\mathrm{X-ray}}$	P_{err}^{*}	$\theta^{\dagger}$
	J2000	J2000	J2000	J2000	arcsec	arcsec
A	18 24 32.00799483(72)	-24 52 10.8348902(28)	18 24 32.10	-24 52 10.81	0.3	0.03
B	18 24 32.54585781(35)	-24 52 04.3560436(06)	-	-	-	-
C	18 24 32.19250199(14)	-24 52 14.6818430(26)	18 24 32.20	-24 52 14.80	0.1	0.1
D	18 24 32.42200854(39)	-24 52 26.2224825(13)	18 24 32.43	-24 52 26.90	0.1	0.6
E	18 24 33.08952070(88)	-24 52 13.4701099(81)	18 24 33.05	-24 52 13.30	0.1	0.6
F	18 24 31.81278784(22)	-24 49 24.9511809(85)	18 24 31.80	-24 49 24.89	0.4	0.2
G	18 24 33.02548892(97)	-24 52 17.1927818(36)	18 24 33.03	-24 52 17.00	0.1	0.2
H	18 24 31.61052125(72)	-24 52 17.2268378(32)	18 24 31.61	-24 52 17.35	0.3	0.1
I	18 24 32.50368185(81)	-24 52 07.4353327(34)	18 24 32.51	-24 52 07.66	0.3	0.3
J	18 24 32.73414004(26)	-24 52 10.3208653(08)	18 24 32.71	-24 52 10.18	0.3	0.4
K	18 24 32.49746490(59)	-24 52 11.3661979(78)	18 24 32.49	-24 52 11.31	0.3	0.1
L	18 24 32.35856942(90)	-24 52 08.1973300(70)	18 24 32.34	-24 52 08.02	0.3	0.3
M	18 24 33.1835(5)	-24 52 08.179(23)	18 24 33.21	-24 52 08.20	0.1	0.3
N	18 24 33.1418(12)	-24 52 11.89(3)	-	-	-	-

* Positional uncertainty radius. † Angular separation between the X-ray and radio positions. Units of right ascension are hours, minutes, and seconds, and units of declination are degrees, arcminutes, and arcseconds. M and N's radio positions are taken from Douglas et al. (2022). X-ray positions of I, L and their positional uncertainties (68% c. l.) are taken from Becker et al. (2003). X-ray positions of C, D, E, G, M and their positional uncertainties (68% c. l.) are taken from Cheng et al. (2020). The rest of the X-ray positions and their positional errors are obtained in this work (95% c. l.).

2 Pulses of Best Profile

Search Information

Candidate: PSR_1824−2452I
Telescope: GBT
Epoch$_{topo}$ = 57172.16164352236
Epoch$_{bary}$ = N/A
T$_{sample}$ = 4.096e−05
Data Folded   = 637578240
Data Avg   = 2645
Data StdDev   = 26.58
Profile Bins   = 64
Profile Avg   = 2.635e+10
Profile StdDev   = 8.39e+04

RA$_{J2000}$ = 18:24:32.8800   DEC$_{J2000}$ = −24:52:12.3600
Folding Parameters
DOF$_{eff}$ = 48.66 χ^2_{red} = 3.030 P(Noise) < 7.06e−12 (6.8σ)
Dispersion Measure (DM; pc/cm^3) = 118.870
P$_{topo}$ (ms) = 3.931821487(32)   P$_{bary}$ (ms) = N/A
P'$_{topo}$ (s/s) = 0.0(9.4)x10^{-15} P'$_{bary}$ (s/s) = N/A
P''$_{topo}$ (s/s^2) = 0.0(2.3)x10^{-18} P''$_{bary}$ (s/s^2) = N/A
Binary Parameters
P$_{orb}$ (s) = N/A   e = N/A
a$_1$sin(i)/c (s) = N/A ω (rad) = N/A
T$_{peri}$ = N/A

guppi_57172_M28_0006_subs_0001.fits

sransom 2−May−2022 16:15

Figure A.1: Green Bank Telescope plus GUPPI detection of M28I on 57172, during one of the ∼8-hr duration observations of M28, simultaneous with *Chandra* x-ray observations. The pulsar can be clearly seen to be coming out of the eclipse in the pulse phase vs the time greyscale plot on the left. The integrated pulse profile is shown at the top left. The detection was made using `prepfold` from the `PRESTO` package, after optimizing the predicted orbital phasing using `SPIDER_TWISTER`.
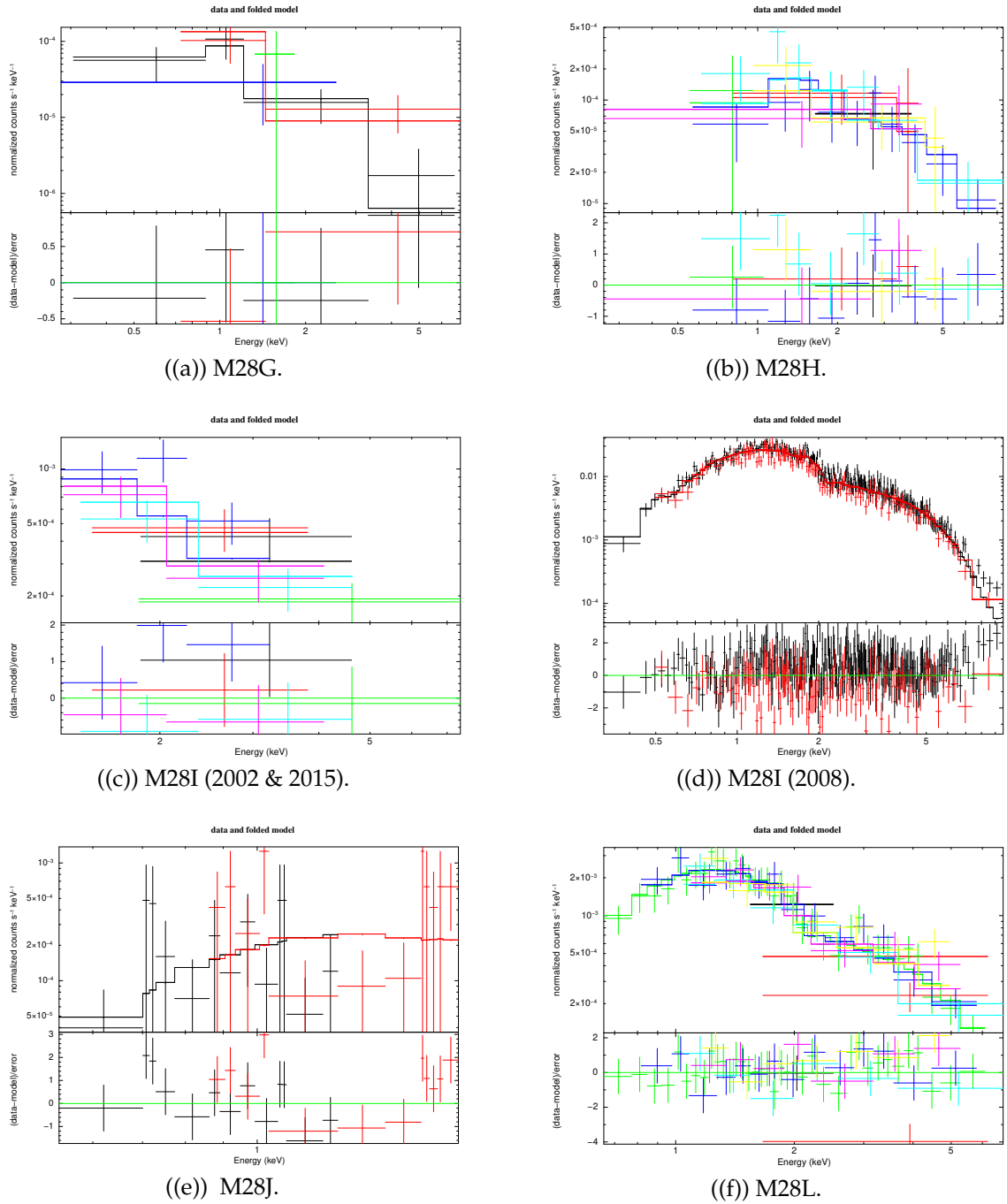
Figure A.2: *Upper panels:* X-ray spectra of the spiders in M28. *Lower panels:* The best fit residuals.
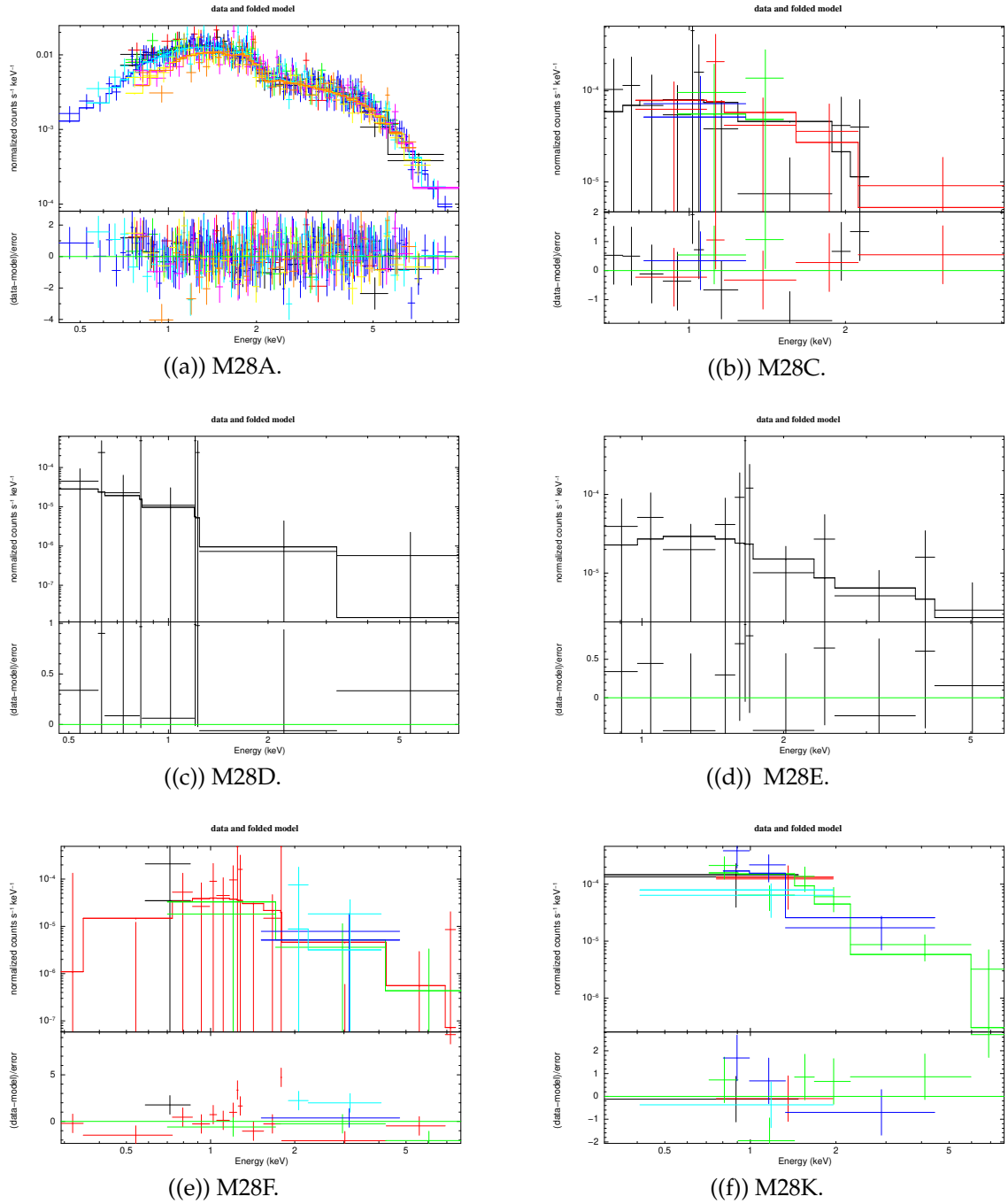
Figure A.3: *Upper panels:* X-ray spectra of the rest of the detected pulsars in M28. *Lower panels:* The best fit residuals.
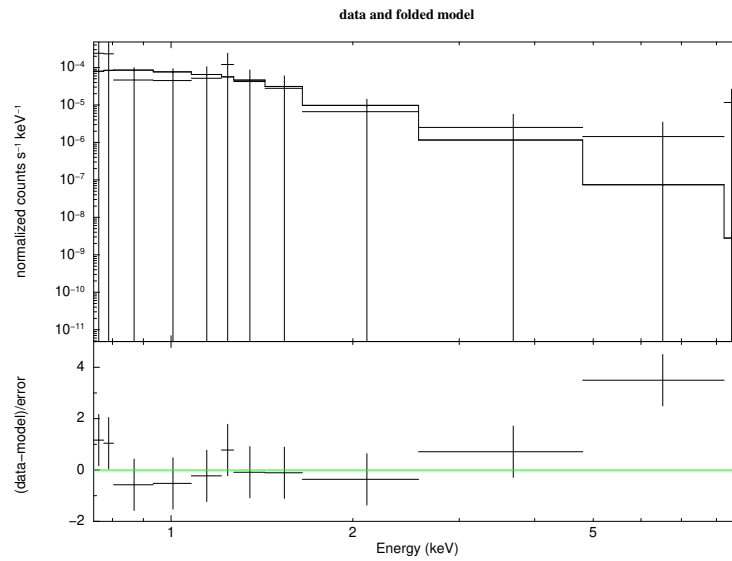
((a)) M28M.

Figure A.4: *Upper panel:* X-ray spectrum. *Lower panel:* The best fit residuals.
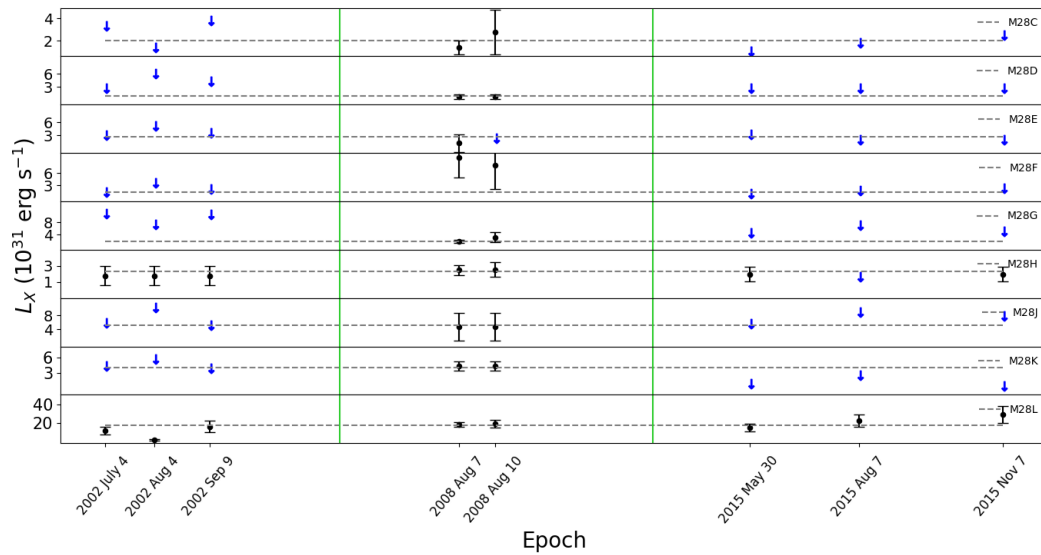
Figure A.5: Luminosity evolution for the faint pulsars. Blue arrows show upper limits, black filled circles indicate detections. Horizontal dashed lines indicate the average luminosity for individual sources. The green vertical lines separate the epochs visually.
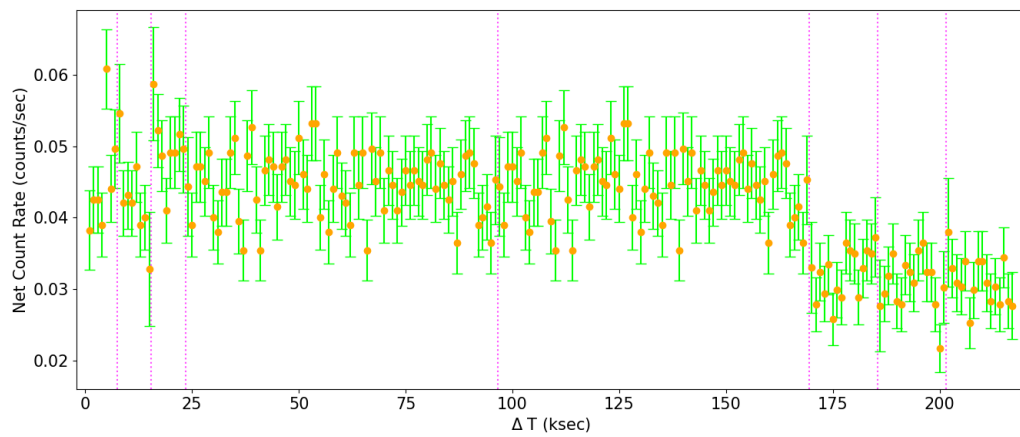
Figure A.6: X-ray count rate light curve (0.2–10.0 keV) of the qLMXB in M28, including all 8 *Chandra*-ACIS observations (separated by vertical lines, with arbitrary time offsets for display purposes). The molecular contamination effect is apparent as a drop in count rate around ΔT∼170 ksec.

Appendix B

Details of Axisymmetric SPMHD simulations

B.1 The MHD equations

Magnetohydrodynamics is a reasonable theoretical framework to describe the macroscopic dynamics of plasmas, i.e. on typical lengthscales much larger than their collisional mean free paths and on timescales much longer than their collisional frequencies. The fundamental equations governing MHD can be expressed as follows:

$$\frac{\partial \rho}{\partial t} + \nabla \cdot (\rho \mathbf{v}) = 0 \tag{B.1}$$

$$\rho \left(\frac{\partial \mathbf{v}}{\partial t} + (\mathbf{v} \cdot \nabla)\mathbf{v} \right) = -\nabla p + \rho \mathbf{g} + \frac{1}{\mu_0}(\nabla \times \mathbf{B}) \times \mathbf{B} \tag{B.2}$$

$$\frac{\partial \mathbf{B}}{\partial t} = \nabla \times (\mathbf{v} \times \mathbf{B}) \tag{B.3}$$

$$\frac{\partial e}{\partial t} + \nabla \cdot [(e + p)\mathbf{v}] = -\rho \mathbf{v} \cdot \mathbf{g} + \mathbf{J} \cdot \mathbf{E} \tag{B.4}$$

$$\mathbf{J} = \frac{1}{\mu_0}(\nabla \times \mathbf{B}) \tag{B.5}$$

Here, ρ denotes the mass density, $\mathbf{v}$ is the velocity vector, p represents the pressure, $\mathbf{B}$ is the magnetic field, μ_0 is the permeability of free space, $\mathbf{J}$ is the current density, $\mathbf{E}$ is the electric field, $\mathbf{g}$ is the gravitational acceleration vector, and e denotes the total energy density.

Equation (B.1) represents the conservation of mass, Equation (B.2) is the momentum conservation equation, Equation (B.3) is Faraday's law of electromagnetic induction, Equation (B.4) is the energy conservation equation, and Equation (B.5) relates the current density to the magnetic field.

B.2 MHD Equations in Axial Geometry and SPH Form

For completeness, we summarize below the main axial SPMHD equations used in this work:

- *Mass conservation*

$$\eta_a = \sum_{b=1}^{n_b} \varepsilon_b \, m_b W_{ab}(h_a) \tag{B.6}$$

- *Momentum equations*

$$a_a^r = 2\pi \frac{\left(P_a + \frac{B_a^2}{2\mu_0} - \frac{(B_a^\varphi)^2}{\mu_0}\right)}{\eta_a} + \\ 2\pi \sum_{b=1}^{n_b} m_b \left(\frac{S_a^{ri}|r_a|}{\eta_a \eta_b} \mathcal{A}_{ab}^i(h_a) + \varepsilon_b \frac{S_b^{ri}|r_b|}{\eta_a \eta_b} \mathcal{A}_{ab}^i(h_b) \right) , \tag{B.7}$$

$$a_a^z = 2\pi \sum_{b=1}^{n_b} m_b \left(\frac{S_a^{zi}|r_a|}{\eta_a \eta_b} \mathcal{A}_{ab}^i(h_a) + \varepsilon_b \frac{S_b^{zi}|r_b|}{\eta_a \eta_b} \mathcal{A}_{ab}^i(h_b) \right) , \tag{B.8}$$

$$a_a^\varphi = 2\pi \left(\frac{B_a^r B_a^\varphi}{\mu_0 \eta_a} \right) + \\ 2\pi \sum_{b=1}^{n_b} m_b \left(\frac{S_a^{\varphi i}|r_a|}{\eta_a \eta_b} \mathcal{A}_{ab}^i(h_a) + \varepsilon_b \frac{S_b^{\varphi i}|r_b|}{\eta_a \eta_b} \mathcal{A}_{ab}^i(h_b) \right) , \tag{B.9}$$

where h_a, h_b are the smoothing lengths of particles a, b respectively (i.e. the local resolution) and repeated indexes in $\{i = r, z\}$ are summed.

- *Energy equation*

$$\frac{du_a}{dt} = -2\pi \frac{P_a}{\eta_a} v_{r_a} + 2\pi \frac{P_a|r_a|}{\eta_a} \sum_{b=1}^{n_b} \frac{m_b}{\eta_b} \left(v_{ab}^i \, \mathcal{A}_{ab}^i(h_a) \right) . \tag{B.10}$$

where S_a^{ij} are the components of the stress tensor of particle a,

$$S_a^{ij} = -\left(P_a + \frac{1}{2\mu_0} B_a^2 \right) \delta^{ij} + \frac{1}{\mu_0} \left(B_a^i B_a^j \right) , \tag{B.11}$$

The magnitude $\mathcal{A}_{ab}^i$ is related to the gradient of the interpolator kernel [García-Senz et al. 2023b], η_a is the 2D-cartesian density (i.e. the surface density) and the remaining symbols have their usual meaning. The parameter ε_b is one for all particles except for ghost particles located across the symmetry axis for which $\varepsilon_b = -1$. The MHD equations above are complemented with the induction equation plus fluid and magnetic dissipative terms in axisymmetric geometry and an efficient divergence-cleaning algorithm [Tricco et al. 2016, Tricco 2023]. The equation of state, EOS, has contributions from the ideal gas of ions and electrons and from radiation. At each integration step, the temperature is obtained from the internal energy by means of a standard Newton-Raphson scheme.

Magnetic Dissipation and Joule Heating

The magnetic dissipation term, $\xi_r \nabla^2 \mathbf{B}$, where ξ_r is the electrical resistivity, leads to the generation of heat due to the resistive dissipation of magnetic energy, similar to the Joule effect in classical electrodynamics. The heating term can be expressed as:

$$Q_{\text{Joule}} = \xi_r \left(\frac{\nabla \times \mathbf{B}}{\mu_0} \right)^2$$

This term represents the rate at which magnetic energy is converted into thermal energy, contributing to the overall heating of the plasma. These equations provide a comprehensive framework for simulating the complex dynamics of magnetized plasmas in axial geometries using the SPH method, capturing both fluid and magnetic field behaviors along with the associated dissipation processes.

In this work, however, we use an expression for the dissipation, $(du/dt)^{\text{diss}}$ which is equivalent to Q_{Joule} above but more compatible with the conservation of energy in presence of shocks Wissing and Shen (2020), García-Senz et al. (2022). The magnetic dissipation which contributes to the rate of change of internal energy writes,

$$\left(\frac{du}{dt} \right)_a^{diss} = -\frac{\pi r_a}{\mu_0 \eta_a} \sum_{b=1}^{n_b} \frac{m_b}{\eta_b} \frac{\xi_{r,a} + \xi_{r,b}}{|s_{ab}|} \mathbf{B}_{ab}^2 \left(\hat{s}_{ab}^i \tilde{\mathcal{A}}_{ab}^i \right) , \quad (B.12)$$

In the tests below, the adopted value of the resistivity ξ_r is,

$$\xi_r = \frac{1}{2} \alpha_r \, v_{sig,B} |s_{ab}| . \quad (B.13)$$

where s_{ab} is the distance between neighbor particles a and b and $\alpha_r = 1$. For the signal velocity, we simply take the Alfven velocity,

$$v_A = \sqrt{\frac{B^2}{\mu_0 \rho}}, \tag{B.14}$$

B.3 The Inner Disk Configurations

In our study, disk configurations are characterized by the location of the disk, which is positioned at varying distances from the NS, specifically at 0.5LC, 1LC, 5LC, and 25LC. We show the disk structures, after interacting with the averaged magnetic field, at different distances in this Appendix section. We also present the ratios of temperature and density changes relative to their initial values within different regions at the accretion disk for all our models.

((a)) R_{in}=25LC, ξ =5°, t=1.4 s

((b)) R_{in}=5LC, ξ =5°, t=0.4 s

((c)) R_{in}=1LC, ξ =5°, t=0.02 s

((d)) R_{in}=0.5LC, ξ =5°, t=0.02 s

((e)) R_{in}=25LC, ξ =10°, t=1.2 s

((f)) R_{in}=5LC, ξ =10°, t=0.3 s

((g)) R_{in}=1LC, ξ =10°, t=0.02 s

((h)) R_{in}=0.5LC, ξ =10°, t=0.02 s
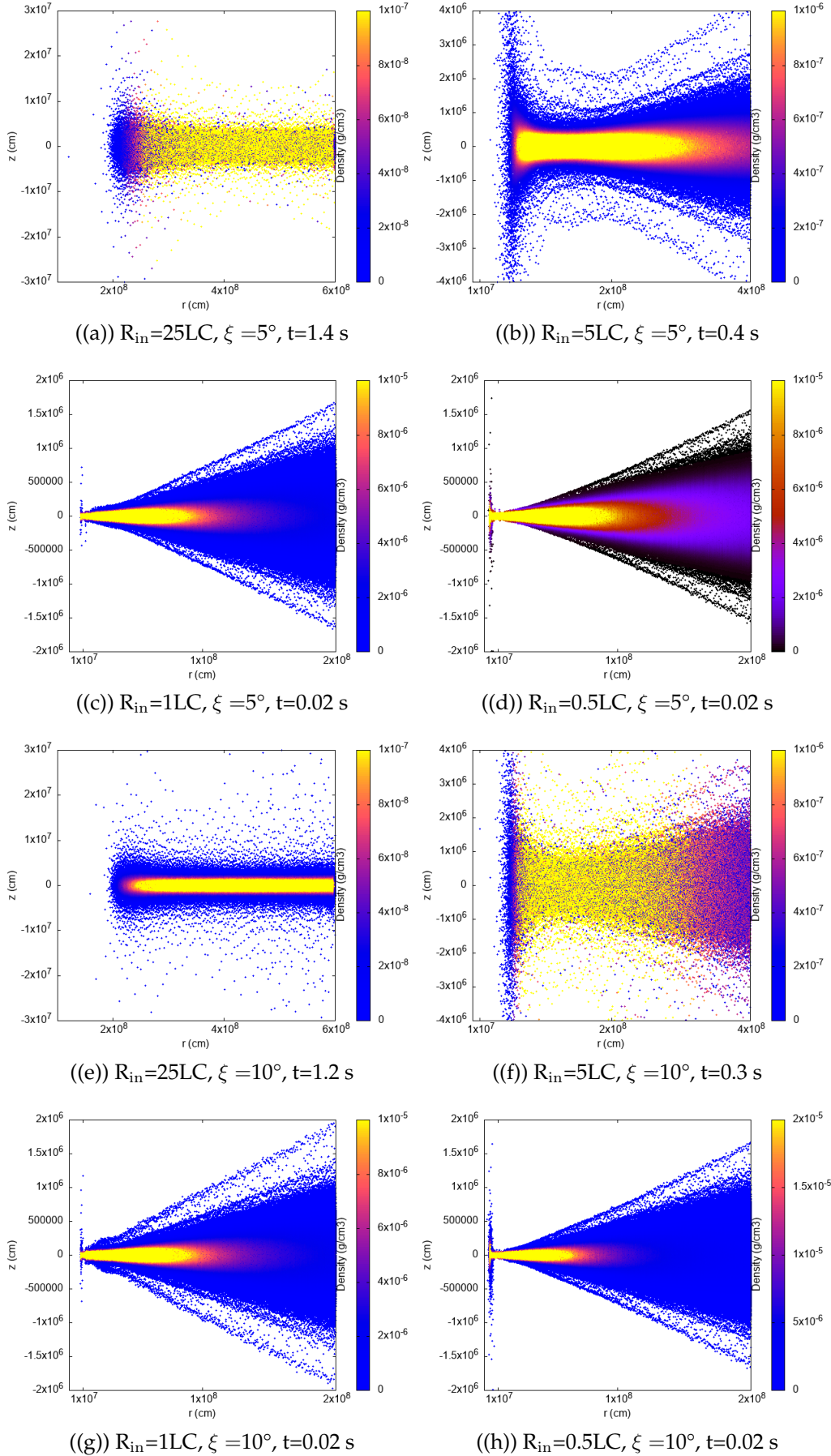
Figure B.1: Disk structure showing the density distribution where the inner disk radius is at 25LC, 5LC, 1LC, 0.5LC.

((a)) R_{in}=25LC, ξ =20°, t=0.8 s

((b)) R_{in}=5LC, ξ =20°, t=0.3 s

((c)) R_{in}=1LC, ξ =20°, t=0.01 s

((d)) R_{in}=0.5LC, ξ =20°, t=0.02 s

((e)) R_{in}=25LC, ξ =30°, t=0.4 s

((f)) R_{in}=5LC, ξ =30°, t=0.3 s

((g)) R_{in}=1LC, ξ =30°, t=0.01 s

((h)) R_{in}=0.5LC, ξ =30°, t=0.01 s
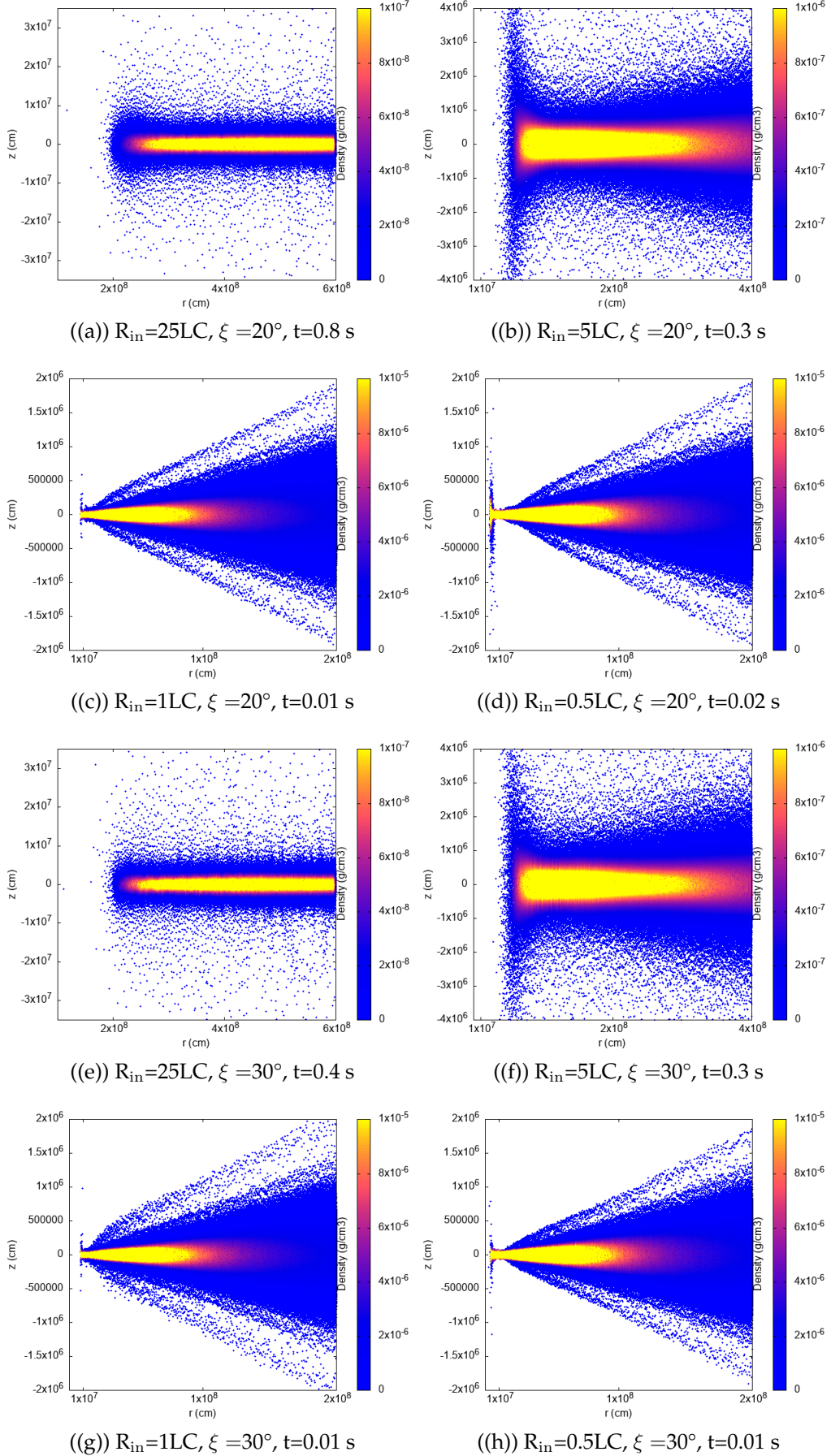
Figure B.2: Disk structure showing the density distribution where the inner disk radius is at 25LC, 5LC, 1LC, 0.5LC.

((a)) R_{in}=25LC, ξ =5°

((b)) R_{in}=25LC, ξ =10°

((c)) R_{in}=25LC, ξ =20°

((d)) R_{in}=25LC, ξ =30°

((e)) R_{in}=5LC, ξ =5°

((f)) R_{in}=5LC, ξ =10°

((g)) R_{in}=5LC, ξ =20°

((h)) R_{in}=5LC, ξ =30°
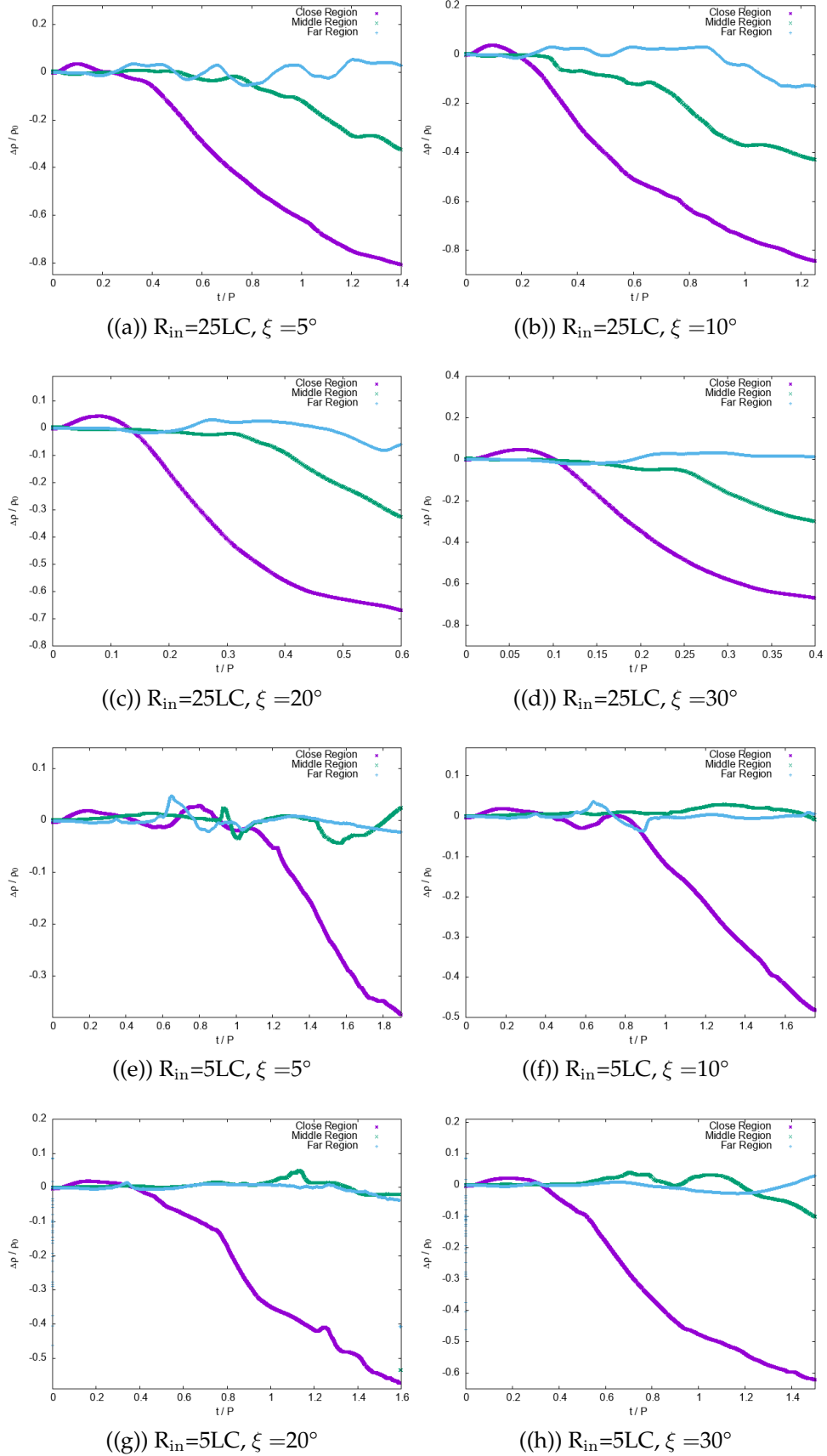
Figure B.3: The ratio of the density change to the initial density. The x-axis represents the simulation time normalized by the Keplerian period at the disk's inner edge (t/P).

((a)) R_{in}=25LC, ξ =5°   ((b)) R_{in}=25LC, ξ =10°

((c)) R_{in}=25LC, ξ =20°   ((d)) R_{in}=25LC, ξ =30°

((e)) R_{in}=5LC, ξ =5°   ((f)) R_{in}=5LC, ξ =10°

((g)) R_{in}=5LC, ξ =20°   ((h)) R_{in}=5LC, ξ =30°
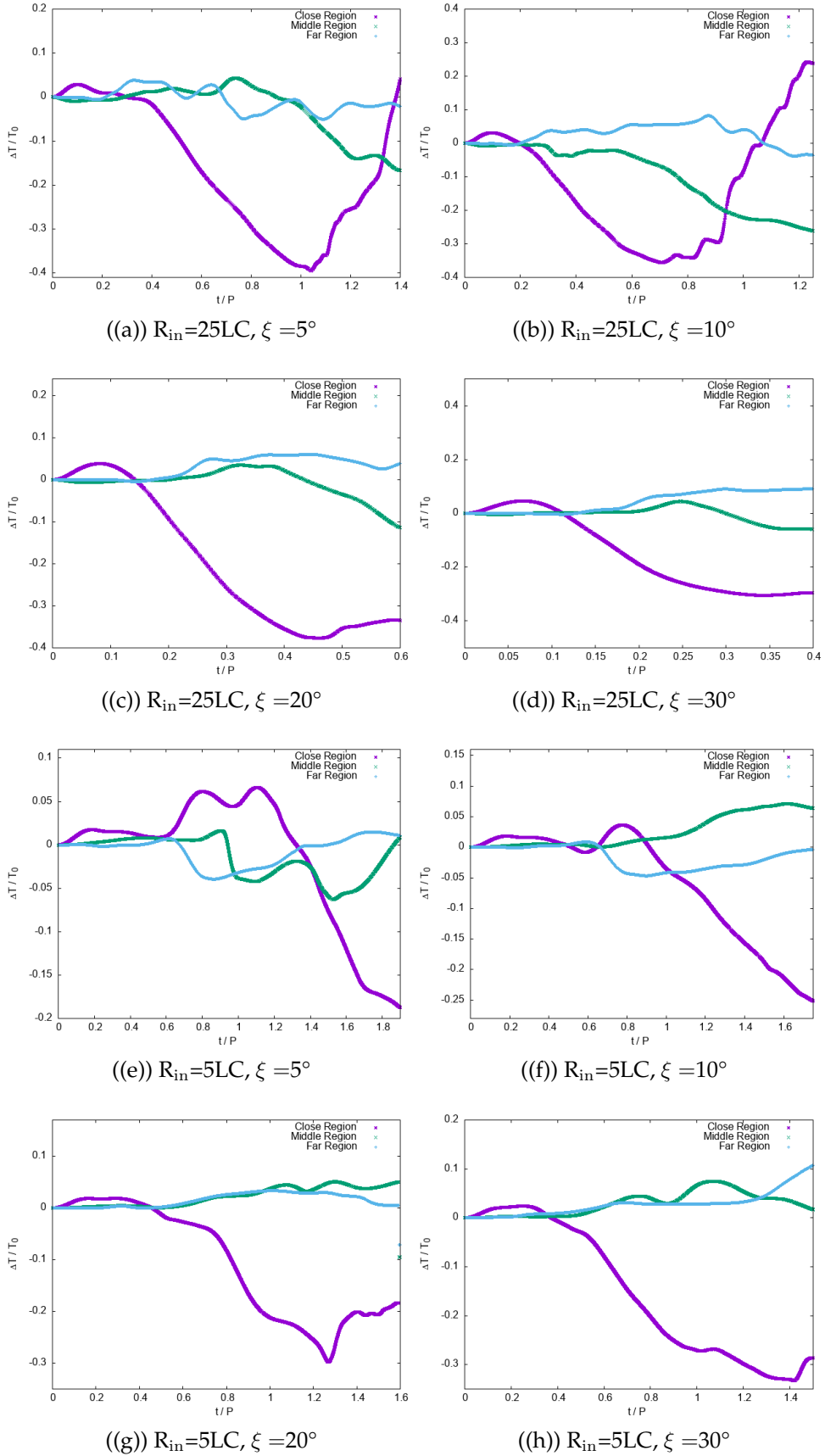
Figure B.4: The ratio of the temperature change to the initial temperature. The x-axis represents the simulation time normalized by the Keplerian period at the disk's inner edge (t/P).
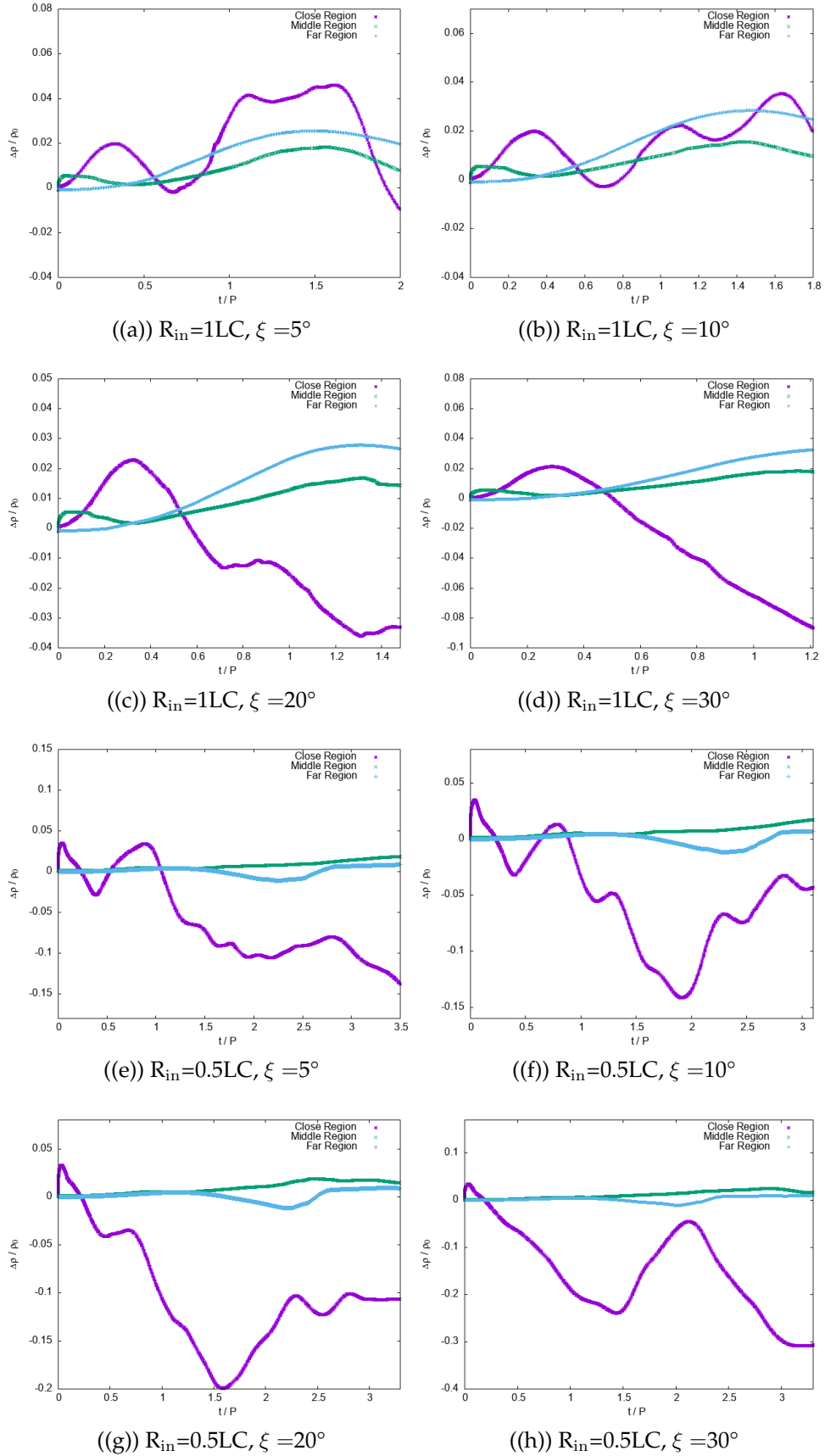
Figure B.5: The ratio of the density change to the initial density. The x-axis represents the simulation time normalized by the Keplerian period at the disk's inner edge (t/P).

((a)) R_{in}=1LC, ξ =5°

((b)) R_{in}=1LC, ξ =10°

((c)) R_{in}=1LC, ξ =20°

((d)) R_{in}=1LC, ξ =30°

((e)) R_{in}=0.5LC, ξ =5°

((f)) R_{in}=0.5LC, ξ =10°

((g)) R_{in}=0.5LC, ξ =20°

((h)) R_{in}=0.5LC, ξ =30°
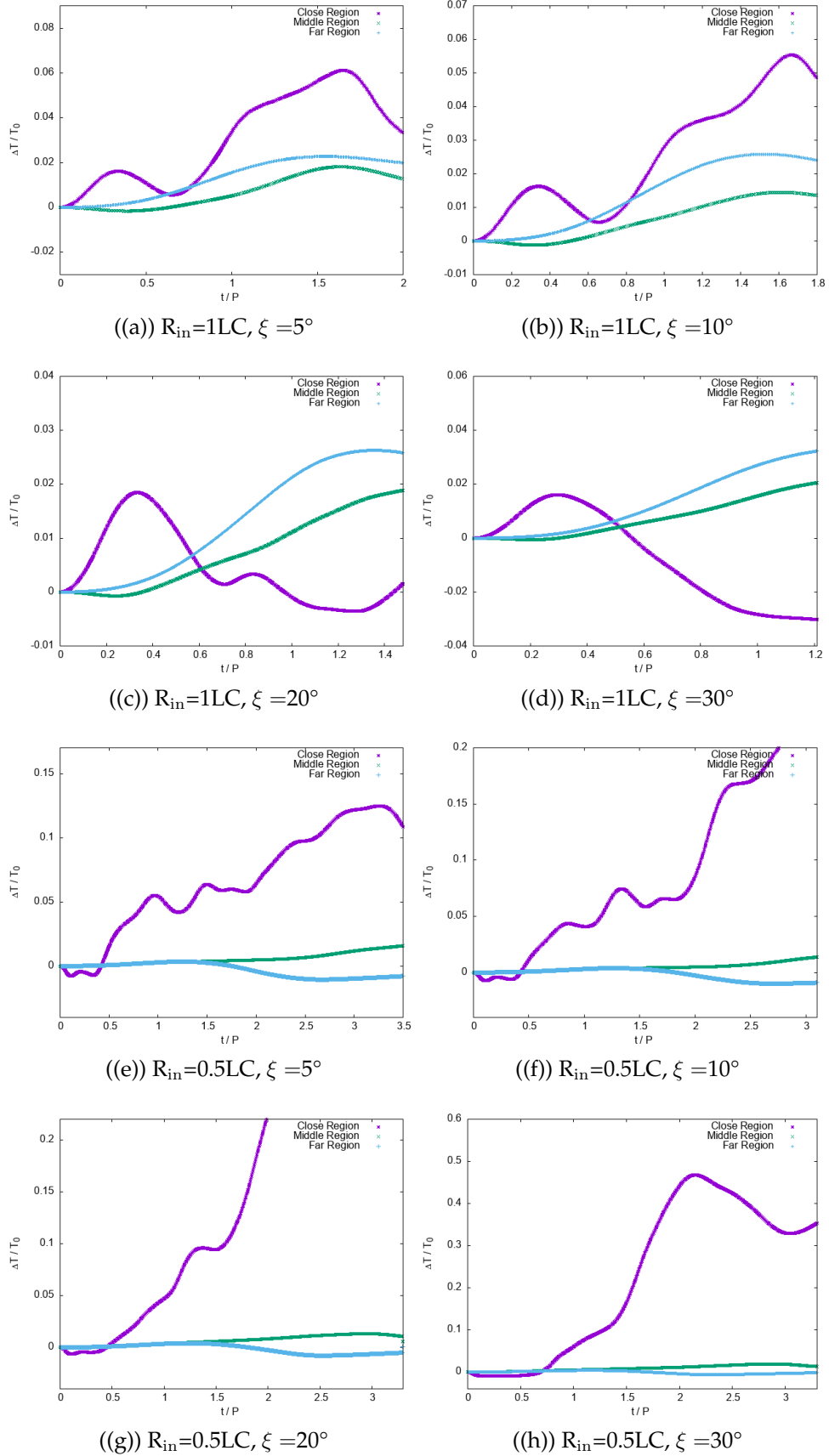
Figure B.6: The ratio of the temperature change to the initial temperature. The x-axis represents the simulation time normalized by the Keplerian period at the disk's inner edge (t/P).

Bibliography

M. A. Alpar, A. F. Cheng, M. A. Ruderman, and J. Shaham. A new class of radio pulsars. , 300:728–730, 1982. doi: 10.1038/300728a0.

A. M. Archibald, I. H. Stairs, S. M. Ransom, V. M. Kaspi, V. I. Kondratiev, D. R. Lorimer, M. A. McLaughlin, J. Boyles, J. W. T. Hessels, R. Lynch, J. van Leeuwen, M. S. E. Roberts, F. Jenet, D. J. Champion, R. Rosen, B. N. Barlow, B. H. Dunlap, and R. A. Remillard. A Radio Pulsar/X-ray Binary Link. *Science*, 324(5933):1411, June 2009a. doi: 10.1126/science.1172740.

A. M. Archibald, I. H. Stairs, S. M. Ransom, V. M. Kaspi, V. I. Kondratiev, D. R. Lorimer, M. A. McLaughlin, J. Boyles, J. W. T. Hessels, R. Lynch, J. van Leeuwen, M. S. E. Roberts, F. Jenet, D. J. Champion, R. Rosen, B. N. Barlow, B. H. Dunlap, and R. A. Remillard. A Radio Pulsar/X-ray Binary Link. *Science*, 324(5933):1411, June 2009b. doi: 10.1126/science.1172740.

A. M. Archibald, V. M. Kaspi, S. Bogdanov, J. W. T. Hessels, I. H. Stairs, S. M. Ransom, and M. A. McLaughlin. X-ray Variability and Evidence for Pulsations from the Unique Radio Pulsar/X-ray Binary Transition Object FIRST J102347.6+003841. , 722(1):88–95, Oct. 2010. doi: 10.1088/0004-637X/722/1/88.

K. A. Arnaud. XSPEC: The First Ten Years. In G. H. Jacoby and J. Barnes, editors, *Astronomical Data Analysis Software and Systems V*, volume 101 of *Astronomical Society of the Pacific Conference Series*, page 17, 1996.

A. Bahramian, C. O. Heinke, G. R. Sivakoff, D. Altamirano, R. Wijnands, J. Homan, M. Linares, D. Pooley, N. Degenaar, and J. C. Gladstone. Discovery of the Third Transient X-Ray Binary in the Galactic Globular Cluster Terzan 5. , 780(2):127, Jan. 2014. doi: 10.1088/0004-637X/780/2/127.

A. Bahramian, J. Strader, J. C. A. Miller-Jones, L. Chomiuk, C. O. Heinke, T. J. Maccarone, D. Pooley, L. Shishkovsky, V. Tudor, Y. Zhao, K. L. Li, G. R. Sivakoff,

E. Tremou, and J. Buchner. The MAVERIC survey: Chandra/ACIS catalog of faint x-ray sources in 38 galactic globular clusters. *The Astrophysical Journal*, 901 (1):57, sep 2020. doi: 10.3847/1538-4357/aba51d. URL https://doi.org/10.3847/1538-4357/aba51d.

D. S. Balsara. von neumann stability analysis of smoothed particle hydrodynamics—suggestions for optimal algorithms. *Journal of Computational Physics*, 121(2): 357–372, 1995. ISSN 0021-9991. doi: https://doi.org/10.1016/S0021-9991(95) 90221-X. URL https://www.sciencedirect.com/science/article/pii/S002199919590221X.

C. Bassa, D. Pooley, L. Homer, F. Verbunt, B. M. Gaensler, W. H. G. Lewin, S. F. Anderson, B. Margon, V. M. Kaspi, and M. van der Klis. Addendum: "X-Ray Sources and Their Optical Counterparts in the Globular Cluster M4" (¡A href="/abs/2004ApJ...609..755B"¿ApJ, 609, 755 [2004]¡/A¿). , 619(2):1189–1189, Feb. 2005. doi: 10.1086/426683.

C. G. Bassa, A. Patruno, J. W. T. Hessels, E. F. Keane, B. Monard, E. K. Mahony, S. Bogdanov, S. Corbel, P. G. Edwards, A. M. Archibald, G. H. Janssen, B. W. Stappers, and S. Tendulkar. A state change in the low-mass X-ray binary XSS J12270-4859. , 441(2):1825–1830, June 2014. doi: 10.1093/mnras/stu708.

W. Becker, D. A. Swartz, G. G. Pavlov, R. F. Elsner, J. Grindlay, R. Mignani, A. F. Tennant, D. Backer, L. Pulone, V. Testa, and et al. Chandra x-ray observatoryobservations of the globular cluster m28 and its millisecond pulsar psr b182124. *The Astrophysical Journal*, 594(2):798–811, Sep 2003. ISSN 1538-4357. doi: 10.1086/376967. URL http://dx.doi.org/10.1086/376967.

S. Bégin. A search for fast pulsars in globular clusters. Master's thesis, University of British Columbia, Oct. 2006.

S. Bogdanov, J. E. Grindlay, and M. van den Berg. An X-Ray Variable Millisecond Pulsar in the Globular Cluster 47 Tucanae: Closing the Link to Low-Mass X-Ray Binaries. , 630:1029–1036, 2005. doi: 10.1086/432249.

S. Bogdanov, J. E. Grindlay, C. O. Heinke, F. Camilo, P. C. C. Freire, and W. Becker. ChandraX-ray observations of 19 millisecond pulsars in the globular cluster 47 tucanae. *The Astrophysical Journal*, 646(2):1104–1115, aug 2006. doi: 10.1086/505133. URL https://doi.org/10.1086/505133.

S. Bogdanov, M. van den Berg, M. Servillat, C. O. Heinke, J. E. Grindlay, I. H. Stairs, S. M. Ransom, P. C. C. Freire, S. Bégin, and W. Becker. Chandra X-ray Observations of 12 Millisecond Pulsars in the Globular Cluster M28. , 730(2):81, Apr. 2011. doi: 10.1088/0004-637X/730/2/81.

S. Bogdanov, C. O. Heinke, F. Özel, and T. Güver. Neutron Star Mass-Radius Constraints of the Quiescent Low-mass X-Ray Binaries X7 and X5 in the Globular Cluster 47 Tuc. , 831(2):184, Nov. 2016. doi: 10.3847/0004-637X/831/2/184.

I. Bombaci. The maximum mass of a neutron star. , 305:871, Jan. 1996.

R. M. Cabezón, D. García-Senz, and J. Figueira. SPHYNX: an accurate density-based SPH method for astrophysical applications. , 606:A78, Oct. 2017a. doi: 10.1051/0004-6361/201630208.

R. M. Cabezón, D. García-Senz, and J. Figueira. SPHYNX: an accurate density-based SPH method for astrophysical applications. , 606:A78, Oct. 2017b. doi: 10.1051/0004-6361/201630208.

P. R. A. Cairns. Plasma Physics and Fusion Energy, by J. Freidberg. *Contemporary Physics*, 50(5):605–606, Sept. 2009. doi: 10.1080/00107510902885284.

F. Camilo and F. A. Rasio. Pulsars in Globular Clusters. In F. A. Rasio and I. H. Stairs, editors, *Binary Radio Pulsars*, volume 328 of *Astronomical Society of the Pacific Conference Series*, page 147, July 2005a. doi: 10.48550/arXiv.astro-ph/0501226.

F. Camilo and F. A. Rasio. Pulsars in Globular Clusters. In F. A. Rasio and I. H. Stairs, editors, *Binary Radio Pulsars*, volume 328 of *Astronomical Society of the Pacific Conference Series*, page 147, 2005b.

S. Campana, M. Colpi, S. Mereghetti, L. Stella, and M. Tavani. The neutron stars of Soft X-ray Transients. , 8(4):279–316, Jan. 1998. doi: 10.1007/s001590050012.

S. Campana, N. Ferrari, L. Stella, and G. L. Israel. XMM-Newton observations of two transient millisecond X-ray pulsars in quiescence. , 434(3):L9–L12, May 2005. doi: 10.1051/0004-6361:200500103.

B. Cerutti, A. A. Philippov, and A. Spitkovsky. Modelling high-energy pulsar light curves from first principles. , 457(3):2401–2414, Apr. 2016. doi: 10.1093/mnras/stw124.

B. Cerutti, A. A. Philippov, and G. Dubus. Dissipation of the striped pulsar wind and non-thermal particle acceleration: 3D PIC simulations. , 642:A204, Oct. 2020a. doi: 10.1051/0004-6361/202038618.

B. Cerutti, A. A. Philippov, and G. Dubus. Dissipation of the striped pulsar wind and non-thermal particle acceleration: 3D PIC simulations. , 642:A204, Oct. 2020b. doi: 10.1051/0004-6361/202038618.

Z. Cheng, H. Mu, Z. Li, X. Xu, W. Wang, and X. Li. Exploring the mass segregation effect of x-ray sources in globular clusters. iii. signs of binary disruption in m28. *The Astrophysical Journal*, 892(1):16, Mar 2020. ISSN 1538-4357. doi: 10.3847/1538-4357/ab7933. URL http://dx.doi.org/10.3847/1538-4357/ab7933.

P. B. Cho, J. P. Halpern, and S. Bogdanov. Variable heating and flaring of three redback millisecond pulsar companions. *The Astrophysical Journal*, 866(1):71, Oct 2018. ISSN 1538-4357. doi: 10.3847/1538-4357/aade92. URL http://dx.doi.org/10.3847/1538-4357/aade92.

H. N. Cohn, P. M. Lugger, S. Bogdanov, C. O. Heinke, M. Van Den Berg, and G. Sivakoff. HST search of the region around IGR J18245-2452. *The Astronomer's Telegram*, 5031:1, Apr. 2013.

K. Davidson and J. P. Ostriker. Neutron-Star Accretion in a Stellar Wind: Model for a Pulsed X-Ray Source. , 179:585–598, Jan. 1973. doi: 10.1086/151897.

J. E. Davis. Event pileup in charge-coupled devices. *The Astrophysical Journal*, 562(1):575–582, nov 2001. doi: 10.1086/323488. URL https://doi.org/10.1086/323488.

A. T. Deller, A. M. Archibald, W. F. Brisken, S. Chatterjee, G. H. Janssen, V. M. Kaspi, D. Lorimer, A. G. Lyne, M. A. McLaughlin, S. Ransom, I. H. Stairs, and B. Stappers. A Parallax Distance and Mass Estimate for the Transitional Millisecond Pulsar System J1023+0038. , 756(2):L25, Sept. 2012. doi: 10.1088/2041-8205/756/2/L25.

A. J. Deutsch. The electromagnetic field of an idealized star in rigid rotation in vacuo. *Annales d'Astrophysique*, 18:1, Jan. 1955.

T. Di Salvo and L. Burderi. Constraints on the neutron star magnetic field of the two X-ray transients SAX J1808.4-3658 and Aql X-1. , 397:723–727, Jan. 2003. doi: 10.1051/0004-6361:20021491.

A. Douglas, P. V. Padmanabh, S. M. Ransom, A. Ridolfi, P. Freire, V. V. Krishnan, E. D. Barr, C. Pallanca, M. Cadelano, A. Possenti, I. Stairs, J. W. T. Hessels, M. E. DeCesar, R. S. Lynch, M. Bailes, M. Burgay, D. J. Champion, R. Karuppusamy, M. Kramer, B. Stappers, and L. Vleeschower. Two new black widow millisecond pulsars in m28. *The Astrophysical Journal*, 927(1):126, mar 2022. doi: 10.3847/ 1538-4357/ac4744. URL https://doi.org/10.3847/1538-4357/ac4744.

R. C. Duncan and C. Thompson. Formation of Very Strongly Magnetized Neutron Stars: Implications for Gamma-Ray Bursts. , 392:L9, June 1992. doi: 10.1086/ 186413.

K. Y. Ekşi and M. A. Alpar. Disks Surviving the Radiation Pressure of Radio Pulsars. , 620(1):390–397, Feb. 2005. doi: 10.1086/425959.

J. Frank, A. King, and D. J. Raine. *Accretion Power in Astrophysics: Third Edition.* 2002a.

J. Frank, A. King, and D. J. Raine. *Accretion Power in Astrophysics: Third Edition.* 2002b.

P. Freire. Pulsars in globular clusters, online catalog, 2021. URL http://www. naic.edu/~pfreire/GCpsr.html.

J. K. Fridriksson, J. Homan, R. Wijnands, M. Méndez, D. Altamirano, E. M. Cackett, E. F. Brown, T. M. Belloni, N. Degenaar, and W. H. G. Lewin. RAPID COOLING OF THE NEUTRON STAR IN THE QUIESCENT SUPER-EDDINGTON TRANSIENT XTE j1701–462. *The Astrophysical Journal*, 714(1):270–286, apr 2010. doi: 10.1088/0004-637x/714/1/270. URL https://doi.org/10. 1088/0004-637x/714/1/270.

A. S. Fruchter, D. R. Stinebring, and J. H. Taylor. A millisecond pulsar in an eclipsing binary. In H. Ögelman and E. P. J. van den Heuvel, editors, *Timing Neutron Stars*, volume 262 of *NATO Advanced Study Institute (ASI) Series C*, page 163, Jan. 1989. doi: 10.1007/978-94-009-2273-0_13.

A. Fruscione, J. C. McDowell, G. E. Allen, N. S. Brickhouse, D. J. Burke, J. E. Davis, N. Durham, M. Elvis, E. C. Galle, D. E. Harris, D. P. Huenemoerder, J. C. Houck, B. Ishibashi, M. Karovska, F. Nicastro, M. S. Noble, M. A. Nowak, F. A. Primini, A. Siemiginowska, R. K. Smith, and M. Wise. CIAO: Chandra's data analysis system. In D. R. Silva and R. E. Doxsey, editors, *Society of Photo-Optical Instrumentation Engineers (SPIE) Conference Series*, volume 6270 of *Society of Photo-Optical Instrumentation Engineers (SPIE) Conference Series*, page 62701V, June 2006. doi: 10.1117/12.671760.

D. García-Senz, R. M. Cabezón, J. M. Blanco-Iglesias, and P. Lorén-Aguilar. Self-gravitating barotropic equilibrium configurations of rotating bodies with smoothed particle hydrodynamics. , 637:A61, May 2020. doi: 10.1051/0004-6361/201936837.

D. García-Senz, R. Wissing, and R. M. Cabezón. Axisymmetric magneto-hydrodynamics with SPH. *arXiv e-prints*, art. arXiv:2206.05324, June 2022. doi: 10.48550/arXiv.2206.05324.

D. García-Senz, R. Wissing, R. M. Cabezón, E. Vurgun, and M. Linares. Axisymmetric smoothed particle magnetohydrodynamics. , 518(3):4115–4131, Jan. 2023a. doi: 10.1093/mnras/stac3328.

D. García-Senz, R. Wissing, R. M. Cabezón, E. Vurgun, and M. Linares. Axisymmetric smoothed particle magnetohydrodynamics. , 518(3):4115–4131, Jan. 2023b. doi: 10.1093/mnras/stac3328.

R. A. Gingold and J. J. Monaghan. Smoothed particle hydrodynamics: theory and application to non-spherical stars. , 181:375–389, Nov. 1977. doi: 10.1093/mnras/181.3.375.

J. Goodman and G. Xu. Parasitic Instabilities in Magnetized, Differentially Rotating Disks. , 432:213, Sept. 1994. doi: 10.1086/174562.

S. Guillot, R. E. Rutledge, E. F. Brown, G. G. Pavlov, and V. E. Zavlin. Discovery of a Candidate Quiescent Low-mass X-Ray Binary in the Globular Cluster NGC 6553. , 738(2):129, Sept. 2011. doi: 10.1088/0004-637X/738/2/129.

W. E. Harris. A Catalog of Parameters for Globular Clusters in the Milky Way. , 112:1487, Oct. 1996. doi: 10.1086/118116.

W. E. Harris. A new catalog of globular clusters in the milky way, 2010.

C. O. Heinke, G. B. Rybicki, R. Narayan, and J. E. Grindlay. A Hydrogen Atmosphere Spectral Model Applied to the Neutron Star X7 in the Globular Cluster 47 Tucanae. , 644(2):1090–1103, June 2006. doi: 10.1086/503701.

C. O. Heinke, H. N. Cohn, P. M. Lugger, N. A. Webb, W. C. G. Ho, J. Anderson, S. Campana, S. Bogdanov, D. Haggard, A. M. Cool, and J. E. Grindlay. Improved mass and radius constraints for quiescent neutron stars in ω Cen and NGC 6397. , 444(1):443–456, Oct. 2014. doi: 10.1093/mnras/stu1449.

W. C. G. Ho and C. O. Heinke. A neutron star with a carbon atmosphere in the Cassiopeia A supernova remnant. , 462(7269):71–73, Nov. 2009. doi: 10.1038/nature08525.

J. Hong, M. van den Berg, E. M. Schlegel, J. E. Grindlay, X. Koenig, S. Laycock, and P. Zhao. X-Ray Processing of ChaMPlane Fields: Methods and Initial Results for Selected Anti-Galactic Center Fields. , 635(2):907–919, Dec. 2005. doi: 10.1086/496966.

C. Y. Hui, C. P. Hu, S. M. Park, J. Takata, K. L. Li, P. H. T. Tam, L. C. C. Lin, A. K. H. Kong, K. S. Cheng, and C. Kim. Exploring the intrabinary shock from the redback millisecond pulsar psr j2129-0429. *The Astrophysical Journal*, 801 (2):L27, Mar 2015. ISSN 2041-8213. doi: 10.1088/2041-8205/801/2/l27. URL http://dx.doi.org/10.1088/2041-8205/801/2/L27.

N. Hynes. Credit: Nasa/r. hynes. https://www.cosmos.esa.int/web/cesar/X-ray-binaries-monitoring.

D. Kandel, R. W. Romani, and H. An. The synchrotron emission pattern of intrabinary shocks. *The Astrophysical Journal*, 879(2):73, jul 2019. doi: 10.3847/1538-4357/ab24d9. URL https://doi.org/10.3847%2F1538-4357%2Fab24d9.

M. Linares. X-Ray States of Redback Millisecond Pulsars. , 795(1):72, Nov. 2014a. doi: 10.1088/0004-637X/795/1/72.

M. Linares. X-ray states of redback millisecond pulsars. , 795:72, 2014b. doi: 10.1088/0004-637X/795/1/72.

M. Linares, A. Bahramian, C. Heinke, R. Wijnands, A. Patruno, D. Altamirano, J. Homan, S. Bogdanov, and D. Pooley. The neutron star transient and millisecond pulsar in M28: from sub-luminous accretion to rotation-powered quiescence. , 438(1):251–261, Feb. 2014a. doi: 10.1093/mnras/stt2167.

M. Linares, J. Casares, P. Rodriguez-Gil, and T. Shahbaz. PSR J1023+0038: phase-resolved optical spectroscopy and continued X-ray activity. *The Astronomer's Telegram*, 5868:1, Feb. 2014b.

V. M. Lipunov. *Astrophysics of Neutron Stars*. 1992.

D. Lorimer. Galactic Millisecond Pulsars. *Online catalog at http://astro.phys.wvu.edu/GalacticMSPs*, 2019.

D. R. Lorimer. Binary and Millisecond Pulsars. *Living Reviews in Relativity*, 11:8, 2008. doi: 10.12942/lrr-2008-8.

D. R. Lorimer and M. Kramer. *Handbook of Pulsar Astronomy*, volume 4. 2004.

L. B. Lucy. A numerical approach to the testing of the fission hypothesis. , 82:1013–1024, Dec. 1977. doi: 10.1086/112164.

A. G. Lyne, A. Brinklow, J. Middleditch, S. R. Kulkarni, and D. C. Backer. The discovery of a millisecond pulsar in the globular cluster M28. , 328(6129):399–401, July 1987. doi: 10.1038/328399a0.

T. Maccarone and C. Knigge. Compact objects in globular clusters. *Astronomy and Geophysics*, 48(5):5.12–5.20, Oct. 2007. doi: 10.1111/j.1468-4004.2007.48512.x.

R. N. Manchester, G. B. Hobbs, A. Teoh, and M. Hobbs. The australia telescope national facility pulsar catalogue. *The Astronomical Journal*, 129(4):1993–2006, apr 2005. doi: 10.1086/428488. URL https://doi.org/10.1086%2F428488.

L. Mestel and J. D. Landstreet. Stellar Magnetic Fields. In R. Wielebinski and R. Beck, editors, *Cosmic Magnetic Fields*, volume 664, page 183. 2005. doi: 10.1007/3540313966_8.

F. C. Michel and H. Li. Electrodynamics of neutron stars. , 318(6):227–297, Sept. 1999. doi: 10.1016/S0370-1573(99)00002-2.

M. C. Miller, F. K. Lamb, A. J. Dittmann, S. Bogdanov, Z. Arzoumanian, K. C. Gendreau, S. Guillot, W. C. G. Ho, J. M. Lattimer, M. Loewenstein, and et al. The radius of psr j0740+6620 from nicer and xmm-newton data. *The Astrophysical Journal Letters*, 918(2):L28, Sep 2021. ISSN 2041-8213. doi: 10.3847/2041-8213/ ac089b. URL `http://dx.doi.org/10.3847/2041-8213/ac089b`.

J. J. Monaghan. SPH and Riemann Solvers. *Journal of Computational Physics*, 136(2): 298–307, Sept. 1997. doi: 10.1006/jcph.1997.5732.

C. Pallanca, E. Dalessandro, F. R. Ferraro, B. Lanzoni, and G. Beccari. The Optical Counterpart to the X-Ray Transient IGR J1824-24525 in the Globular Cluster M28. , 773(2):122, Aug. 2013. doi: 10.1088/0004-637X/773/2/122.

A. Papitto and D. de Martino. Transitional millisecond pulsars, 2020.

A. Papitto and D. de Martino. Transitional Millisecond Pulsars. In S. Bhattacharyya, A. Papitto, and D. Bhattacharya, editors, *Astrophysics and Space Science Library*, volume 465 of *Astrophysics and Space Science Library*, pages 157–200, Jan. 2022a. doi: 10.1007/978-3-030-85198-9_6.

A. Papitto and D. de Martino. Transitional Millisecond Pulsars. In S. Bhattacharyya, A. Papitto, and D. Bhattacharya, editors, *Astrophysics and Space Science Library*, volume 465 of *Astrophysics and Space Science Library*, pages 157–200, Jan. 2022b. doi: 10.1007/978-3-030-85198-9_6.

A. Papitto and D. F. Torres. A Propeller Model for the Sub-luminous State of the Transitional Millisecond Pulsar PSR J1023+0038. , 807(1):33, July 2015. doi: 10. 1088/0004-637X/807/1/33.

A. Papitto, C. Ferrigno, E. Bozzo, N. Rea, L. Pavan, L. Burderi, M. Burgay, S. Campana, T. di Salvo, M. Falanga, M. D. Filipović, P. C. C. Freire, J. W. T. Hessels, A. Possenti, S. M. Ransom, A. Riggio, P. Romano, J. M. Sarkissian, I. H. Stairs, L. Stella, D. F. Torres, M. H. Wieringa, and G. F. Wong. Swings between rotation and accretion power in a binary millisecond pulsar. , 501(7468):517–520, Sept. 2013. doi: 10.1038/nature12470.

K. Parfrey and A. Tchekhovskoy. General-relativistic Simulations of Four States of Accretion onto Millisecond Pulsars. , 851(2):L34, Dec. 2017. doi: 10.3847/ 2041-8213/aa9c85.

K. Parfrey, A. Spitkovsky, and A. M. Beloborodov. Simulations of the magnetospheres of accreting millisecond pulsars. , 469(3):3656–3669, Aug. 2017. doi: 10.1093/mnras/stx950.

E. N. Parker. *Cosmical magnetic fields. Their origin and their activity.* 1979.

D. J. Price. Smoothed particle hydrodynamics and magnetohydrodynamics. *Journal of Computational Physics*, 231(3):759–794, Feb. 2012a. doi: 10.1016/j.jcp.2010.12.011.

D. J. Price. Smoothed particle hydrodynamics and magnetohydrodynamics. *Journal of Computational Physics*, 231:759–794, Feb. 2012b. doi: 10.1016/j.jcp.2010.12.011.

D. J. Price, J. Wurster, T. S. Tricco, C. Nixon, S. Toupin, A. Pettitt, C. Chan, D. Mentiplay, G. Laibe, S. Glover, C. Dobbs, R. Nealon, D. Liptai, H. Worpel, C. Bonnerot, G. Dipierro, G. Ballabio, E. Ragusa, C. Federrath, R. Iaconi, T. Reichardt, D. Forgan, M. Hutchison, T. Constantino, B. Ayliffe, K. Hirsh, and G. Lodato. Phantom: A Smoothed Particle Hydrodynamics and Magnetohydrodynamics Code for Astrophysics. , 35:e031, Sept. 2018. doi: 10.1017/pasa.2018.25.

E. Priest and T. Forbes. *Magnetic Reconnection: MHD Theory and Applications.* 2000. doi: 10.1017/CBO9780511525087.

J. E. Pringle and M. J. Rees. Accretion Disc Models for Compact X-Ray Sources. , 21:1, Oct. 1972.

S. M. Ransom. Twenty Years of Searching for (and Finding) Globular Cluster Pulsars. In C. Bassa, Z. Wang, A. Cumming, and V. M. Kaspi, editors, *40 Years of Pulsars: Millisecond Pulsars, Magnetars and More*, volume 983 of *American Institute of Physics Conference Series*, pages 415–423, 2008. doi: 10.1063/1.2900267.

T. E. Riley, A. L. Watts, P. S. Ray, S. Bogdanov, S. Guillot, S. M. Morsink, A. V. Bilous, Z. Arzoumanian, D. Choudhury, J. S. Deneva, K. C. Gendreau, A. K. Harding, W. C. G. Ho, J. M. Lattimer, M. Loewenstein, R. M. Ludlam, C. B. Markwardt, T. Okajima, C. Prescod-Weinstein, R. A. Remillard, M. T. Wolff, E. Fonseca, H. T. Cromartie, M. Kerr, T. T. Pennucci, A. Parthasarathy, S. Ransom, I. Stairs, L. Guillemot, and I. Cognard. A NICER View of the Massive Pulsar PSR J0740+6620 Informed by Radio Timing and XMM-Newton Spectroscopy. , 918(2):L27, Sept. 2021. doi: 10.3847/2041-8213/ac0a81.

M. S. E. Roberts. Surrounded by spiders! New black widows and redbacks in the Galactic field. In J. van Leeuwen, editor, *Neutron Stars and Pulsars: Challenges and Opportunities after 80 years*, volume 291, pages 127–132, Mar. 2013. doi: 10.1017/ S174392131202337X.

R. W. Romani and N. Sanchez. INTRA-BINARY SHOCK HEATING OF BLACK WIDOW COMPANIONS. *The Astrophysical Journal*, 828(1):7, aug 2016. doi: 10.3847/0004-637x/828/1/7. URL https://doi.org/10.3847%2F0004-637x%2F828%2F1%2F7.

M. M. Romanova, A. V. Koldoba, G. V. Ustyugova, A. A. Blinova, D. Lai, and R. V. E. Lovelace. 3D MHD simulations of accretion on to stars with tilted magnetic and rotational axes. , 506(1):372–384, Sept. 2021. doi: 10.1093/mnras/ stab1724.

R. E. Rutledge, L. Bildsten, E. F. Brown, G. G. Pavlov, V. E. Zavlin, and G. Ushomirsky. Crustal emission and the quiescent spectrum of the neutron star in KS 1731-260. *The Astrophysical Journal*, 580(1):413–422, nov 2002. doi: 10.1086/342745. URL https://doi.org/10.1086/342745.

Saeedi, Sara, Liu, Teng, Knies, Jonathan, Sasaki, Manami, Becker, Werner, Bulbul, Esra, Dennerl, Konrad, Freyberg, Michael, Laktionov, Roman, and Merloni, Andrea. erosita study of the globular cluster 47 tucanae. *A&A*, 661:A35, 2022. doi: 10.1051/0004-6361/202141612. URL https://doi.org/10.1051/ 0004-6361/202141612.

M. Servillat, C. O. Heinke, W. C. G. Ho, J. E. Grindlay, J. Hong, M. van den Berg, and S. Bogdanov. Neutron star atmosphere composition: the quiescent, low-mass x-ray binary in the globular cluster m28. *Monthly Notices of the Royal Astronomical Society*, 423(2):1556–1561, May 2012. ISSN 0035-8711. doi: 10.1111/j.1365-2966.2012.20976.x. URL http://dx.doi.org/10.1111/ j.1365-2966.2012.20976.x.

N. I. Shakura and R. A. Sunyaev. Black holes in binary systems. Observational appearance. , 24:337–355, Jan. 1973.

S. L. Shapiro and S. A. Teukolsky. *Black holes, white dwarfs and neutron stars. The physics of compact objects*. 1983. doi: 10.1002/9783527617661.

V. F. Shvartsman. The Influence of Stellar Wind on Accretion. , 14:527, Dec. 1970.

V. F. Shvartsman. Neutron Stars in Binary Systems Should Not Be Pulsars. , 15:342, Oct. 1971.

V. Springel and L. Hernquist. Cosmological smoothed particle hydrodynamics simulations: a hybrid multiphase model for star formation. , 339(2):289–311, Feb. 2003. doi: 10.1046/j.1365-8711.2003.06206.x.

H. C. Spruit. Essential magnetohydrodynamics for astrophysics, 2016.

B. W. Stappers, A. M. Archibald, J. W. T. Hessels, C. G. Bassa, S. Bogdanov, G. H. Janssen, V. M. Kaspi, A. G. Lyne, A. Patruno, S. Tendulkar, A. B. Hill, and T. Glanzman. A STATE CHANGE IN THE MISSING LINK BINARY PULSAR SYSTEM PSR j10230038. *The Astrophysical Journal*, 790(1):39, jul 2014. doi: 10.1088/0004-637x/790/1/39. URL https://doi.org/10.1088%2F0004-637x%2F790%2F1%2F39.

A. W. Steiner, C. O. Heinke, S. Bogdanov, C. K. Li, W. C. G. Ho, A. Bahramian, and S. Han. Constraining the mass and radius of neutron stars in globular clusters. , 476(1):421–435, May 2018. doi: 10.1093/mnras/sty215.

J. M. Stone. Astrophysical magnetohydrodynamics. *Bulletin of the Astronomical Society of India*, 39:129–143, Mar. 2011.

V. F. Suleimanov, D. Klochkov, G. G. Pavlov, and K. Werner. Carbon Neutron Star Atmospheres. , 210(1):13, Jan. 2014. doi: 10.1088/0067-0049/210/1/13.

T. S. Tricco. Smoothed particle magnetohydrodynamics. *Frontiers in Astronomy and Space Sciences*, 10:1288219, Dec. 2023. doi: 10.3389/fspas.2023.1288219.

T. S. Tricco, D. J. Price, and M. R. Bate. Constrained hyperbolic divergence cleaning in smoothed particle magnetohydrodynamics with variable cleaning speeds. *Journal of Computational Physics*, 322:326–344, Oct. 2016. doi: 10.1016/j.jcp.2016.06.053.

C. J. T. van der Merwe, Z. Wadiasingh, C. Venter, A. K. Harding, and M. G. Baring. X-ray through very high energy intrabinary shock emission from black widows and redbacks. *The Astrophysical Journal*, 904(2):91, Nov 2020. ISSN 1538-4357. doi: 10.3847/1538-4357/abbdfb. URL http://dx.doi.org/10.3847/1538-4357/abbdfb.

F. Verbunt and W. H. G. Lewin. Globular cluster x-ray sources, 2005.

F. Verbunt and W. H. G. Lewin. Globular cluster X-ray sources. In *Compact stellar X-ray sources*, volume 39, pages 341–379. 2006. doi: 10.48550/arXiv.astro-ph/0404136.

E. Vurgun, M. Linares, S. Ransom, A. Papitto, S. Bogdanov, E. Bozzo, N. Rea, D. García-Senz, P. Freire, and I. Stairs. The Neutron Star Population in M28: A Joint Chandra/GBT Look at Pulsar Paradise. , 941(1):76, Dec. 2022. doi: 10.3847/1538-4357/ac9ea0.

Z. Wadiasingh, A. K. Harding, C. Venter, M. Böttcher, and M. G. Baring. Constraining Relativistic Bow Shock Properties in Rotation-powered Millisecond Pulsar Binaries. , 839:80, Apr. 2017. doi: 10.3847/1538-4357/aa69bf.

Z. Wadiasingh, C. Venter, A. K. Harding, M. Böttcher, and P. Kilian. Pressure Balance and Intrabinary Shock Stability in Rotation-powered-state Redback and Transitional Millisecond Pulsar Binary Systems. , 869(2):120, Dec. 2018. doi: 10.3847/1538-4357/aaed43.

R. Wijnands and N. Degenaar. A low-level accretion flare during the quiescent state of the neutron-star X-ray transient SAX J1750.8-2900. , 434(2):1599–1603, Sept. 2013. doi: 10.1093/mnras/stt1119.

R. Wijnands, C. O. Heinke, D. Pooley, P. D. Edmonds, W. H. G. Lewin, J. E. Grindlay, P. G. Jonker, and J. M. Miller. The Hard Quiescent Spectrum of the Neutron Star X-Ray Transient EXO 1745-248 in the Globular Cluster Terzan 5. , 618(2):883–890, Jan. 2005a. doi: 10.1086/426127.

R. Wijnands, J. Homan, C. O. Heinke, J. M. Miller, and W. H. G. Lewin. Chandra Observations of the Accretion-driven Millisecond X-Ray Pulsars XTE J0929-314 and XTE J1751-305 in Quiescence. , 619(1):492–502, Jan. 2005b. doi: 10.1086/426379.

R. Wijnands, N. Degenaar, M. Armas Padilla, D. Altamirano, Y. Cavecchi, M. Linares, A. Bahramian, and C. O. Heinke. Low-level accretion in neutron star X-ray binaries. *Monthly Notices of the Royal Astronomical Society*, 454 (2):1371–1386, 10 2015. ISSN 0035-8711. doi: 10.1093/mnras/stv1974. URL https://doi.org/10.1093/mnras/stv1974.

J. Wilms, A. Allen, and R. McCray. On the Absorption of X-Rays in the Interstellar Medium. , 542:914–924, Oct. 2000. doi: 10.1086/317016.

R. Wissing and S. Shen. Smoothed particle magnetohydrodynamics with the geometric density average force expression. , 638:A140, June 2020. doi: 10.1051/ 0004-6361/201936739.

C. Zanni and J. Ferreira. MHD simulations of accretion onto a dipolar magnetosphere. I. Accretion curtains and the disk-locking paradigm. , 508(3):1117–1133, Dec. 2009a. doi: 10.1051/0004-6361/200912879.

C. Zanni and J. Ferreira. MHD simulations of accretion onto a dipolar magnetosphere. I. Accretion curtains and the disk-locking paradigm. , 508(3):1117–1133, Dec. 2009b. doi: 10.1051/0004-6361/200912879.

C. Zanni and J. Ferreira. MHD simulations of accretion onto a dipolar magnetosphere. II. Magnetospheric ejections and stellar spin-down. , 550:A99, Feb. 2013. doi: 10.1051/0004-6361/201220168.

J. Zhao and C. O. Heinke. A Chandra X-ray study of millisecond pulsars in the globular cluster Omega Centauri: a correlation between spider pulsar companion mass and X-ray luminosity. , 526(2):2736–2753, Dec. 2023. doi: 10.1093/ mnras/stad2930.